UiO : Department of Mathematics
University of Oslo

Numerical Simulations of Pharmaceutical Particles Depositing in the Human Respiratory System

Verification and Validation of a Virtual Laboratory

Guttorm Magnus Leiel Kvaal

Master's Thesis, Spring 2017

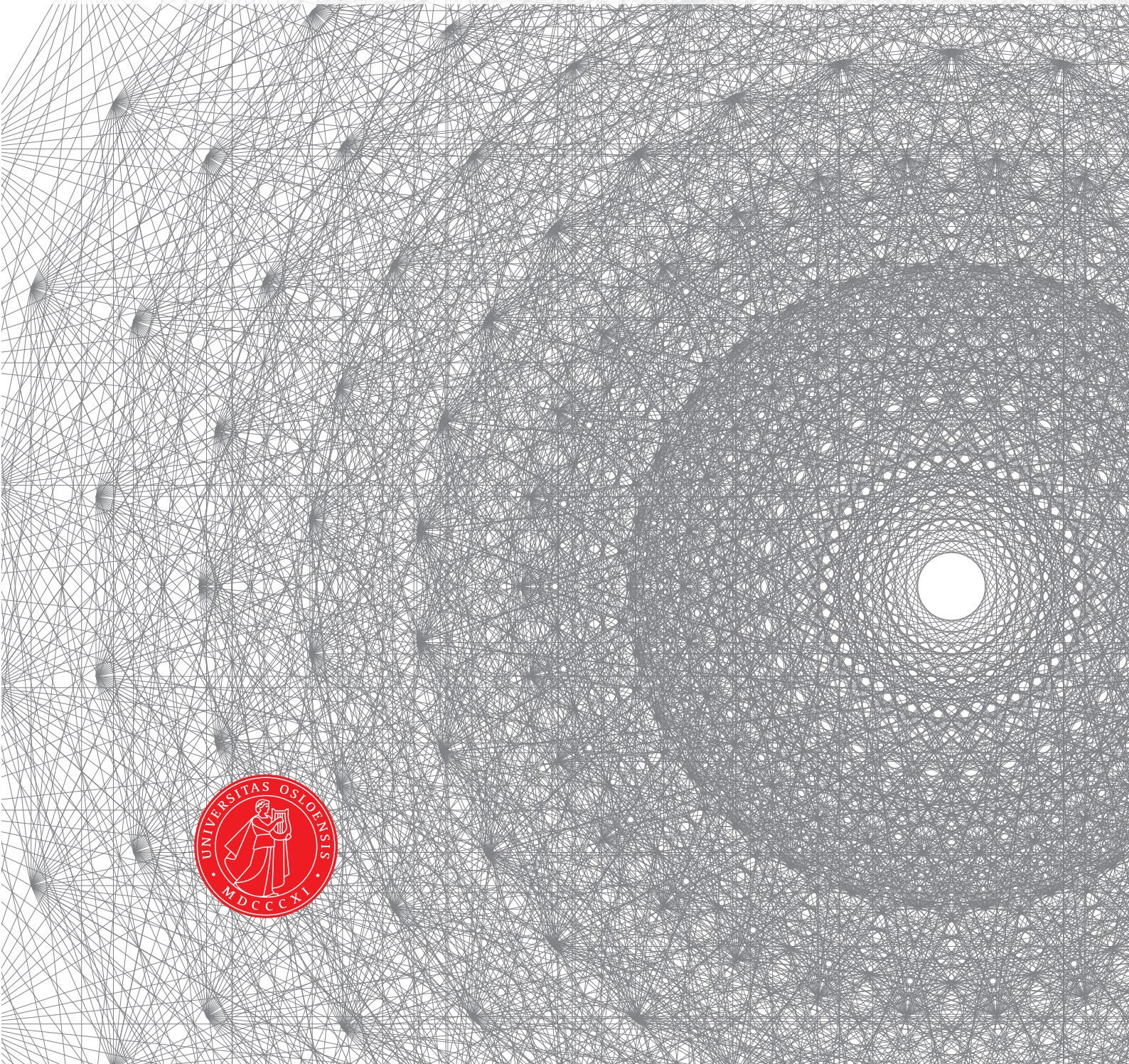

This master's thesis is submitted under the master's programme *Computational Science and Engineering*, with programme option *Mechanics*, at the Department of Mathematics, University of Oslo. The scope of the thesis is 60 credits.

The front page depicts a section of the root system of the exceptional Lie group E_8, projected into the plane. Lie groups were invented by the Norwegian mathematician Sophus Lie (1842–1899) to express symmetries in differential equations and today they play a central role in various parts of mathematics.

Abstract

Millions of people world wide suffer from asthma, and respiratory diseases are one of the leading causes of death. Patients can be treated or relieved by inhalation of medicine, but the efficiency of the treatment is often dependent on on the local deposition of the inhaled drug.

In this thesis, a virtual laboratory for simulating the deposition of pharmaceutical particles inhaled into the human respiratory system has been developed. The virtual laboratory is composed of the Navier-Stokes solver *Oasis*, a particle tracking framework, and several scripts for analyzing flow properties and post-processing of data.

The Navier-Stokes solver *Oasis* has been thoroughly validated on problem specific test cases, and has proven capable of simulating turbulent-like flows with high accuracy and minimal numerical dissipation, at a reasonable computational cost.

Based on considerations on the flow properties in the human respiratory system, a particle motion algorithm has been developed and implemented in the framework of *LagrangianParticles.py* within the open source software *fenicstools*. The algorithm was verified second order accurate, and performed well under validation against established numerical and experimental results.

The airflow in the human respiratory system for moderate and high inhalation rates was simulated, with inflow conditions that mimic the effect of a spray inhaler. The flow field was found to exhibit turbulent-like structures enhanced by asymmetries in the geometry.

Finally, simulations of particles inhaled into the human respiratory system were performed, from which connections between particle size and deposition pattern were determined in overall good results reported in the literature.

Acknowledgement

I want to express my sincere gratitude to my main supervisors Dr. Kristian Valen-Sendstad and Aslak W. Bergersen for the assistance I have received while working on this Master's thesis. By generously sharing your time and knowledge you have both been great inspirations, which I hope is reflected in this thesis. Your inputs has been of the highest value.

Thanks to my co-supervisor Associate Professor Mikael Mortensen for the support and great lectures on viscous flow and turbulence.

I want to thank the community at Simula for including me and widening my academic horizon.

Thanks to my father for reflections and proofreading.

Finally, I want to thank my family and my partner, Rebecca, for continuous love and support.

Contents

Chapter 1

Introduction

1.1 Why Model Inhalation and Particle Deposition?

According to World Health Organization it is estimated that in 2030 the third, forth and sixth leading causes of death will be *chronic obstructive pulmonary disease*, *lower respiratory infections*, and *trachea, bronchus and lung cancers*, respectively [48]. Over 300 million people world wide are suffering from *asthma* and it is expected that 100 million additional affected by 2025, much due to increasingly urban lifestyles [40]. In the US alone, the socio-economic cost of *asthma* in 2007 reached $57 billions, and in 2008, on average, children lost 4 days of school and adults 5 days of work due to *asthma* [1]. All of the above mentioned conditions can in various ways be threated or relieved by inhalation of medicine, but the effectiveness of the treatment is often dependent on the local deposition of the inhaled remedy [32]. This motivates the study of air flow in the human respiratory system with the aim of predicting the deposition pattern of inhaled particles, depending on size, density and respiratory influx.

Qualitative studies of the motion of inhaled air and particles in the human respiratory system emerged in the 50's [52]. An advance in the field came in 1963 with *Weibel's Model A* which gave a simple geometrical description of the human respiratory system, and provided a theoretical framework for calculations of air flow and particle deposition [66]. The first significant in vitro experiment of particle deposition based on a cast of the human respiratory system was performed in 1972 by *Schlesinger and Lippmann* [57]. The experiment was conducted by releasing slightly radioactive particles that left a measurable residue on the cast surface upon impact, a method which is also used in more recent experiments [34]. In vivo experiments on live subjects are much more limited both due to the difficulty of measuring particle deposition within the human airways and the related potential health hazards.

Although in vitro experiments has given valuable and detailed insight into the mechanisms of particle deposition in the human respiratory system, the procedure for such practices are both expensive and time consuming, requiring advanced apparatus and laboratories. Hence, the last two decades the focus has shifted towards numerical simulations with *computational fluid dynamaics* (CFD) [13]. In addition to being faster and cheaper to perform, CFD has the advantage over in vitro methods as it offers much more flexibility and simpler acquisition of data from the experiments. However, CFD can produce erroneous and misleading results if not performed without proper verification and validation, understanding of the underlaying physical, mathematical and numerical problems [65, 16].

Nowadays, the overall deposition pattern of inhaled particles as function of size and density can be predicted with moderate precision [34]. General characteristics of the airflow through the human respiratory system are also described, and is known to possess turbulent properties even at moderate inhalation flow rates [33]. However, further efforts in the characterization of the flow is necessary before a more accurate description of local deposition can be established, with the purpose of optimizing pharmaceutical products for inhalation therapy. In order for CFD to make a break-through in the field, validation of the numerical models are necessary to ensure that the experiments correctly reflects the nature of the flow. For this purpose, researchers at *Brno University of Technology* has performed in vitro experiments of both the flow and particle deposition in a realistic model of the human airways [34]. Based on the experiments, a benchmark test case has been announced, inviting researchers to perform numerical simulations on digitalized versions of the same geometry. The benchmark study is called *Brno lung* and is organized by *SimInhale*, a European network of scientists working on technological development in the field of inhalation medicine.

The goal of this thesis is to develop and validate a *virtual laboratory* for simulating particles of different diameters inhaled in the human respiratory system with the aim of being able to predict the **variations in local deposition patterns depending on particle size and inspiratory flow rates**.

The flow of inhaled air has been modeled with the open source, Navier-Stokes solver *Oasis* [44]. A particle motion algorithm has been developed and implemented within the framework of the open source software, *fenicstools* [43]. Both Oasis and the particle tracking framework has been verified and validated in separate, problem specific test cases, in order to ensure the validity of the obtained results. In addition, several post-processing scripts has been written for analyzing flow properties and measure convergence. Oasis, the particle tracking frame work, and the post processing scripts together constitutes the *virtual laboratory*.

The concluding simulations of particle deposition in the human respiratory system were performed with a digital model provided by the *Brno lung* benchmark, and included 25000 particles of each size, with diameters ranging from 1 μm to 20 μm. A total of 4.5 TB data was generated and analyzed in this thesis.

Chapter 2

Governing Equations, Numerical Methods, and Turbulence Theory

2.1 Governing the Motion of Fluids: Navier-Stokes Equations

The motion of fluids are described by the Navier-Stokes equations which is derived using the laws of conservation of momentum and mass [30]. In this thesis the studied fluid is air with the properties of being Newtonian and incompressible. The Navier-Stokes equations then takes the form:

$$\frac{\partial \mathbf{u}}{\partial t} + \mathbf{u} \cdot \nabla \mathbf{u} = \frac{1}{\rho} \nabla p + \nu \nabla^2 \mathbf{u} + \mathbf{f} \tag{2.1}$$

$$\nabla \cdot \mathbf{u} = 0 \tag{2.2}$$

where $\mathbf{u}$ is the velocity, ρ the density, ν kinematic viscosity and $\mathbf{f}$ body forces. The validity of the incompressibility constraint can be shown by combining conservation of momentum, the ideal gas law - which is valid for air - and an isentropic flow condition, and deduce the following relation

$$-M^2 \frac{dV}{V} = \frac{d\rho}{\rho} \tag{2.3}$$

The mach number M is the ratio of the fluid velocity to the speed of sound ($\approx 340.3\ m/s$ in air), V and ρ is volume and density respectively. Relation 2.3 states that for $M^2 \ll 1$ a change of volume cause negligible change of density, i.e

incompressibility. Assuming that the air flow in the human respiratory system does not exceed 10 m/s, then $M^2 \approx 10^{-4} \ll 1$, and the assumption of incompressibility is considered to be valid [34].

2.2 Methods for solving the Incompressible Navier-Stokes Equations

The existence of a smooth and unique solution to the Navier-Stokes Equations has not been proven, and is one of the Millennium Price Problems [15]. Some analytical solutions can be found given simple geometries and boundary conditions. However, by discretizing the equations it has for decades been possible to use numerical solutions in scientific and engineering applications. There are several features of the Navier-Stokes equations which makes them non-trivial to solve, even with discretization techniques, which can be illustrated by attempting a simple, implicit temporal discretization of Eq. 2.1 and 2.2:

$$\frac{\mathbf{u}^n - \mathbf{u}^{n-1}}{\Delta t} + \mathbf{u}^n \cdot \nabla \mathbf{u}^n = \frac{1}{\rho} \nabla p^n + \nu \nabla^2 \mathbf{u}^n \tag{2.4}$$

$$\nabla \cdot \mathbf{u}^n = 0 \tag{2.5}$$

Here Δt is a finite time step, and superscript n denotes the discrete time level such that $t^n = n\Delta t$. First of all, there are no obvious strategies for computing the next step pressure gradient ∇p^n, and the convective term $\mathbf{u} \cdot \nabla \mathbf{u}$ makes the equations non linear. The coupling of the velocity and pressure through the incompressibility constraint further complicates the issue [21]. Even though these obstacles can be circumvented by different discretization and linearization techniques, making an efficient, energy conserving and minimally dissipating solution algorithm is a challenging task. As of today, several approaches exist with different advantages and drawbacks. One possibility is to solve the equations as a fully coupled system, which, when discretized, results in a linear set of equations that are very computationally demanding to solve [22]. Another, computationally faster approach is to split the equations and solve them separately, as introduced by Chorin and Teman in the late 60's [9]. This type of splitting method, referred to as the projection method, consist of three main steps:

1. Compute a tentative velocity directly from the momentum equation.
2. Project the pressure onto a divergence free velocity field.
3. Update the velocity solution.

The advantage with this approach is that the Naviers-Stokes equations are split into three well known and easy solvable equations; the convection-diffusion, the Poisson equation, and an explicit velocity update. However, this approach does

not come without negative trade-offs: The Poisson equation arising from the correction step demands an additional boundary condition on the pressure at the full boundary. As a result, artificial boundary conditions must be assigned which may lead to an error of first order for the pressure at the vicinity of the boundary, although methods exists for limiting this problem [22].

A development of the projection method introduced by Chorin is the *incremental pressure correction scheme* (IPCS), where the previous time level pressure gradient ∇p^n is used in the computation of the tentative velocity (Chorin's method simply discards the pressure gradient in the tentative calculation). A generic IPCS following a centered Crank-Nicholson temporal discretization reads:

$$\frac{u_k^* - u_k^{n-1}}{\Delta t} + B_k^{n-1/2} = \nabla_k p^* + \nu \nabla^2 u_k^{n-1/2} + f_k^{n+1/2} \tag{2.6}$$

$$\nabla^2 \phi = -\frac{1}{\Delta t} \nabla \cdot u_k^* \tag{2.7}$$

$$\frac{u_k^n - u_k^*}{\Delta t} = -\nabla \phi \tag{2.8}$$

where subscript k denotes spatial coordinates and superscript n temporal step. u_k^* and p^* are tentative velocity and pressure, respectively. The density is incorporated into the pressure gradient through a change of variables, and $B_k^{n-1/2}$ is the convective term $u_k \nabla \cdot u_k$.

Some of the many spatial discretization techniques for solving partial differential equations (PDE), such as the Navier-Stokes Equations, include the *finite difference method* (FDM), the *finite volume method* (FVM) and the *finite element method* (FEM). The FEM is one of the most popular methods today, as it is well suited for computations on complicated geometries.

2.2.1 The Navier-Stokes Solver Oasis

In this thesis the Navier-Stokes equations are solved using the open source solver *Oasis* [44], which is based on the FEM computing platform *FEniCS* [36]. Several schemes are implemented in *Oasis*. In the current work *IPCS-ABCN* is used, which is an *incremental pressure correction scheme* featuring a Crank-Nicholson temporal discretization and a linearization of the convective term, $B_k^{n+1/2}$, through an Adams-Bashforth (AB) projection:

$$B_k^{n+1/2} = (\frac{3}{2} u_k^{n-1} - \frac{1}{2} u_k^{n-2}) \nabla \cdot \frac{1}{2} (u_k^n + u_k^{n-1}) \tag{2.9}$$

This solver is reported to perform well with regards to turbulence transition and scales weakly in parallel computation up to 256 CPU's, which together with a

flexible Python interface makes it well suited for the intended computations, as respiratory flow is reported to be in the transient regime [44, 33]. An algorithm of the *IPCS-ABCN* as implemented in Oasis is presented in Algorithm 1 as follows:

Algorithm 1 Fractional Step Algorithm. Rewritten from M.Mortensen [44]

set initial conditions
$t = 0$
while $t < T$ **do**
    $t = t + \Delta t$
    while error $<$ max error and iter $<$ max iter **do**
        $\phi = p^* = p^{n-1/2}$
        solve eq 2.6 for u_k^*, k=0,...,d
        solve eq 2.7 for $p^{n-1/2}$
        $\phi = p^{n-1/2} - \phi$
    solve eq 2.8 for u_k^n, k=0,...,d
    update to next time step

2.3 Characteristics of a Turbulent Flow

Since it is argued that the air flow in the human respiratory system inherit turbulent-line properties, the following section will give a summary of the most central characteristics of turbulence and how it affects CFD simulations.

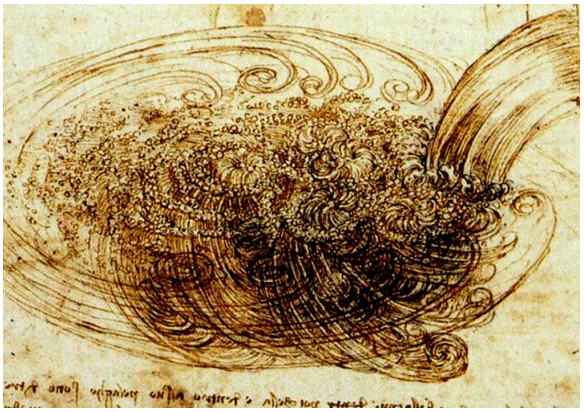

Figure 2.1: Turbulent motion by Leonardo Da Vinci (1451-1519)

One of the first known descriptions of turbulent motion is through drawings made by Leonardo Da Vinci between 1508-1513 [41]. The modern, mathematically approached study of turbulent motion and related field dates back to the 1870s, associated with names such as Boussinesq, Taylor, Prandtl and von Karman [38]. Even today, due to the complex nature of turbulence a complete definition has not

yet been described, but it is possible to characterize it through its many properties [67], some of which are:

- Random fluctuations in space and time
- Energy cascade
- Stochastic motion
- Increased convection

One of the most essential characteristics of turbulence is the presence of the *energy cascade*, first introduced by Richardson (1922). The essence of this idea is that kinetic energy is fed to the turbulence at the largest length scales and continuously transfered to smaller ones until the energy is dissipated by viscous action. A lyrical interpretation of this process was presented by Richardson and sounds as follows:

> Big whorls have little whorls
> Which feed on their velocity,
> And little whorls have lesser whorls
> And so on to viscosity.
>
> Lewis Fry Richardson, 1922

In fluid dynamics, when referring to kinetic energy, it is actually the kinetic energy per unit mass with units $[\frac{m^2}{s^2}]$ that it is being referred to. Similarly, the units for the rate of dissipation is $[\frac{m^2}{s^3}]$. Thus, the total dissipation of energy can be determined from the motions that triggers the turbulence and is scaled as $\epsilon = u_0^3/l_0$, where u_0 and l_0 are the characteristic velocity and length scales of the flow, respectively.

The size of the largest eddies are comparable to the macroscopic length scale of the flow, which is limited by the geometry which it flows around or within, such as the diameter of a pipe. The size of the smallest scales η, however, can be found in *Kolmogorov's Theory of 1941* which is stated in the form of three hypotheses, given sufficiently high Reynold's Number:

- **Kolmogorov's hypothesis of local isotropy**; the small scale turbulent motions are statistically isotropic.
- **Kolmogorov's first similarity hypothesis**; the statistics of the small scale motions are uniquely determined by the fluid viscosity ν and turbulent dissipation ϵ.
- **Kolmogorov's second similarity hypothesis**; the statistics of the intermediate length scale $l_0 \ll l \ll \eta$ are uniquely determined by ϵ only.

The expressions for the Kolmogorov time, velocity and length scales can be derived in just a few steps. The smallest time scale of the flow τ_n is related to the smallest length η and velocity scale u_η as:

$$\tau_n = \frac{\eta}{u_\eta} \tag{2.10}$$

Given a kinematic viscosity ν and characteristic length and velocity scale l_0 and u_0, respectively, the Reynolds number, defined as the ratio of inertial to viscous forces is

$$Re = \frac{l_0 u_0}{\nu} \tag{2.11}$$

At the smallest length and velocity scales the Reynolds number reach unity:

$$Re_\eta = \frac{\eta u_\eta}{\nu} = 1 \quad \rightarrow \quad \eta = \frac{\nu}{u_\eta} \tag{2.12}$$

The dissipation rate is defined as $\epsilon = 2\nu(S, S)$, with $S = \frac{1}{2}(\nabla u + (\nabla u)^T)$, the rate of strain tensor. An expression for the smallest velocity scale is found by utilizing the fact that the dissipation rate scales with the velocity and length scale as

$$\epsilon = \frac{u_\eta^3}{\eta} = \frac{u_\eta^4}{\nu} \quad \rightarrow \quad u_\eta = (\epsilon\nu)^{1/4} \tag{2.13}$$

By inserting 2.13 into 2.12 the smallest length scale is found:

$$\eta = \frac{\nu}{(\epsilon\nu)^{1/4}} = \left(\frac{\nu^3}{\epsilon}\right)^{1/4} \tag{2.14}$$

The smallest time scale can then be expressed by inserting 2.13 and 2.14 into 2.10:

$$\tau_n = \left(\frac{\nu^3}{\epsilon(\epsilon\nu)}\right)^{1/4} = \left(\frac{\nu}{\epsilon}\right)^{1/2} \tag{2.15}$$

Hence, the three Kolmogorov scales, estimating the magnitude of the smallest scales existing in a given flow, are:

$$\eta = \left(\nu^3/\epsilon\right)^{1/4} \tag{2.16}$$
$$u_\eta = (\epsilon\nu)^{1/4} \tag{2.17}$$
$$\tau_\eta = (\nu/\epsilon)^{1/2} \tag{2.18}$$

Furthermore, the ratios between the smallest and largest scales is related to the Reynolds Number as:

$$\eta/l_0 \sim Re^{-3/4} \tag{2.19}$$
$$u_\eta/u_0 \sim Re^{-1/4} \tag{2.20}$$
$$\tau_\eta/\tau_0 \sim Re^{-1/2} \tag{2.21}$$

where τ_0 is the characteristic time scale of the flow.

The full range of length scales in the energy cascade can be split into three, as depicted in Figure 2.2:

1. Energy is introduced at the large length scales in the *energy-containing* range
2. transfered through the *inertial subrange*
3. and dissipated in the *dissipation range*

The last two steps in the energy dissipation process are categorized as the *universial equilibrium range*. The span of the *energy-containing range* l_{EI} is crudely estimated to be $l_{EI} > l_0/6$ and the *dissipation range* $l_{DI} < 60\eta$ [51].

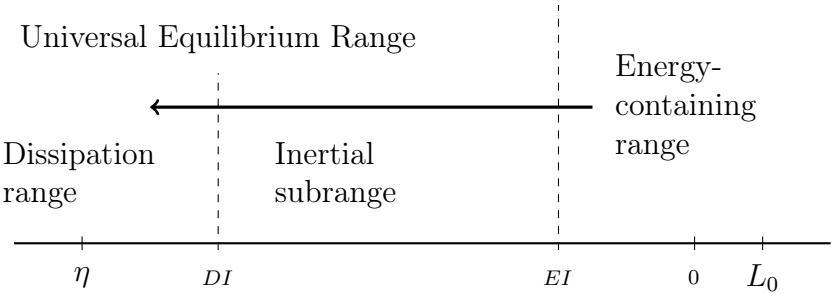

Figure 2.2: Characteristic eddy length sizes for a high Reynolds Number flow, illustrating the relations to various length scales and ranges. Re-sketched from Pope (2001)

The bulk of the kinetic energy is contained within the *energy-containing range* while being transfered through the *inertial subrange* as the eddies are breaking up, until finally being dissipated in the dissipation range. The rate of which energy is transfered from the large scales is, logically, equal to the total dissipation rate ϵ.

2.4 On the Importance of Properly Modeling the Energy Cascade in Numerical Simulations of Turbulent Flows.

As stated above, the bulk of the dissipation happens at the small length scales $< {}_{DI}$, something which has major implications for numerical turbulent flow simulations; the smallest length scale possible to model is confined by the element size of the computational mesh, as well as the discrete time step Δt. Figure 2.3 exemplifies two simulations with a somewhat well resolved and underresolved spatial resolution, respectively. The triangle grids are representing the computational mesh while the whirls the smallest eddies in the flow with a diameter approximately η. In Figure 2.3a the edge length is about half the Kolmogorov length scale and the simulation is reasonably resolved in space, while in Figure 2.3b edge length is about ten times the Kolmogorov length scale and the contrary is the case.

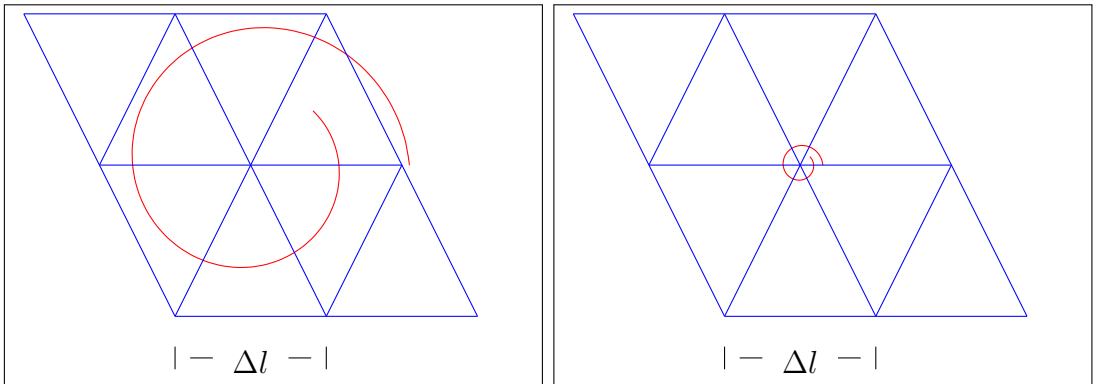

(a) Small length scales being reasonably resolved by the discretization as the eddy length scale η is greater than the edge length of the mesh

(b) Small length scales not being well resolved by the discretization as the eddy length scale η is smaller than the edge length of the mesh

Figure 2.3

Even with modern computers, in most scientific and engineering turbulent flow simulations we are not able to resolve the flow down to the smallest length scales. As an example, *Nakayamna* (1988) studied air flowing at 3.3 m/s over a flat plate 2.4 m long and 1.2 m wide, transitioning into turbulence at around 0.9 m, and found the smallest eddies having a diameter of around 0.04 mm. If performing a fully resolved numerical simulation of the same experiment, modeling the shear layer with a thickness of 10 cm would require approximately 5 trillion mesh points [67]!

Furthermore, not only does an increased mesh resolution cause a rise in the computational cost of solving the equations, smaller steps are also necessary to comply with the smaller cell sizes. Since small time and length scales are associated with

each other, a mesh refinement may be futile if being cut off by a too coarse temporal resolution. Furthermore, numerical errors are introduced both from the spatial and temporal discretization. For a numerical scheme of temporal and spatial order of convergence a and b, respectively, the error can be expressed as:

$$E = \alpha \Delta t^a + \beta \Delta x^b \tag{2.22}$$

where α and β are constants, Δt and Δx, characteristic temporal and spatial resolution, respectively. Thus, a unilateral reduction of only one of the terms is futile if the other term is dominating.

Following the *Energy Cascade*, the consequences of not resolving the small scale motions may affect the flow up to the macroscopic level, such as causing spurious break downs of turbulent jets [4]. The particular effects of a under-resolved flow simulation are both dependent on the problem studied and the numerical scheme applied. As is observed in Chapter 3.4, artificial numerical dissipation may work as a counter weight when the smallest flow scales are not captured in coarse mesh simulations. Since it is not possible *a priori* to determine the full range of effects caused by under-resolved flow simulations, the sensitivity of the measured metrics to the spatial and temporal resolution should be examined through a refinement study. For many problems where crude metric are investigated, such as when computing time averaged lift and drag coefficients, the desired result may be obtained within the expected level of accuracy even for under-resolved flows [28]. As the size of the particles studied in this thesis are of the same magnitude as the smallest length scales typically found in turbulent-like flows, it is plausible that the computed pattern of deposited particles are highly sensitive to temporal and spatial resolution. Hence, the methods used for the characterization of turbulence and measuring convergence are described in the next section.

2.4.1 Methods for Measuring and Visualizing Turbulence

The aim of this thesis is not to compute an optimal turbulent flow simulation. However, since it is reported that flow pattern of the studied problem possesses characteristics of a turbulent flow, it is necessary to investigate how turbulence properties are affected by temporal and spatial resolution. In order to quantify how well resolved a flow simulation is, both temporally and spatially, the Kolmogorov scales have been computed and compared with the cell circumference Δl and time step Δt. As least one cell is needed to roughly approximate a length scale in the dissipation range, the ratio between η and Δl must be smaller or equal to one for the simulated flow to be considered a direct numerical simulation (DNS) where all turbulence length scales are well resolved.

A second, similar approach used is to consider the simplified length and time scale ratios described in *Statistical Theory and Modeling for Turbulent Flow* (2001)

$$l^+ = \frac{u_* \Delta x}{\nu}$$
$$t^+ = \frac{u_*^2 \Delta t}{\nu}$$

where ${u_*}^2 = \nu(S,S)^{1/2}$, where S is the previously defined strain tensor.

As mentioned in the previous section, turbulence is characterized by stochastic fluctuations in fluid velocity and pressure. If measuring the magnitudes of a quantity over a statistically significant time interval $(t_0, t_0 + T)$, a time average, here exemplified by the velocity, is found as:

$$\overline{\mathbf{u}}(x) = \frac{1}{N} \sum_{i}^{N} \mathbf{u}(x, t_i) \tag{2.23}$$

where N is the number of samples at discrete time intervals t_i and x is the spatial location. Following the Reynolds decomposition, the fluctuating parts are then defined as the difference between the instantaneous and the mean values:

$$\mathbf{u}'(x, t_i) = \mathbf{u}(x, t_i) - \overline{\mathbf{u}}(x) \tag{2.24}$$
$$p'(x, t_i) = p(x, t_i) - \overline{p}(x) \tag{2.25}$$

In order to measure the magnitude of the turbulent fluctuations, root-mean-square (RMS) values are uses, defined as:

$$\mathbf{u}'(x, t_i)_{rms} = \sqrt{\frac{1}{N} \sum_{i}^{N} \mathbf{u}'^2(x, t_i)} \tag{2.26}$$

The turbulence is considered statistically stationary if Eq 2.23 and 2.26 are invariant under a translation in time. Furthermore, in a numerical simulation it is important that sampling is performed after the flow has become developed, meaning that it is no longer affected by initial effects. Thus, t_0 is some time after the flow has become developed and T is the time for the flow statistics to converge.

2.4.2 The Q Criterion

There are several methods for visualizing vortex structures. One of these methods are the Q-criterion, where the magnitude of the vorticity is larger than the magnitude of the strain [29]

$$Q = \frac{1}{2}\left(|\mathbf{\Omega}|^2 - |\mathbf{S}|^2\right) > 0 \tag{2.27}$$

where $\mathbf{\Omega} = \frac{1}{2}(\nabla\mathbf{u} - (\nabla\mathbf{u})^T)$ and the rate of strain tensor S is as previously defined.

Chapter 3

Verification and Validation of the Fluid Flow Solver

3.1 On the Difference between Verification and Validation in Computational Science and Engineering

In the process of the development of any product, Quality Assurance (QA) is an indispensable routine to be performed before the product is used or released for public use. In the setting of this thesis, the product is a number of algorithms that are programmed in computer codes, and it is crucial that the expected performance of the algorithms is assured before any results are presented to a wider audience. Following the chapter on Semantics in P. J. Roache's *Verification and Validation in Computational Science and Engineering* (1998) [54], code QA can be split into two separate practices; *verification* and *validation* (V&V). Even though being synonyms and often mistaken or interchanged in the literature, verification and validation have, according to Roache's definition, strictly independent definitions and goals. Both are performed with the aim of assuring the quality of code and algorithms, and hence the validity of the obtained results. In this thesis, verification and validation are, respectively, defined as:

- Verification is to check that the equations are solved correctly.
- Validation is to check that equations correctly solves the physical problem in question.

Thus, in the setting of computational science and engineering, verification is to ensure that the equations are correctly implemented in the code, while validation is to assess whether the implemented equations and boundary conditions correctly reflect the physics of the problem in question. Another important distinction is that while a computer code can, at least to some extent, be considered verified,

validation is a more problem specific and continuous process. Even though a software or code may have been extensively tested, it is still necessary to perform a validation test when it is applied on a new problem.

3.2 Verification and Validation of the Navier-Stokes Solver *Oasis*

The order of accuracy and performance of *Oasis* has been thoroughly tested [44, 26, 4]. In the paper describing the structure and theory behind the solver, a rate of convergence test was carried out by computing the 2D Taylor-Green Vortex. Due to "super convergence" a rate of convergence two orders higher than the polynomial degree was reported. A second order temporal convergence was found in agreement with the Crank-Nicholson discretization [44]. In the master thesis of Aslak W. Bergersen a verification test was carried out through the *method of manufactured solutions*, recovering the expected convergence rates. Since the performance and accuracy of *Oasis* has been verified, a separate verification has not been carried out in this thesis. However, in compliance with the arguments in the previous sections, validation tests has been performed.

The process of validation is typically split into building block which are gradually more complex and problem specific. The perhaps most desirable method of assessing a result is by comparison with trustworthy experimental data. For many applications where the scale or nature of the problems makes the acquisition of experimental data difficult, other approaches are possible, such as comparison with other, well established numerical results.

In this thesis two different benchmarks are considered with the intention of validating that *Oasis* is well suited for computing turbulent flow in the human respiratory system. Neither of the problems are of a nature for which experiments can be conducted, but have both been subject to several benchmark studies [56, 47]. The first problem concerns a 2D laminar flow past a cylinder asymmetrically located in a channel, i.e., *the von Karman vortex street*. This problem was selected in order to validate the use of *Oasis* in the computation of a laminar, vortex shedding flow with minimal computational resources by applying simple refinement techniques. In the second validation test case the 3D *Taylor-Green vortex* has been computed with the intention of verifying that *Oasis* can, at a reasonable computational cost and with limited numerical dissipation, compute laminar flow transitioning into turbulence.

3.3 Validation Case 1: The von Karman Vortex Street

In 1996 *M. Schäfer* and *S. Turek* announced the study *Benchmark Computations of Laminar Flow Around a Cylinder* [56]. Participants from 17 different German research groups participated in what became one of the first large CFD benchmark studies. The aim of the study was to analyze the performance of different computational methods, (e.g., Coupled Solvers vs. Fractional Step Solvers), and to determine whether and why certain approaches are superior to others. The benchmark consists of a total of nine 2D and 3D problems.

In this thesis one of the 2D test cases was computed. The domain of this problem is a cylinder located with a small offset to the center of a narrow channel, as depicted in Figure 3.1. Due to the asymmetric location of the cylinder, wakes in the flow field behind the cylinder is created, causing oscillations in the drag and lift forces.

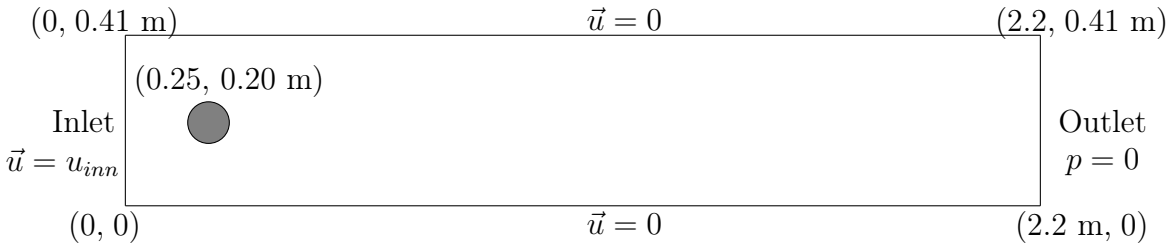

Figure 3.1: Schematic drawing of the 2 dimensional cylinder in a channel. Note that the cylider is located asymmetrically in the channel, thus causing instabilities in the flow field.

Setup for the von Karman test case (2D-1, unsteady, Re=100)

The inflow condition is:

$$u(0, y, t) = 6(0.41 - y)/0.41^2, \quad v(0, y, t) = 0$$

The following metrics are computed:

- Maximum Drag Coefficient, $C_{d\,max}$.
- Maximum Lift Coefficient, $C_{l\,max}$.
- Change of the pressure behind the cylinder, $\Delta P(t_0 + \frac{1}{2f})$.
- Strouhal Number, Str.

Here, t_0 is defined as the discrete time when maximum drag occurs, f is the vortex shedding frequency and $Str = D/f\bar{U}$ with D being the circle diameter ($0.1\ m$) and $\bar{U}$ the mean velocity ($1\ m/s$). The drag and lift are calculated by, respectively, taking the first and second component of the force vector:

$$F = \int_{Circle} \left(\nu(\nabla u + (\nabla u)^T) - pI\right) \cdot n\ ds$$

where ν is the viscosity, $\mathbf{u}$ the velocity, p the pressure, I the unit matrix, and n the unit vector normal to the cylidner surface. The corresponding coefficients are defined as:

$$C_d = \frac{2F_x}{\rho \bar{U} D} \qquad C_l = \frac{2F_y}{\rho \bar{U} D}$$

3.3.1 Methods for the Mesh Convergence Test

In time dependent numerical simulations, errors are introduced from both the temporal and spatial discretization as described in Eq. 2.22. Depending on the applied discretization technique such as the FDM, FEM, or the *spectral method*, several approaches are possible to reduce the spatial numerical error. In FEM we can either increase the mesh resolution, the order of the polynomial space, or both. In this section, a convergence test was carried out by adjusting the mesh density while the polynomial degree was kept constant (P1P1). In order to keep errors from the temporal discretization low, the time step was set to $\Delta t = 5 \cdot 10^{-4}\ s$ for all computations.

Even though the geometry in question is quite simple, the process of refining the mesh for obtaining convergence at a reasonable computational cost is not trivial. A brute force process would simply be to refine the every triangle in the mesh until convergence is reached, but that is likely to produce meshes that requires computations that are inconvenient or even impossible to perform on a personal laptop. A better approach is to refine in the area that intuitively has the largest impact on the metrics sought, namely the the pressure and the velocity gradients around the cylinder. Three different mesh refinement parameters were considered;

- The number of nodes constituting the cylinder, N_{cyl}
- The radial thickness of the innermost cell to the cylinder surface, Δy_1
- The resolution in the domain up to $0.5\ m$ downstream of the cylinder, Δx_w

A total of 9 meshes were produced using the open source tool, GMSH [20] which easily allows controlling the local mesh density. In Mesh1 - Mesh4 only the cells

constituting the cylinder are refined. For the remaining meshes a more deliberate refinement approach was taken. The cells at the cylinder surface was organized in a structured inflation layer, where the thickness of the innermost layer is denoted Δy_1. Furthermore, as stated above, the cells up to a distance of 0.5 m behind the cylinder were also refined, in order to better approximate the motion of the vortex shedding. For all meshes the characteristic edge length in the field far away from the cylinder is kept constant at $\Delta x_{far} = 2.0 \cdot 10^{-2}\ m^2$. The mesh characteristics are presented in Table 3.1 at the end of this section.

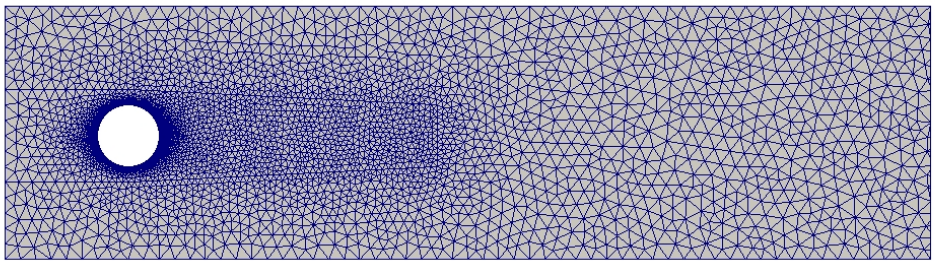

(a) Mesh6

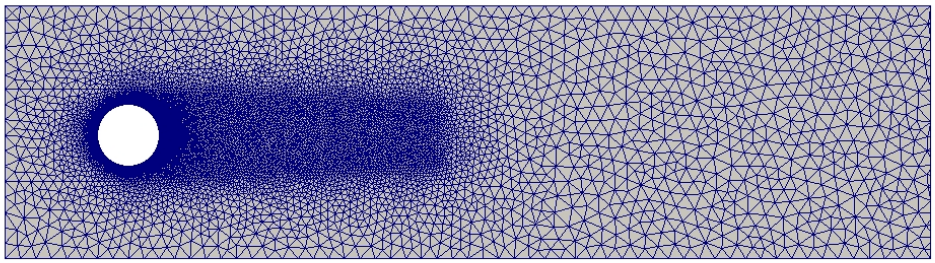

(b) Mesh9

Figure 3.2: Overview of mesh resolution around and behind the cylinder.

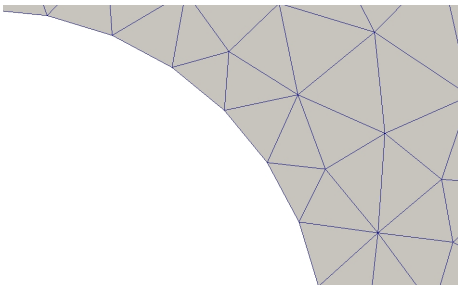

(a) Mesh1

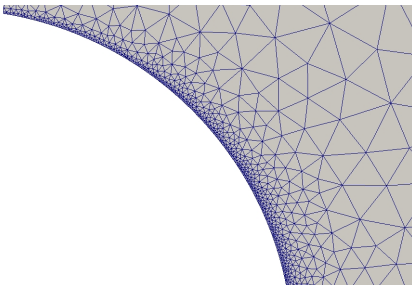

(b) Mesh3

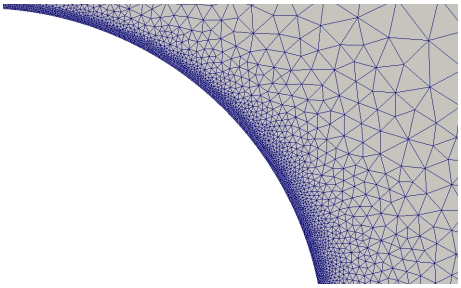

(c) Mesh6

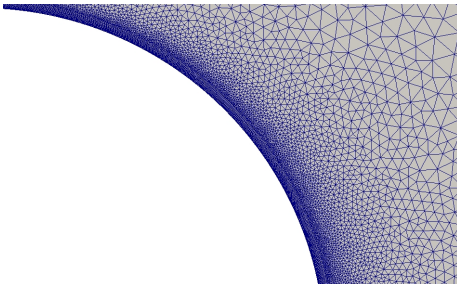

(d) Mesh9

Figure 3.3: A close view of the mesh resolution at the cylinder boundary.

3.3.2 Flow Description

It is important to note that the cylinder is located with a small offset to the center of the channel. This causes different flow rates and velocities at each side of the cylinder which affects the pressure gradients and triggers flow instabilities. The evolution of the velocity and vorticity ($\nabla \times \mathbf{u}$) field is depicted in 3.4. At $t = 0.5\ s$ the flow is still undeveloped and steady, but asymmetries can be observed. A second later instabilities are being apparent as oscillations are observed behind the cylinder. At $t = 5\ s$ the instabilities have reached a steady state causing vortex shedding behind the cylinder. The vortices are rotating in every other direction, manifesting the conservation of momentum.

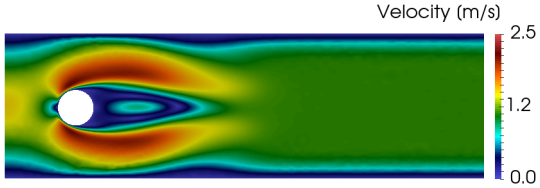

(a) Steady flow at $t = 0.5\ s$ (velocity).

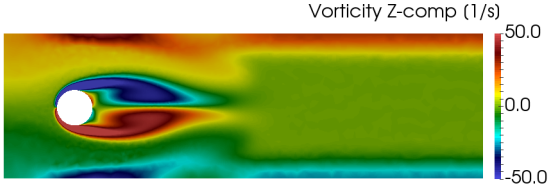

(b) Steady flow at $t = 0.5\ s$ (vorticity).

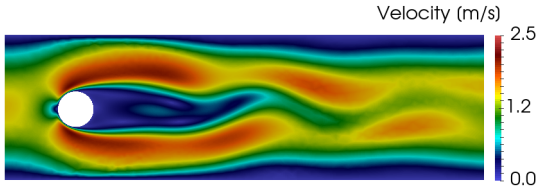

(c) Instabilities at $t = 1.5\ s$ (velocity).

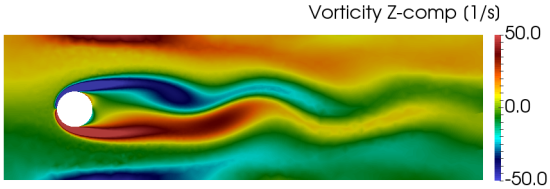

(d) Instabilities at $t = 1.5\ s$ (vorticity).

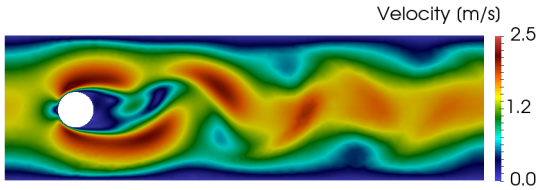

(e) Developed von Karman vortex street at $t = 5\ s$ (velocity).

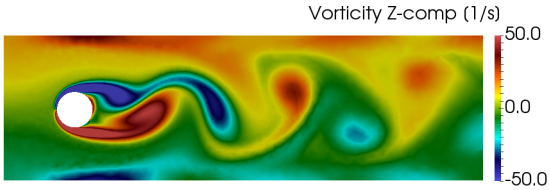

(f) Developed von Karman vortex street
at $t = 5\ s$ (vorticity).

Figure 3.4: Velocity and vortex profiles at $t = 0.5$, 1.5 and 5.0 s, showing the evolution of the vortex shedding. The computations were performed on Mesh7 (cf., Table 3.1)

3.3.3 Results and Discussion

The results produced following computations on the nine different meshes are presented in Table 3.2, while Table 3.3 shows the results established in the benchmark. Curves illustrating the fluctuations in lift and drag are depicted in Figure 3.5. Of

note is the very irregular drag initially in the simulation. The computations performed on Mesh1 - Mesh4 underestimated the lift and drag coefficients overall as a consequence of not being able to capture the steep gradients at the cylinder surface. For Mesh1 and Mesh2 the errors may also be ascribed to insufficient number of cells constituting the cylinder, as seen in Figure 3.3a. For Mesh6 - Mesh9 a convergence in all metrics are observed with variations below 1% except for ΔP in Mesh6. The lift coefficients and Stokes numbers are within the bounds established in the benchmark, while the drag coefficient and pressure difference is marginally below. For the last 3 meshes the Strouhal number is identical down to 4 digits.

It is concluded that it is possible, with a simple mesh refinement strategy, to reproduce the results following *Schäfer* and *Turek's* benchmark and achieve grid independent solutions with *Oasis*.

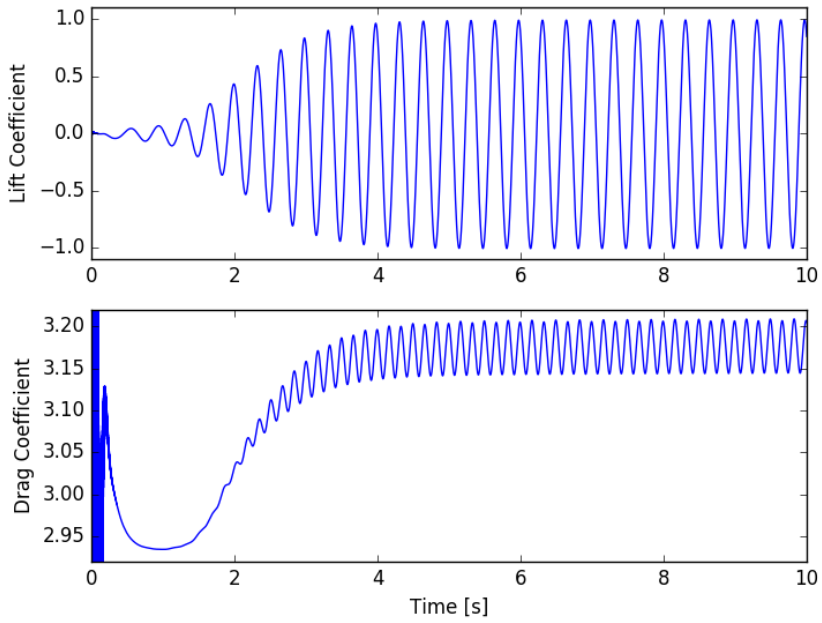

Figure 3.5: The evolution of the lift and drag coefficients.

Mesh	N_{tot}	N_{cyl}	Δy_1 $[m]$	Δx_w $[m]$
Mesh1	4000	32	n/a	n/a
Mesh2	7000	128	n/a	n/a
Mesh3	12000	512	n/a	n/a
Mesh4	19000	1024	n/a	n/a
Mesh5	20000	512	$2.0 \cdot 10^{-4}$	$2.0 \cdot 10^{-2}$
Mesh6	28000	512	$2.0 \cdot 10^{-4}$	$1.0 \cdot 10^{-2}$
Mesh7	42000	512	$1.0 \cdot 10^{-4}$	$5.0 \cdot 10^{-3}$
Mesh8	52000	1024	$1.0 \cdot 10^{-4}$	$2.5 \cdot 10^{-3}$
Mesh9	68000	1024	$5.0 \cdot 10^{-5}$	$2.5 \cdot 10^{-3}$

Table 3.1: Mesh characteristics for the von Karman vortex street benchmark. N_{tot} - total number of cells, N_{cyl} - number of cells constituting the cylinder, y_1 - radial thickness of the innermost boundary layer cell, x_w - cell density in the domain downstream of the cylinder. y_1 and x_w was not specified for Mesh1 - Mesh4

Mesh	$C_{l\,max}$	$C_{d\,max}$	$\Delta P(t_0 + t_{1/2})$	Str
Mesh1	0.3852	2.7442	2.8381	0.3134
Mesh2	0.8673	2.9555	2.4242	0.2999
Mesh3	0.9673	3.1380	2.3641	0.2990
Mesh4	0.8488	3.1103	2.3891	0.2999
Mesh5	0.9237	3.0935	2.4661	0.2999
Mesh6	0.9952	3.2105	2.4314	0.2994
Mesh7	0.9979	3.2080	2.4646	0.3003
Mesh8	1.0037	3.2150	2.4631	0.3003
Mesh9	1.0040	3.2090	2.4594	0.3003

Table 3.2: Results for the von Karman vortex street benchmark for steady flow, Re=100.

$C_{l\,max}$	$C_{d\,max}$	$\Delta P(t_0 + t_{1/2})$	Str
0.9900 - 1.0100	3.2200 - 3.2400	2.4600 - 2.5000	0.2950 - 0.3050

Table 3.3: Upper and lower bounds for the results produced by the benchmark study.

3.4 Validation Case 2: The 3D Taylor-Green Vortex

The Taylor-Green vortex (TGV) is a fluid dynamics problem developed to study the process of large eddies breaking up into smaller eddies [61]. As the TGV problem has a relatively simple setup and involves central mechanisms in turbulence, it is a much used case for testing the accuracy of numerical schemes on modeling the transition of laminar flow into turbulent-like motion. Since this thesis concerns the modeling of airflow in the human airways, known to possess turbulent-like properties [33], the TGV problem is considered as an appropriate validation case for this purpose.

3.4.1 Notes on TGV and Turbulence

In Chapter 2.3 it was argued that even though a complete and definite definition of turbulence is not made, several key characteristics must be present for a flow to be characterized as turbulent. Two of these characteristics include *random fluctuations* in space and time, and *local isotropy* of the small length scales. As the TGV is completely deterministic and DNS simulations results in a symmetric flow field due to the periodic boundary conditions, it is somewhat dubious to refer to the problem as turbulent. Even though the TGV is not turbulent in the strictest sense, the presence of the *energy cascade* is still prominent in the problem, making it relevant for testing the performance of numerical schemes on turbulence problems. Because the TGV flow contains some turbulence characteristics and is frequently described as turbulent in the literature [12, 6], this phrase will also be adopted here, despite the aforementioned contradiction.

3.4.2 Methods for Computing and Comparing the Rate of Kinetic Energy Dissipation Between Different Meshes

Even though the 3D Taylor-Green does not have an analytical solution, DNS simulations of the problem has been conducted, providing reference solutions for comparison. In addition, by computing the kinetic energy and the dissipation of energy it is possible to measure the effects of different numerical schemes and resolutions on how well the transition process is being modeled. As the coarser meshes are not able to capture the smallest length scales where a substantial amount of energy is being dissipated (cf., Section 2.3), it may be expected that computations on coarse meshes will result in artificially high levels of kinetic energy. However, many CFD schemes are subject to artificial numerical dissipation, and in particular those of lower order [24]. Even though a thorough examination of the sources behind numerical dissipation (or diffusion) is outside the scope of this thesis, its

effects related to different spatial resolution have none-the-less been investigated in this section.

Given a velocity field, $\mathbf{u}$, existing within a finite volume, $\mathbf{V}$, the volume averaged kinetic energy is defined as:

$$E_k(\mathbf{u}) = \frac{1}{2V} \int_V \mathbf{u} \cdot \mathbf{u} \, \mathbf{dV} \tag{3.1}$$

The total kinetic energy dissipation rate (KEDR) can be found by differentiating Eq. 3.1 with respect to time:

$$\epsilon(u) = \frac{E_k(\mathbf{u})}{dt} \tag{3.2}$$

Furthermore, the enstrophy is the volume averaged dot product of the vorticity:

$$\varsigma = \frac{1}{2V} \int_V \omega \cdot \omega \, dV \tag{3.3}$$

where $\omega = \nabla \times \mathbf{u}$, i.e the vorticity. For an incompressible fluid with constant density, ρ, and viscosity, μ, the KEDR is related to the enstrophy through the following relation:

$$\epsilon(\varsigma) = \frac{2\mu\varsigma}{\rho} \tag{3.4}$$

The KEDR computed from the enstrophy is dissipation due to vortical structures and shows how well the small scale motions are being captured [8]. Hence by comparing the two different KEDR curves for a given simulation it is possible to measure the amount of dissipation due other effects than vorticity, e.g., *numerical dissipation* [12].

Following NASA's *3rd International Workshop on Higher-Order CFD-Method* [47], reference solutions to $\epsilon(\mathbf{u})$ and $\epsilon(\varsigma)$ was made available. The reference solutions were produced by a spectral method scheme.

In order to distinguish between the two approaches for computing dissipation, the KEDR from direct differentiation is denoted $\epsilon(\mathbf{u})$ (cf., Eq. 3.2), and the KEDR related to the enstrophy is denoted $\epsilon(\varsigma)$ (cf., Eq. 3.4).

3.4.3 Setup

The simulations were performed over a $[-\pi, \pi]^3$ domain with periodic boundary conditions and the motion was initiated with the following velocity field:

$$u(x, y, z) = V_0 \sin(x/L) \cos(y/L) \sin(z/L) \tag{3.5}$$
$$v(x, y, z) = -V_0 \sin(x/L) \cos(y/L) \sin(z/L) \tag{3.6}$$
$$z(x, y, z) = 0 \tag{3.7}$$
$$p(x, y, z) = p_0 + \frac{\rho V_0^2}{16} (\cos(2x/L) + \cos(2y/L)) (\cos(2z/L) + 2) \tag{3.8}$$

The Reynolds number was set to 1600 which allows the comparison of results with several published papers. As the density is incorporated into the pressure gradient in *Oasis*, it was set to 1 kg/m^3 in 3.8 . Furthermore, $L = 1\ m$ and $V_0 = 1\ m/s$ forcing $\nu = 1/1600\ m^2/s$ in order to obtain the desired Reynolds number. The computational time was set to $T = 20\ s$ which made it possible to study the process of the flow from transitioning laminar to turbulent, before being relaminarized. The time step was set to $\Delta t = 2 \cdot 10^{-3} s$ giving a total of 10000 time steps. In order to study the effect of spatial discretization, three different meshes were considered in this study; 32, 64 and 128 cells in each direction of the cubical domain, with P1P1 finite elements. The simulations conducted on the different meshes will be referred to as N32, N64, and N128, respectively.

3.4.4 Results

Discretization	$\frac{\epsilon(\mathbf{u})-\epsilon(\varsigma)}{\epsilon(\mathbf{u})}$	$\frac{\epsilon(\mathbf{u})-\epsilon(\mathbf{u})_{\text{reference}}}{\epsilon(\mathbf{u})_{\text{reference}}}$
N32 P1P1	0.0793	0.1221
N64 P1P1	0.0549	0.0946
N128 P1P1	0.0341	0.0214

Table 3.4: Center column: normalized discrepancy between $\epsilon(\mathbf{u})$ and $\epsilon(\varsigma)$ (numerical dispersion), right column: normalized discrepancy of $\epsilon(\mathbf{u})$ from reference solution.

Iso-surfaces of the Q-criterion (cf., Eq. 2.27) at six characteristic stages in the vortex build-up and dissipation process are depicted in Figure 3.6 for N128. Initially the flow field is laminar and characterized by eight large, round vortices (Figure 3.6a). Note the periodic boundary conditions mirroring the half vortices. At $t = 3\ s$ the vortices have begun to stretch and divide, but the KEDR is still low (Figure 3.6b). Two seconds later the KEDR has rapidly increased and more eddies are formed (3.6c). At $t = 9\ s$ the KEDR has reached peak values and the flow is fully turbulent (Figure 3.6d). At $t = 15\ s$ the magnitude of the KEDR is

approximately the same as at $t = 5\ s$, but the size of the vortices are much smaller (Figure 3.6e). After 20 s the KEDR is starting to flatten out, the distribution of length scales is more homogeneous and the effect of the *Energy Cascade* is wearing out. If simulated over a longer time interval the flow field would eventually become completely relaminarized.

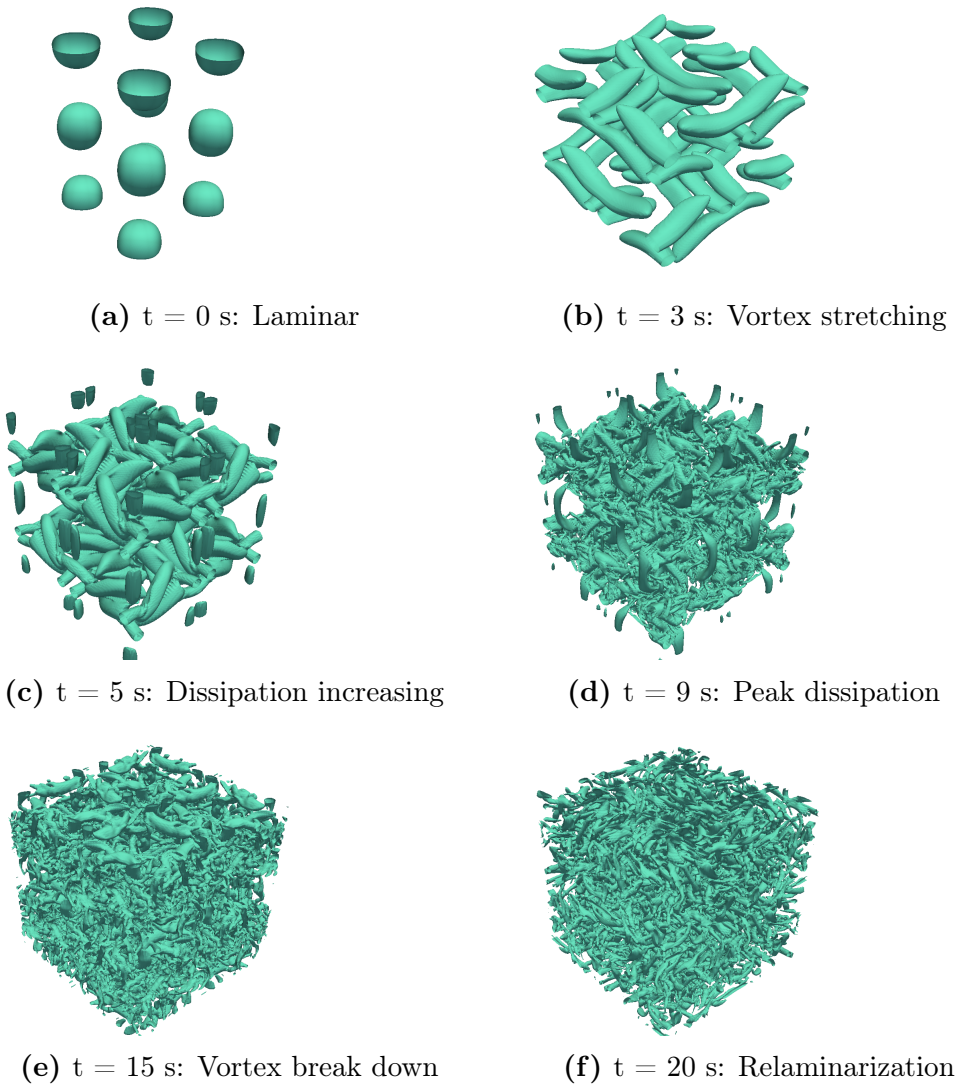

(a) t = 0 s: Laminar

(b) t = 3 s: Vortex stretching

(c) t = 5 s: Dissipation increasing

(d) t = 9 s: Peak dissipation

(e) t = 15 s: Vortex break down

(f) t = 20 s: Relaminarization

Figure 3.6: Iso-surfaces of the Q criterion showing the evolution of vortices breaking down into small scale motion.

As indicated in the previous section, it may, based on the theory of the *energy cascade*, be reasonable to make the a priori assumption that the KEDR will be overall lower for computations performed with coarser spatial resolutions because the length scales in the *dissipation range* are not properly captured. The curves presented in Figure 3.7 do, however, not support this assumption.

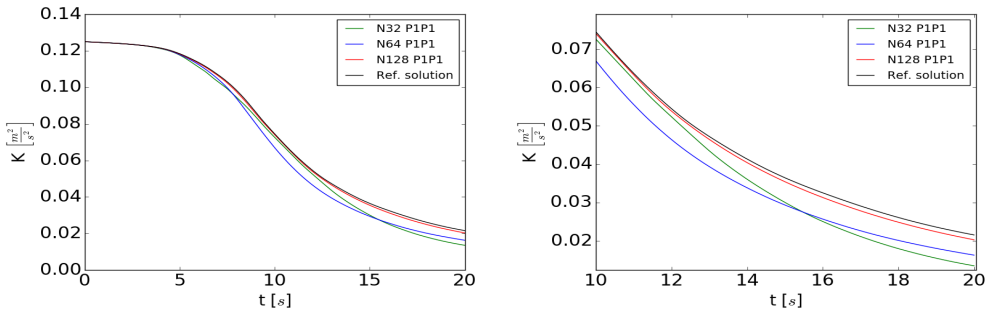

Figure 3.7: Temporal Development of the kinetic energy

At the end of the simulation the kinetic energy is lowest for N32 and is increasing for the finer discretizations. Thus, surprisingly, the coarsest mesh yields the largest total dissipation, which is an indication that there are other processes than just the viscous dissipation contributing to the KEDR.

The Figures 3.8a - 3.8c shows comparisons of $\epsilon(\mathbf{u})$ and $\epsilon(\varsigma)$ for each of the simulations. By observing the curves in relation to the second column in Table 3.4, it is clear that $\epsilon(\mathbf{u})$ and $\epsilon(\varsigma)$ is converging for better resolved simulations, which is in agreement with reference solution, where $\epsilon(\mathbf{u})$ and $\epsilon(\varsigma)$ are indistinguishable [12]. In Figure 3.8d $\epsilon(\varsigma)$ is compared for the various simulations. N128 is closest resembling the reference solution.

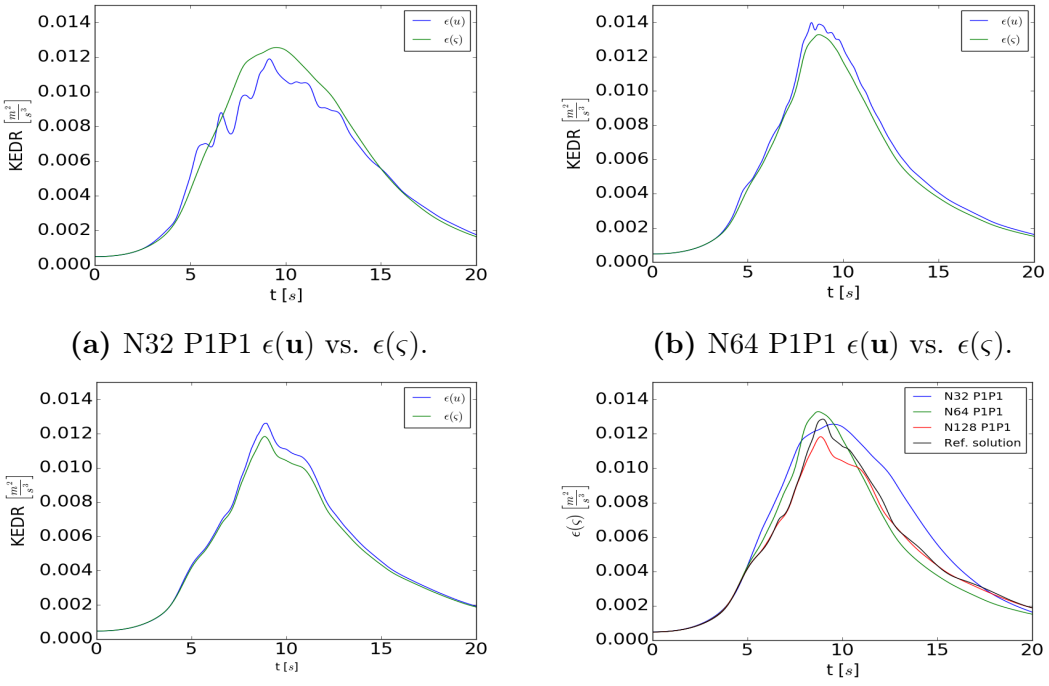

(a) N32 P1P1 $\epsilon(\mathbf{u})$ vs. $\epsilon(\varsigma)$.

(b) N64 P1P1 $\epsilon(\mathbf{u})$ vs. $\epsilon(\varsigma)$.

(c) N128 P1P1 $\epsilon(\mathbf{u})$ vs. $\epsilon(\varsigma)$.

(d) Enstrophy computed KEDR. $\epsilon(\varsigma)$

Figure 3.8: Time development of $\epsilon(\mathbf{u})$ vs. $\epsilon(\varsigma)$ (a,b,c), and comparisons of $\epsilon(\varsigma)$ between the three meshes (d).

Figure 3.9a shows the directly computed KEDR $\epsilon(\mathbf{u})$ for the three simulations in relation to the reference solution, while Figure 3.9b exhibits N128 extracted. Whereas N32 and N64 yields $\epsilon(\mathbf{u})$ with an considerable offset from the reference solution, N128 shows a very good correlation with a normalized discrepancy of only $\approx 2\%$ following last row in column 3 in Table 3.4.

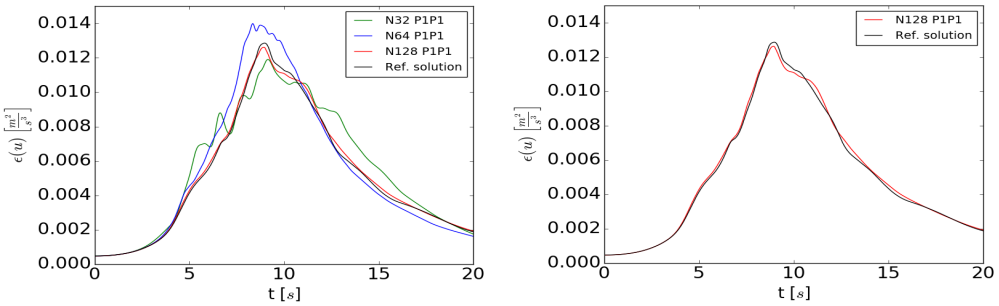

(a) Directly computed KEDR $\epsilon(\mathbf{u})$. **(b)** N128 P1P1 $\epsilon(\mathbf{u})$

Figure 3.9: The development of $\epsilon(\mathbf{u})$ for all three meshes compared with the reference solution.

For a well resolved simulation (e.g. the reference solution) $\epsilon(\mathbf{u}) = \epsilon(\varsigma)$, and thus any inconsistency must be due to *numerical dissipation*. It was observed that the discrepancy between $\epsilon(\mathbf{u})$ and $\epsilon(\varsigma)$ decreased when the mesh was refined. The simulation on N128 both showed a good correlation between $\epsilon(\mathbf{u})$ and $\epsilon(\varsigma)$, as well as to the reference solution. It can thus be concluded that *Oasis* is capable of computing turbulence-like flow conditions at a moderate computational cost and with very low numerical dissipation.

3.5 Concluding Remarks on the Validation of the Navier-Stokes Solver *Oasis*

In Section 3.3 it was shown that with only a simple mesh refinement strategy we are able to compute a 2D transient flow in good agreement with established results, and obtain a mesh independent solution at a low computational cost. The significance of keeping a high mesh resolution in sections of the domain with intuitively high gradients was also demonstrated. A similar approach was also taken when the model of the upper human respiratory system was meshed, as outlined in Section 6.4.2.

In Section 3.4 *Oasis* was tested by simulating a laminar flow transitioning into turbulence before being relaminarized, and showed excellent agreement with the reference solution. Based on the validation test cases, it is concluded that ***Oasis* is an *energy conserving* and *minimally dissipative* Navier-Stokes solver capable of producing high precision simulations of turbulent flow at a**

moderate computational cost. Oasis has also been extensively used to model turbulent-like flows in the cardiovascular system and demonstrated phenotypically similar results compared to spectral element method solvers. [3, 25, 26, 27, 46, 60, 63, 64, 65]. Thus, *Oasis* is deemed an adequate choice for computing air inhaled in the human respiratory system under turbulent flow conditions.

Chapter 4

The Kinetics of Particles Dispersed in a Moving Fluid

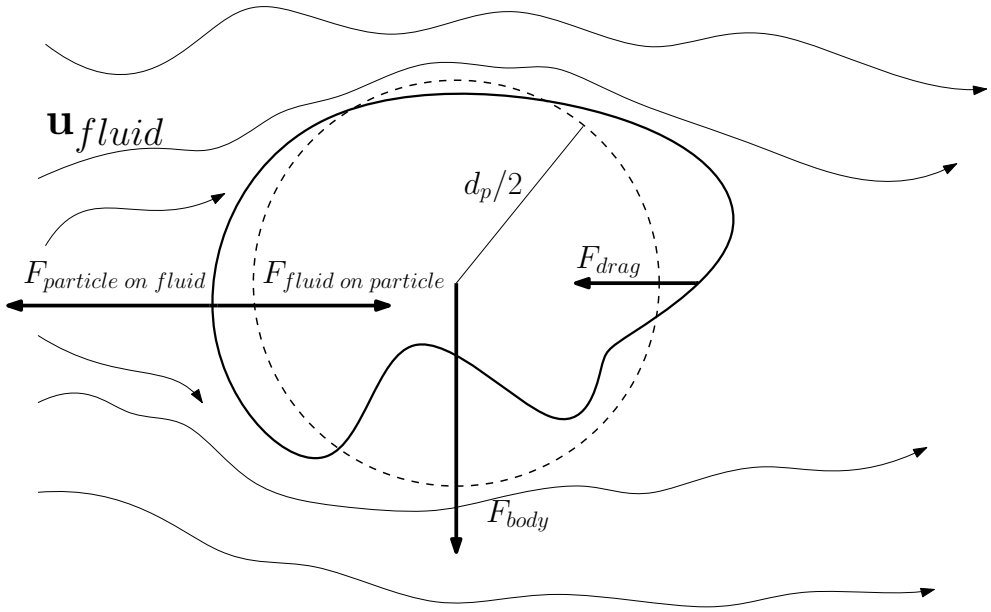

Figure 4.1: A particle influenced by a moving fluid. Body forces such as gravity working on the particle, in addition to the friction between the particle and the fluid. The size of the particle is defined by an characteristic radius $d_p/2$.

4.1 Determining an Appropriate Particle Motion Model

The study of the kinetics of particles dispersed in a moving fluid is a subcategory of multiphase flows. As the field covers physical phenomenons that are central in a wide range of modern sciences and technology applications such as combustion

engines, pollutant control, and petroleum pipelines, comprehensive work has been conducted on the subject in the recent decades [10]. The very definition of a multiphase flow is, as the name suggests, a flow mixture of different phases. A phase is the state of a matter, such as solid, liquid, or vapor. The type of multiphase flow studied in this thesis is solid particles dispersed in air. Even though the below definitions apply for different types of multiphase flows, the solid phase will only be referred to as *particles*.

Figure 4.1 shows a small particle in a moving fluid with arrows illustrating the different forces acting on the particle. The body force is typically gravity, but can also include magnetic or electrostatic forces among other. From the moving fluid, several forces act on the particle, and the presence of the particle also affects the surrounding flow, possibly making it a coupled-force problem. However, the significance of the difference forces and to which degree the presence of the particle modifies the surrounding flow is strictly problem specific and depends on the particle, fluid, and flow properties. In order to determine an appropriate model for the type of multiphase flows considered in this thesis, it is necessary to establish a basis of expressions and relations. The following definitions are taken from *Multiphase Flow with Droplets and Particles, Second Edition (2012)*, but the notation is adjusted to the nomenclature of the thesis [10].

Consider the velocity of a particle and the fluid at the corresponding location, expressed respectively as $u_{p,i}$ and $u_{f,i}$ with subscript i denoting the spatial direction. In the reference of a particle, the local Reynolds number is defined by the velocity difference between the continuous and dispersed phase as:

$$Re_p = \frac{d_p|u_{f,i} - u_{p,i}|}{\nu_f} \tag{4.1}$$

The particle response time is the approximate time for a particle to accelerate from zero to 67% of the free stream velocity. This crude estimate is deduced assuming a creeping flow around the particle with no forces acting back on the fluid. In numerical simulations the response time is critical as it both sets an upper limit for the discrete time step Δt, in addition to characterizing to which degree particles respond to changes in the velocity field. If considering a particle of diameter d_p and density ρ_p dispersed in a fluid of viscosity μ_c, the particle response time is then expressed as:

$$\tau_p = \frac{\rho_d d_p^2}{18\mu_c} \tag{4.2}$$

The Stokes number describes the response time in relation to the condition of the flow in which the particle is suspended. For high or low Stokes number, the motion of the particle is characterized either by its inertia or susceptibility to abrupt flow

changes, respectively. For a characteristic length scale D_0, such as the diameter of a tube, and a mean velocity U_0, the flow time scale can be estimated as $\tau_f = D_0/U_0$. The dimensionless Stokes number is then:

$$St = \frac{\tau_p}{\tau_f} \tag{4.3}$$

Given the presence of particles with a total volume of V_d contained in a sample volume ΔV, the volume fraction is defined as

$$\Phi_p = \lim_{\Delta V \to \Delta V_{mo}} \frac{V_d}{V} \tag{4.4}$$

where ΔV_{mo} is a sampling volume that contains a sufficient number of particles for a sound statistical representation. The volume fraction in a multiphase flow is essential when considering the interaction between the phases (e.g., fluid and particle). In *S. Elghobashi* (1994) a quantification of the significance of phase interaction in turbulent multiphase flows depending on volume fraction and relative time scales was made and presented as a map divided into four regions [14]. A re-sketch is depicted in Figure 4.2, showing the map split into four regions.

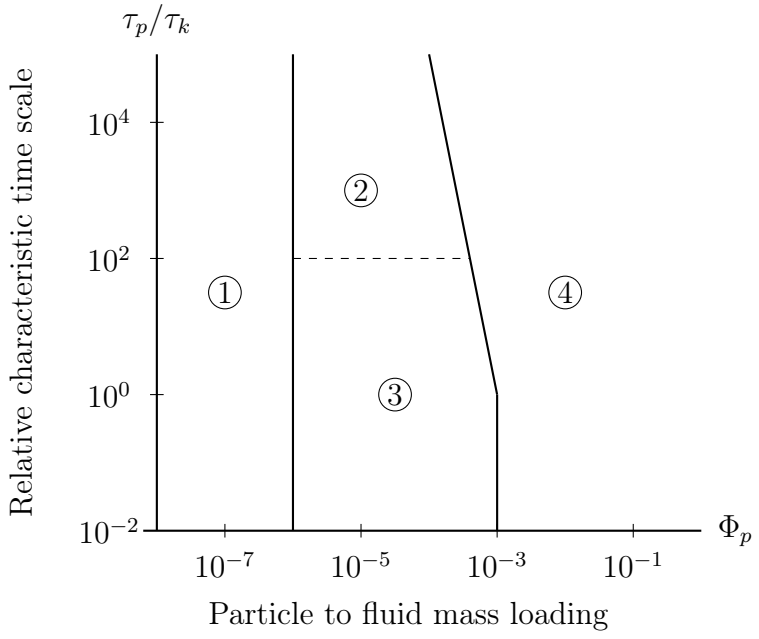

Figure 4.2: Map consisting of four regions quantifying the significance for phase interaction for turbulent flows, given mass loading and characteristic time scale.

In a multiphase problem with very low mass loading $\Phi_p < 10^{-6}$, (region 1), the flow is virtually unaltered by the presence of the particles, and a *one way coupling*

is sufficient. Given an intermediate mass loading $\Phi_p > 10^{-6}$ (region 2 and 3), the particles affect the flow in such degree that a two way coupling is necessary. For high mass loadings (region 4) the particles are so densely suspended that inter-particle interaction should also be accounted for.

The fluid-particle interaction map in Figure 4.2 is a useful tool for determining the significance of the interaction between the fluid and the particles for the problems considered in this thesis. Figure 4.3 shows the volume fractions as function of number of particles dispersed based on the lung geometry provided by *Brno lung*. The calculations were performed assuming an even distribution of particles. The horizontal, dashed line indicates the lower limit of volume fractions for which a one-way coupling is considered adequate. For the smallest particles, $d_p = 1.0\ \mu m$, a one way coupling is sufficient. The second largest particles, $d_p = 10\ \mu m$ reach the limit when 80000 particles are present in the geometry. For the largest particles the limit is already reach for less than 10000. However, based on the results in the literature [50, 34] it is expected that the largest particles barely reach beneath the oral cavity, and are thus not suitable for pharmaceutical applications. Despite that also the 10 μm particles may be within the two-way coupling region for dense local concentration, a one-way coupling is deemed adequate for the intended purpose of the thesis.

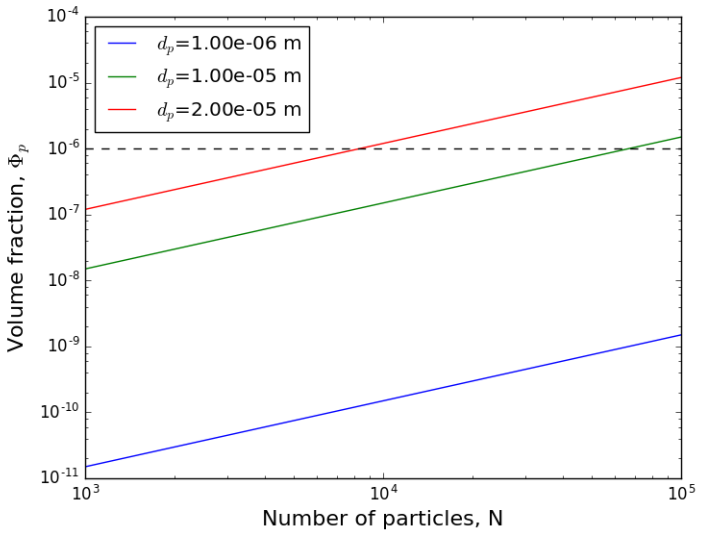

Figure 4.3: Volume fraction as function of number of particles present in the lung geometry for different particle diameters. The black, dashed line indicates the upper limit of volume fractions which allows for a one-way coupling of the fluid - particle interaction.

4.2 Development of a Particle Motion Algorithm

In this thesis, the trajectories of independent particles have been calculated with a Lagrangian-Eulerian approach by integrating the force balance on each single particle. Consider a particle with mass m_p, volume V_p, diameter d_p, and with velocity $u_{p,i}$, located at position x_p. The fluid velocity at the corresponding location is $u_{f,i}$ with density ρ_f, dynamic and kinematic viscosity μ_f and ν_f, respectively. Subscript p and f is referring to fluid and particle, respectively, and i denotes spatial direction. The shear force from the fluid on the particle surface is τ_p, while p is the pressure field, and t' is a short time after t. Following Maxey and Riley's rigorous studies in 1983 on small particles in a low Reynolds Numbers, non-uniform, unsteady flow, the full force balance law contains contributions from gravity, undisturbed flow, steady state drag, virtual mass and Basset force [10]:

$$\Sigma F_{p,i} = m_p \frac{du_{p,i}}{dt} = \underbrace{m_p f_i}_{\text{body forces}} + \underbrace{V_d(-\frac{\partial p}{\partial x_i} + \frac{\partial \tau_{ij}}{\partial x_j})}_{\text{undisturbed flow}} + \underbrace{3\pi\mu_f d_p \left[(u_{p,i} - u_{f,i}) + \frac{d_p^2}{24}\nabla^2 u_{p,i}\right]}_{\text{steady state drag}}$$
$$+ \underbrace{\frac{1}{2}\rho_f V_p \frac{d}{dt}\left[(u_{p,i} - u_{f,i}) + \frac{d_p^2}{40}\nabla^2 u_{p,i}\right]}_{\text{virtual mass}} + \underbrace{\frac{3}{2}\pi\mu_f d_p \int_0^t \left[\frac{\frac{d}{dt'}(u_{p,i} - u_{f,i} + \frac{d_p}{24}\nabla^2 u_{p,i})}{\pi\nu_f(t-t')^{1/2}}\right] dt'}_{\text{Basset term}} \tag{4.5}$$

The contribution from the undisturbed flow includes the net pressure difference acting on the particle and the shear stress on its surface. Both the contributions from the undisturbed flow and the last term in the steady state drag (Faxen force) can be neglected for small particles, as they scale with d_p^3 and d_p^2, respectively. Virtual mass accounts for the volume expelled by the presence of a particle, which acts a force on the particle when accelerated. The Basset term accounts for the temporal delay in the boundary layer on a surface in a unsteady flow. According to the studies of *Hjelmfelt and Mockros* (1966), both the virtual mass and the Basset term are negligible for $\rho_p/\rho_f < 10^{-3}$ which is approximately the density ratio between the particles considered in this thesis and that of air, and thus both terms are left out [10]. Hence, by applying the above simplifications, Eq. 4.5 is reduced to:

$$\Sigma F_{p,i} = m_p \frac{du_{p,i}}{dt} = 3\pi\mu_f d_p(u_{p,i} - u_{f,i}) + m_p f_i \tag{4.6}$$

Furthermore, Eq. 4.6 can be expressed through a drag coefficient C_d and the cross sectional area A of the particle:

$$F_{p,i} = \frac{1}{2} C_D A |u_{f,i} - u_{p,i}|(u_{f,i} - u_{p,i}) + f_i \tag{4.7}$$

Assuming spherical particles, the equation can be rewritten as:

$$F_{p,i} = \frac{3\mu m_p C_D Re_p}{4\rho_p d_p^2}(u_{f,i} - u_{p,i}) + f_i \tag{4.8}$$

or simplified to a equation of motion:

$$\frac{du_{p,i}}{dt} = \frac{C_{D,i} Re_{p,i}}{\tau_p}(u_{f,i} - u_{p,i}) + f_i \tag{4.9}$$

The particle trajectory is found by integrating the velocity:

$$\frac{dx_i}{dt} = u_{p,i} \tag{4.10}$$

Since $u_{f,i}$ is defined as the fluid velocity at the particle location at a given time, defined in a Eulerian frame, it is both a function of time and space. The location of the particles, however, are in a Lagrangian frame and thus only function of time. As a result Eq. 4.9 is on a form referred to as a Lagrangian-Eulerian formulation.

The drag coefficient C_D is an experimentally determined function of the Reynolds Number. In this thesis the definition following *Morsi and Alexander* (1972) is used, where the drag coefficient is a second order polynomial on the form [42]:

$$C_D(Re_p) = \begin{cases} \frac{24}{Re_p} & \text{for} \quad R_p < 0.1 \\ 3.6900 + \frac{22.7300}{Re_p} + \frac{0.0903}{Re_p^2} & \text{for} \quad 0.1 \leq R_p < 1.0 \\ 1.2220 + \frac{29.1667}{Re_p} - \frac{3.8889}{Re_p^2} & \text{for} \quad 1.0 \leq R_p < 10.0 \\ 0.6167 + \frac{46.5000}{Re_p} - \frac{116.67}{Re_p^2} & \text{for} \quad 10.0 \leq R_p < 100.0 \\ 0.3644 + \frac{98.3300}{Re_p} - \frac{2778}{Re_p^2} & \text{for} \quad 100.0 \leq R_p < 1000.0 \\ 0.3570 + \frac{148.620}{Re_p} - \frac{4.75 \cdot 10^4}{Re_p^2} & \text{for} \quad 1000.0 \leq R_p < 5000.0 \\ 0.4600 - \frac{490.546}{Re_p} + \frac{57.87 \cdot 10^4}{Re_p^2} & \text{for} \quad 5000.0 \leq R_p < 10000.0 \end{cases} \tag{4.11}$$

Other expressions for the drag coefficients are also used in modern softwares, such as the one proposed by *Chiller and Neumann* in 1935, which is implemented in both Ansys Fluent and OpenFoam [17, 37]. However, in this thesis Expression 4.11 is chosen as it provides the most detailed predictions for low particle Reynolds numbers.

4.2.1 A Predictor Corrector Algorithm for Solving the Equation of Motion for Particles Dispersed in a Moving Fluid

Equation 4.9 and 4.10 are ordinary differential equations on the form $u_p' = F(t, x_p, u_p)$ and can be discretized by the second order accurate Crank Nicholson scheme as:

$$\frac{u_{p,i}^{n+1} - u_{p,i}^{n}}{\Delta t} = \frac{C_{D,i}^{n+1/2} Re_{p,i}^{n+1/2}}{\tau_p} \left(u_{f,i}^{n+1/2} - u_{p,i}^{n+1/2} \right) + f_i^{n+1/2} \tag{4.12}$$

$$\frac{x_i^{n+1} - x_i^{n}}{\Delta t} = u_{p,i}^{n+1/2} \tag{4.13}$$

where superscript n denotes discrete time level. There are several difficulties in approximating the "in between" time steps such as $u_{f,i}^{n+1/2}$. A common second order approximation is to use the arithmetic mean: $u_{f,i}^{n+1/2} = \frac{1}{2}(u_{f,i}^{n+1} + u_{f,i}^{n})$, and similar for the drag coefficient and particle Reynolds number. However, $u_{f,i}^{n+1}$, the fluid velocity at the next step particle location, is not known. The same also applies for $Re_p^{n+1/2}$ and $C_{D,i}^{n+1/2}$ as both are functions of the fluid velocity. In order to circumvent this problem and still maintain a second order accuracy, a simple predictor-corrector algorithm, similar to *Heun's method*, is applied. The idea of this method is as follows:

1. Find a tentative next step particle location x_i^* by solving Eq. 4.12 and 4.13 semi explicitly, i.e, $u_{f,i}^{n+1/2} \approx u_{f,i}^{n}$ and similarly for $Re_{p,i}^{n+1/2}$ and $C_{D,i}^{n+1/2}$ (Eq. 4.14 - 4.15).

2. Find a tentative next step fluid velocity $u_{f,i}^*$ by interpolating the velocity field to position x_i^*.

3. Solve Eq. 4.12 implicitly using $u_{f,i}^{n+1/2} = \frac{1}{2}(u_{f,i}^{n+1} + u_{f,i}^{n})$ and similarly for $Re_{p,i}^{n+1/2}$ and $C_{D,i}^{n+1/2}$ (Eq. 4.16 - 4.17).

$$u^*_{p,i} = \frac{u^n_{p,i} + \Delta t f_i + \frac{\Delta t C^n_{D,i} Re^n_{p,i}}{\tau_p}\left(u^n_{f,i} - \frac{1}{2}u^n_{p,i}\right)}{1 + \frac{\Delta t C^n_{D,i} Re^n_{p,i}}{2\tau_p}} \tag{4.14}$$

$$x^*_i = x^n + \Delta t \frac{1}{2}(u^*_{p,i} + u^n_{p,i}) \tag{4.15}$$

$$u^{n+1}_{p,i} = \frac{u^n_{p,i} + \Delta t f_i + \frac{\Delta t C^n_{D,i} Re^n_{p,i}}{2\tau_p}\left(u^*_{f,i} + u^n_{f,i} - u^n_{p,i}\right)}{1 + \frac{\Delta t C^n_{D,i} Re^n_{p,i}}{2\tau_p}} \tag{4.16}$$

$$x^{n+1}_i = x^n + \Delta t \frac{1}{2}(u^{n+1}_{p,i} + u^n_{p,i}) \tag{4.17}$$

The above algorithm is depicted in Figure 4.4 for a particle moving within a FEM mesh. In the left illustration, consider, at a discrete time step, a particle with position x^n_i and instantaneous velocity $u^n_{p,i}$. At the corresponding location the instantaneous fluid velocity is $u^n_{f,i}$. Following Eq. 4.14 a tentative velocity, $u^*_{p,i}$, is found from $u^n_{f,i}$ and $u^n_{p,i}$. From Eq. 4.15 the tentative position x^*_i is found by moving one discrete time step in the direction of $\frac{1}{2}(u^n_{p,i} + u^*_{p,i})$. The flow field is interpolated to the tentative particle location x^i_p, giving $u^*_{f,i}$. In the right figure the same procedure applies, but the force contribution from the fluid on the particle is calculated from $\frac{1}{2}(u^n_{p,i} + u^*_{p,i})$ following Eq. 4.16. Finally, the next step particle position, x^{n+1}_p and the procedure repeats.

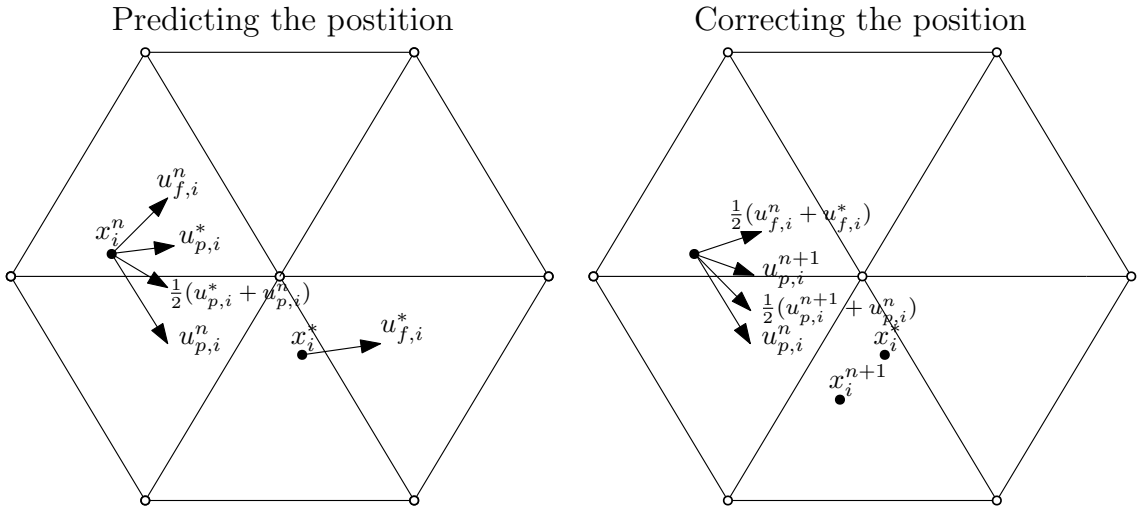

Figure 4.4: A schematic figure of predictor-corrector algorithm when solving the equation of particle motion. The left and right figures are corresponding to Eq. 4.14 and 4.16 - 4.17, respectively.

An algorithm of the implementation of Eq. 4.14 - 4.17 is depicted in Algorithm 3.

Algorithm 3 Particle Motion Algorithm

for particle in ParticleMap **do**
    x = particle.position
    u_f^n = interpolate fluid velocity to x
    for i in [spatial directions] **do**
        compute C_D from 4.11
        solve 4.14 for $u_{p,i}^*$
        solve 4.15 for x_i^*
    u_f^* = interpolate fluid velocity to x^*
    for i in [spatial directions] **do**
        compute C_D from 4.11
        solve 4.16 for $u_{p,i}^{n+1}$
        solve 4.17 for x_i^{n+1}

4.2.2 Numerical Stability of the Algorithm

The above algorithm is derived using a Crank-Nicholson scheme which is known only to be *conditionally stable*. Spurious oscillations in the particle velocity was observed when testing Algorithm 3. Since this artificial effect was typical for small particles when the discrete time step Δt was relatively large, the existence of a stability relation between Δt and the particle response time τ_p was hypothesized.

In order to test this working hypothesis, a simple experiment was carried out. Particles of different diameters spanning the range studied in this thesis was accelerated from rest in a constant 2D velocity field $\mathbf{u}_f = (U_0, 0)$. For each particle diameter the test was performed with increased Δt until the criteria 4.18 - 4.19 were not met.

$$|\mathbf{u}_p^n| > |\mathbf{u}_f^n| \tag{4.18}$$

$$|\mathbf{u}_p^{n+1}| < |\mathbf{u}_p^n| \tag{4.19}$$

From a least square fit to the instability limit Δt_{lim} as a function of particle diameter d_p, the following relation was found:

$$\Delta t < 2.0119\tau_p + 1.4929 \cdot 10^{-5}\ s \tag{4.20}$$

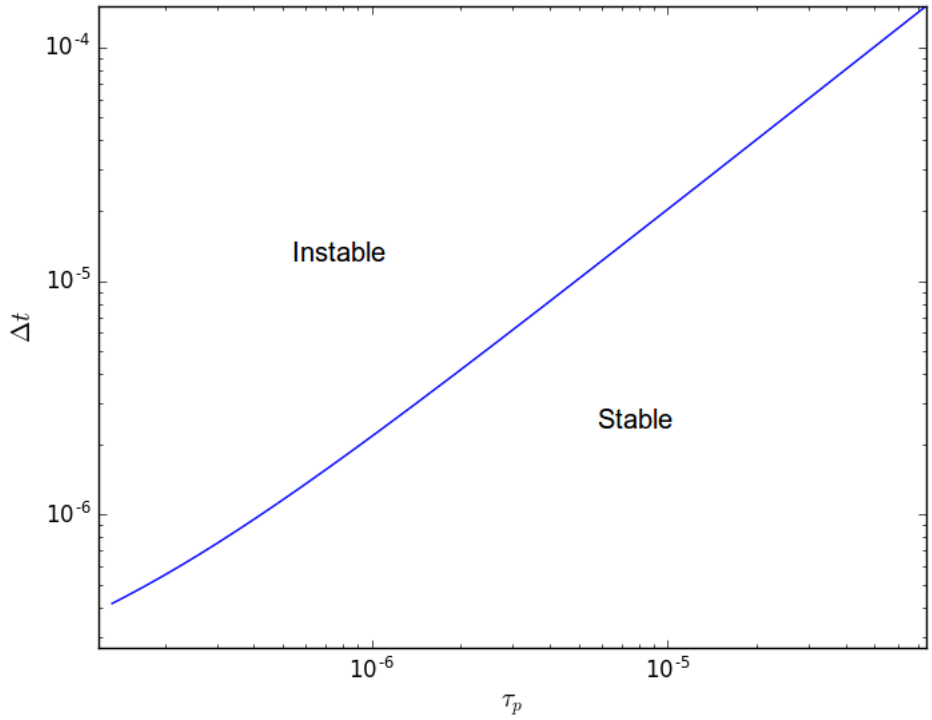

Figure 4.5: Stability relation between response time τ_p and temporal resolution Δt for the Particle Motion Algorithm.

4.3 The Particle Tracking Framework

The equation of particle motion algorithm presented in Section 4.2.1 is implemented in the framework of the module *LagrangianParticle.py* found in the open source software *fenicstools* [43]. This module contains a structure for storing information about particle properties and methods for reading and interpolating velocity fields to point locations within the mesh. In addition, *LagrangianParticle.py* utilizes parallelization through *MPI for Python* (mpi4py) [11], by assigning different parts of the mesh to each processor.

In *LagrangianParticle.py*, each particle is defined through an instance of a class *Particle*, containing information of the current position, velocity, and other properties of the particle. Furthermore, a class *CellParticleMap* contains a dictionary that links individual particle to the cell in which they are located, such that the velocity field can be interpolated from the surrounding nodes. After a new particle position has been computed, its presence within the cell is revisited. If the particle is no longer present in the cell, the neighboring cells will first be checked for its presence, significantly speeding up the relocation process compared to checking the full mesh. Only if a particle is not located within any of the neighboring cells the remaining cells are inspected.

In the initial configuration of the *LagrangianParticle.py*, inertia is ignored and the particles are moved according to the path lines of the velocity field. As particle inertia is only negligible for $\tau_p \to 0$, it was therefore deemed necessary to implement force balance integrating algorithm.

In this thesis the following changes to *LagrangianParticle.py* were performed:

- Adding particle physics by the implementation of Algorithm 3.
- Functionality for saving particle position and velocity to file for post processing and possibility of restarting simulations.
- Deposition criterion: defining particles as deposited and remove from particle map when a given distance to the domain boundary is reached.

Chapter 5

Verification and Validation of the Particle Tracking Framework

5.1 Verification

In order to verify that the equation of particle motion algorithm is correctly implemented, convergence rate tests were carried out. As the particle equations of motion (Eq.4.9 - 4.10) were derived within a Lagrangian frame, they are functions only with respect to time. Furthermore, the equations are discretized using the Crank-Nicholson scheme which is know to be second order accurate [31]. The order of accuracy reflects the polynomial degree of the residual in the Taylor expansion from which the finite difference schemes were derived. By subtracting the exact from the numerical solution of the equation, we are left with the truncation error. As the Taylor residual is the leading order term, we expect the truncation error on the form:

$$E = C\Delta t^r \tag{5.1}$$

where C is an constant and r the *rate-of-convergence*. By computing a series of errors E_i for different temporal resolutions Δt_i, the rate-of-convergence is found as

$$r_i = \frac{log(\frac{E_{i+1}}{E_i})}{log(\frac{\Delta t_{i+1}}{\Delta t_i})} \tag{5.2}$$

A wide range of values for Δt_i should be used to verify that the *rate-of-convergence* is consistent.

5.2 Rate-of-Convergence Tests for the Particle Motion Algorithm

Three problems, each specifically involving different parts of the Equations of Particle Motion algorithm, was considered in the rate-of-convergence tests:

1. Free falling particle accelerated by gravity in fluid at rest.
2. Particle accelerated by a *temporally changing* velocity field $\mathbf{u}_f = (At, 0)$ where A is a constant of dimension $[\frac{m}{s^2}]$.
3. Particle accelerated by a *spatially changing* velocity field $\mathbf{u}_f = (Bx, 0)$ where B is a constant of dimension $[\frac{1}{s}]$.

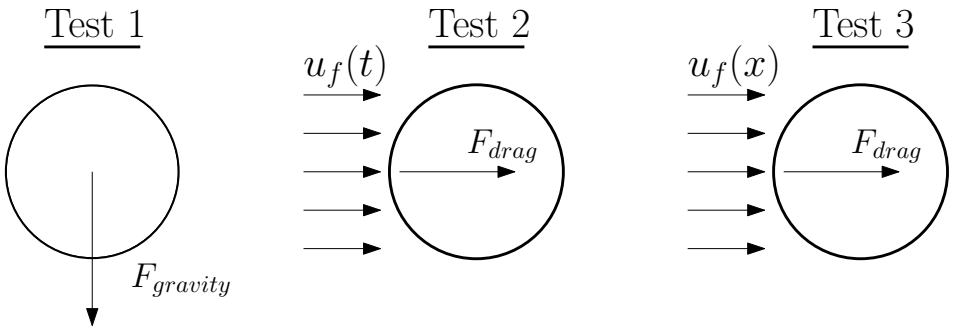

Figure 5.1: Schematic drawing of the three problems for verifying the particle equation of motion algorithm.

Equation 4.9 is non-linear for particle Reynolds numbers above 0.1. Thus, in order to derive simple analytical solutions for Test 1 and 2, the particle Reynolds number was forced below 0.1, thus making the equation linear. Since the tests only involve translation on one direction, the corresponding problems can be described by the one dimensional equations. As no analytical solution was found for Test 3, a *trusted numerical scheme* was used in order to provide a "reference solution".

5.2.1 Test 1

The first problem verifies that drag and the body force term is correctly implemented. For a free falling particle in a fluid at rest, Eq. 4.9 and 4.10 simplifies to:

$$\frac{du_{p,z}(t)}{dt} = -\frac{24}{\tau_p}u_{p,z}(t) - g_z, \qquad \frac{dx_z(t)}{dt} = u_{p,z}(t) \tag{5.3}$$

Initiating the particle at rest from position $x_z = 0$ gives the following analytical solution for the velocity and position:

$$u_{p,z}(t) = \frac{g\tau_p}{24}\left(1 - \exp(-\frac{24t}{\tau_p})\right) \tag{5.4}$$

$$x_{p,z}(t) = \frac{g\tau_p}{24}\left(t - \frac{\tau_p}{24}\exp(-\frac{24t}{\tau_p})\right) - \frac{g\tau_p^2}{24} \tag{5.5}$$

The problem was simulated for a wide range of time steps for a particle with diameter 20 μm and compared with the analytical solution. Table 5.1 shows the obtained results with the (expected) convergence rates marked in bold font.

Δt	E_u	$\mathbf{r}_u$	E_{pos}	$\mathbf{r}_{pos}$
$5.00 \cdot 10^{-5}$	$1.73 \cdot 10^{-4}$	-	$3.24 \cdot 10^{-11}$	-
$2.50 \cdot 10^{-5}$	$4.34 \cdot 10^{-5}$	**2.00**	$8.09 \cdot 10^{-11}$	**2.00**
$1.25 \cdot 10^{-5}$	$1.09 \cdot 10^{-5}$	**2.00**	$2.02 \cdot 10^{-11}$	**2.00**
$6.25 \cdot 10^{-6}$	$2.71 \cdot 10^{-6}$	**2.00**	$5.05 \cdot 10^{-12}$	**2.00**
$3.1250 \cdot 10^{-6}$	$6.79 \cdot 10^{-7}$	**2.00**	$1.26 \cdot 10^{-12}$	**2.00**
$1.5625 \cdot 10^{-6}$	$1.70 \cdot 10^{-7}$	**2.00**	$3.16 \cdot 10^{-13}$	**2.00**
$7.8125 \cdot 10^{-6}$	$4.24 \cdot 10^{-8}$	**2.00**	$7.96 \cdot 10^{-14}$	**1.99**

Table 5.1: Results from Test 1: Convergence rates computed from the problem of a large particle ($d_p = 20\,\mu m$) in free fall. Rate of convergence for the velocity and position $\mathbf{r}_u$ and $\mathbf{r}_{pos}$, respectively.

5.2.2 Test 2

The second problem verifies that the drag contribution from a moving fluid is correctly implemented. For a single particle suspended in the fluid field $\mathbf{u}_f(t) = (At, 0)$, experiencing no body forces, Eq. 4.9 and 4.10 simplifies to:

$$\frac{du_{p,x}(t)}{dt} = \frac{24}{\tau_p}(At - u_{x,p}(p(t)), \qquad \frac{dx_x(t)}{dt} = u_{p,x}(t) \tag{5.6}$$

$$\tag{5.7}$$

Initiating the particle at rest from position $x_x = 0$ gives the analytical solution:

$$u_{p,i}(t) = A\left(t + \frac{\tau_p}{24}(\exp(-\frac{24t}{\tau_p}) - 1)\right) \tag{5.8}$$

$$x_{p,i}(t) = A\left(\frac{1}{2}t^2 - \frac{\tau_p}{24^2}(\tau_p \exp(-\frac{24t}{\tau_p}) + 24t)\right) - \frac{A\tau_p^2}{24^2} \tag{5.9}$$

The problem was simulated for a large $d_p = 20\ \mu m$ and a small $d_p = 3\ \mu m$ particle. Again, the expected convergence rates were found, marked in bold font in Table 5.2 - 5.3.

Δt	E_u	$\mathbf{r}_u$	E_{pos}	$\mathbf{r}_{pos}$
$5.00 \cdot 10^{-5}$	$1.22 \cdot 10^{-2}$	-	$2.44 \cdot 10^{-8}$	-
$2.50 \cdot 10^{-5}$	$3.43 \cdot 10^{-3}$	**1.83**	$5.74 \cdot 10^{-9}$	**2.09**
$1.25 \cdot 10^{-5}$	$9.10 \cdot 10^{-4}$	**1.91**	$1.39 \cdot 10^{-9}$	**2.05**
$6.25 \cdot 10^{-6}$	$2.25 \cdot 10^{-4}$	**1.96**	$3.42 \cdot 10^{-10}$	**2.02**
$3.1250 \cdot 10^{-6}$	$5.96 \cdot 10^{-5}$	**1.98**	$8.49 \cdot 10^{-11}$	**2.01**
$1.5625 \cdot 10^{-6}$	$1.50 \cdot 10^{-5}$	**1.99**	$2.11 \cdot 10^{-11}$	**2.01**
$7.8125 \cdot 10^{-6}$	$3.78 \cdot 10^{-5}$	**1.99**	$5.27 \cdot 10^{-12}$	**2.00**

Table 5.2: Results from Test 2: Convergence rates computed from the problem of a large particle ($d_p = 20\,\mu m$) accelerated by a *temporarily changing* velocity field. Rate of convergence for the velocity and position $\mathbf{r}_u$ and $\mathbf{r}_{pos}$, respectively.

Δt	E_u	$\mathbf{r}_u$	E_{pos}	$\mathbf{r}_{pos}$
$2.50 \cdot 10^{-5}$	$1.02 \cdot 10^{-5}$	-	$7.81 \cdot 10^{-8}$	-
$1.25 \cdot 10^{-5}$	$4.39 \cdot 10^{-6}$	**1.21**	$1.95 \cdot 10^{-8}$	**2.00**
$6.25 \cdot 10^{-5}$	$1.34 \cdot 10^{-6}$	**1.71**	$4.88 \cdot 10^{-9}$	**2.00**
$3.125 \cdot 10^{-6}$	$3.64 \cdot 10^{-7}$	**1.88**	$1.22 \cdot 10^{-9}$	**2.00**
$1.5625 \cdot 10^{-6}$	$9.45 \cdot 10^{-8}$	**1.95**	$3.05 \cdot 10^{-10}$	**2.00**
$7.8125 \cdot 10^{-6}$	$2.41 \cdot 10^{-8}$	**1.97**	$7.62 \cdot 10^{-11}$	**2.00**
$3.90625 \cdot 10^{-6}$	$6.07 \cdot 10^{-9}$	**1.99**	$1.90 \cdot 10^{-11}$	**2.00**

Table 5.3: Results from Test 2: Convergence rates computed from the problem of a small particle ($d_p = 3\ \mu m$) accelerated by a *temporarily changing* velocity field $\mathbf{u}_f = (At, 0)$. Rate of convergence for the velocity and position $\mathbf{r}_u$ and $\mathbf{r}_{pos}$, respectively.

5.2.3 Test 3

Both test 1 and 2 successfully computed the expected convergence rates. However, both tests has the shortcoming as neither properly tests the predictor step of the algorithm. Consider Eq. 4.14; if u_f is constant in the spatial domain, $x^* = x^{n+1}$, and the effectiveness of the predictor step is not tested. Furthermore, as the motion of the fluid and particles are described in different frames - Eulerian and Lagrangian, respectively, finding an analytical solution for the motion of a particle moved by a *spatially changing* velocity field is challenging. Therefore, instead of computing the error by comparing numerical to analytical solution, a *trusted numerical scheme* was used in order to produce a "reference" solution.

For a single particle suspended in the fluid field $\mathbf{u}_f(t) = (Bx, 0)$, experiencing no body forces, Eq. 4.9 and 4.10 simplifies to:

$$\frac{du_{p,x}(t)}{dt} = \frac{24}{\tau_p}(Bx - u_{x,p}(p(t)), \qquad \frac{dx_x(t)}{dt} = u_{p,x}(t) \tag{5.10}$$

Eq. 5.10 was solved with a first order, forward difference scheme with a temporal resolution of magnitude 10^{-11} s - approximately a millionth of the ones in the refinement test. The reference scheme, shown in Listing 5.1 below, was prior to the computations verified as first order accurate on Test 1 and 2.

Listing 5.1: Forward Difference Scheme for Eq. 5.10

```
def drag_model_1(u_p, u_f, g, dt):
  for i in range(len(u_p[:])):
          u_p[i] = u_p[i] + dt*K1*(u_f[i] - u_p[i]) + dt*g[i]
  return u_p[:]
```

The results with convergence rates in bold font are presented in Table 5.4. For $\Delta t \to 1 \cdot 10^{-6}$ the convergence rates appears to become somewhat irregular, which may be explained by recalling the error estimate in Eq. 5.1. The error of the "reference solution" scales as $E_{ref} \approx 10^{-11}$, whereas the scheme under assessment scales as $E_2 \approx 10^{-6*2} = 10^{-12}$. Thus, when $\Delta t \to 1 \cdot 10^{-6}$, the equation of particle motion algorithm is more accurate than the "reference" solution, due to the higher order.

Table 5.5 shows the convergence rates with the *corrector step disabled*, which, as expected, causes a drop in the convergence rate and demonstrating the benfit of the implemented predictor-corrector procedure.

Δt	E_u	r_u	E_{pos}	r_{pos}
$5.00 \cdot 10^{-5}$	$3.07 \cdot 10^{-3}$	-	$2.27 \cdot 10^{-6}$	-
$2.50 \cdot 10^{-5}$	$7.84 \cdot 10^{-4}$	**1.97**	$5.69 \cdot 10^{-6}$	**2.00**
$1.25 \cdot 10^{-5}$	$1.98 \cdot 10^{-4}$	**1.99**	$1.42 \cdot 10^{-6}$	**2.00**
$6.25 \cdot 10^{-6}$	$4.88 \cdot 10^{-4}$	**2.02**	$3.55 \cdot 10^{-7}$	**2.00**
$3.1250 \cdot 10^{-6}$	$1.13 \cdot 10^{-5}$	**2.10**	$8.90 \cdot 10^{-8}$	**2.00**
$1.5625 \cdot 10^{-6}$	$1.95 \cdot 10^{-6}$	**2.54**	$2.23 \cdot 10^{-8}$	**1.99**
$7.8125 \cdot 10^{-6}$	$4.01 \cdot 10^{-7}$	**2.28**	$5.67 \cdot 10^{-9}$	**1.98**

Table 5.4: Results from Test 3: Convergence rates computed from the problem of a large particle ($d_p = 20\mu m$) accelerated by a *spatially changing* velocity field $\mathbf{u}_f = (Bx, 0)$. Rate of convergence for the velocity and position $\mathbf{r}_u$ and $\mathbf{r}_{pos}$, respectively.

Δt	E_u	r_u	E_{pos}	r_{pos}
$5.00 \cdot 10^{-5}$	$3.18 \cdot 10^{-3}$	-	$1.90 \cdot 10^{-4}$	-
$2.50 \cdot 10^{-5}$	$8.32 \cdot 10^{-4}$	**1.93**	$1.12 \cdot 10^{-4}$	**0.75**
$1.25 \cdot 10^{-5}$	$2.13 \cdot 10^{-4}$	**1.97**	$6.08 \cdot 10^{-5}$	**0.89**
$6.25 \cdot 10^{-6}$	$5.38 \cdot 10^{-5}$	**1.99**	$3.15 \cdot 10^{-5}$	**0.95**
$3.1250 \cdot 10^{-6}$	$1.32 \cdot 10^{-5}$	**2.00**	$1.61 \cdot 10^{-5}$	**0.97**
$1.5625 \cdot 10^{-6}$	$3.29 \cdot 10^{-6}$	**2.03**	$8.10 \cdot 10^{-6}$	**0.99**
$7.8125 \cdot 10^{-6}$	$7.42 \cdot 10^{-7}$	**2.15**	$4.07 \cdot 10^{-5}$	**0.99**

Table 5.5: Results from Test 3 with *corrector step disabled*: Convergence rates computed from the problem of a large particle ($d_p = 20\ \mu m$) accelerated by a *spatially changing* velocity field $\mathbf{u}_f = (Bx, 0)$. Rate of convergence for the velocity and position $\mathbf{r}_u$ and $\mathbf{r}_{pos}$, respectively. Note the drop of convergence rate.

5.3 Validation: Particle deposition in a 90 degree tube bend

The previous section verified that the equation of particle motion algorithm is correctly implemented and produces results of the expected order of accuracy. The next step is to perform a test case that allows for the comparison with established experimental and numerical results in order to validate the algorithm. Such a test case should contain similar characteristics as the inhaled particle deposition problem so that the results can be extrapolated to the full scale problem. *Pui et. al* (1987) [53] performed an extensive series of experiments releasing particles of different sizes through bent tubes of varying diameters and curvatures. The Reynolds numbers varied between 1000 and 10000, hence including both laminar and turbulent cases. Previous studies have shown that the particle deposition in bends has a negligible dependency of the curvature ratios, R_c, between 5-30, which is defined as the inscribed radius of the bend divided with the radius of the tube [23]. The study of *Pui et. al* showed that Reynolds number had no impact on the deposition ratio in the turbulent regime and that particle inertia (Stokes number) is the dominant factor.

In this section a numerical simulation of one of the experiments carried out by Pui. et. al. has been performed with the aim of comparing the obtained results. In addition, results following two other numerical studies, *Breuer et. al.* (2006) and *Tsai and Pui* (1990) have also been considered [7, 62].

The motion of fluids running through bends is characterized by the Dean number, which is a dimensionless quantity representing the ratio of the square root of the centripetal and viscous forces to the inertial forces [53]. Given a flow with Reynolds number Re running through a bent pipe with dimensionless curvature ratio R_c, the Dean number is expressed as:

$$De = \frac{Re}{\sqrt{R_c}} \tag{5.11}$$

5.3.1 Method

In this thesis the test case was performed with a tube diameter of $D = 8.51\ mm$, Reynolds number $Re = 1000$, and curvature radius of the bend $R_0 = 5.6D/2$, yielding the Dean number $De = 422.5$. Based on the magnitude of the Dean number, the flow field was expected to be characterized by two counter rotating vortices, skewed towards the inside of the bend. The flow field simulation was performed with *Oasis* on an unstructured mesh created with *ICEM-CFD* (Ansys Inc., Canonsburg, PA, USA), consisting of 6 million cells with a 6 layer thick boundary layer at the walls. Figure 5.2b shows a cross sectional slice of the mesh. The

boundary conditions were set to parabolic velocity inlet profile, no-slip condition at the walls, and zero pressure at the outlet.

A total of 30000 particles of each diameter was released in the experiment over 3000 time steps, crudely corresponding to one flow-through time (0.06 s) with the time step set to $\Delta t = 2{\cdot}10^{-5}$. The properties of the released particles are presented in 5.6. All the particles were well within the empirical stability criterion for the equation of particle motion algorithm (cf. Figure 4.5). Particles were considered as deposited if a next step position x_i^n was located outside the domain boundaries. The particles depositing at the outlet surface were considered escaped. At each time step the flow field was sampled along four lines consisting of 250 equally spaced sample locations using *fenicstools*. Two of the lines were located orthogonal to each other at the particle release plane ($y = 0\ mm$) and similarly at the end of the bend ($z = -23.8\ mm$).

Particle properties			
St	$d_p[\mu m]$	$\tau_p[ms]$	$\rho_p[\frac{kg}{m^3}]$
0.10	8.52	0.21	895
0.17	11.13	0.36	895
0.23	12.94	0.49	895
0.36	16.90	0.77	895
0.44	17.90	0.94	895
0.70	22.58	1.49	895

Table 5.6: Properties of the particles released in the bend

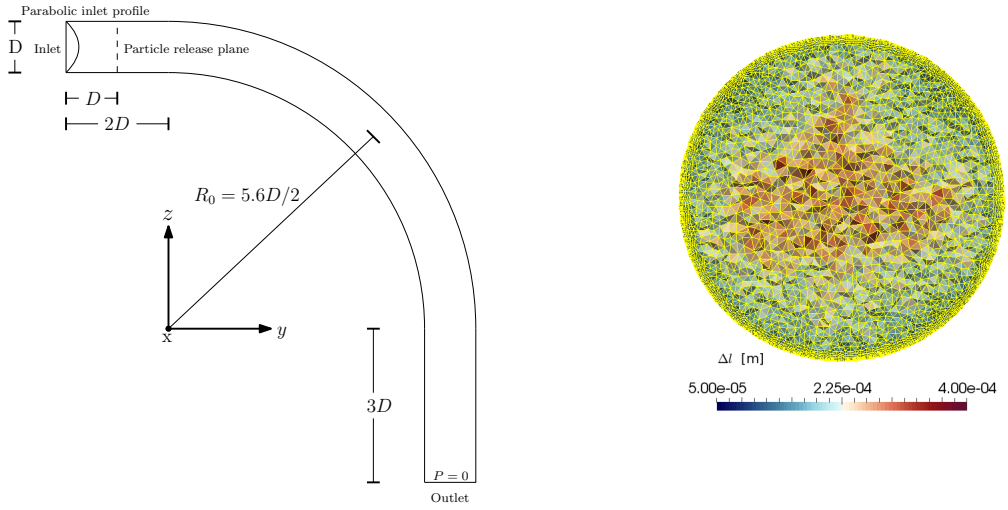

(a) Schematic figure of the tube

(b) Mesh

Figure 5.2: Schematic figure of the tube and cross sectional slice of the mesh at the particle release plane. Note the very fine mesh resolution at the boundary.

5.3.2 Flow field

In order to ensure that the flow field is fully developed before the particles were released, the simulation was run until the velocity field, measured at the four cross sectional locations, showed convergence. Figure 5.3 shows mean velocity profiles based on 1000 samples taken at these probes starting at time step 10000 and 15000. Since no distinction can be seen between the curves following the two different starting time steps at any of the locations, it is evident that the flow has reached a steady state at time step 15000 (0.3 s). Figure 5.5a shows the Q-criterion visualizing the two counter rotating vortices that are described in the literature [7, 53]. The eddies are a result of the fluid moving faster in the outer bend, thus creating a pressure gradient that forces the slower moving fluid outwards in a recirculating motion. Figure 5.4 indicates the direction of rotation of the vortices.

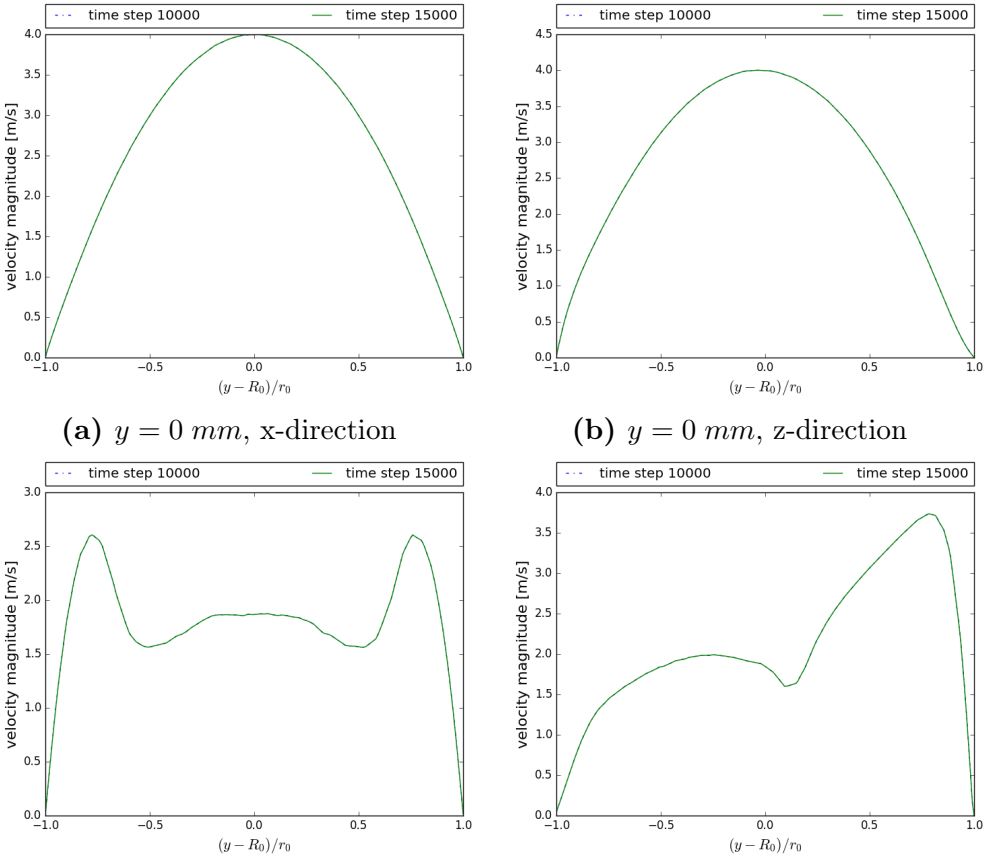

(a) $y = 0\ mm$, x-direction

(b) $y = 0\ mm$, z-direction

(c) $z = -23.8\ mm$, x-direction

(d) $z = -23.8\ mm$, y-direction

Figure 5.3: Mean velocity cross sectional profiles at the particle release plane ($y = 0\ mm$) and at the end of the bend ($z = -23.8\ mm$). The average of the first 1000 time step and the average of time step 5000 - 6000 is compared in each window but are not distinguishable as the flow is fully developed.

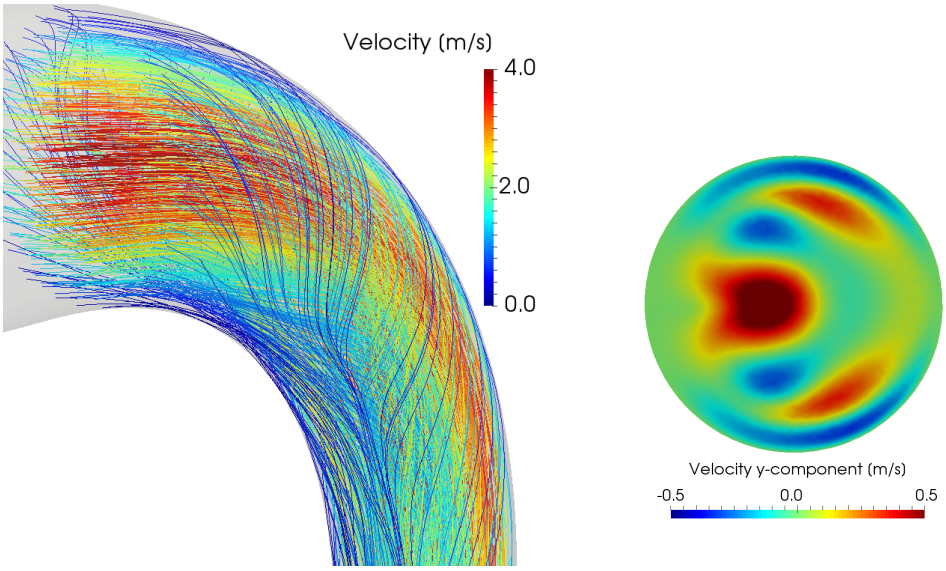

(a) Streamlines of the instantaneous velocity.

(b) Cross sectional slice of the tube downstream of the bend displaying the y-component of the velocity.

Figure 5.4: Streamlines and velocity y-component showing that the fluid is moving from outside of the bends along the wall before being pushed back out through the center.

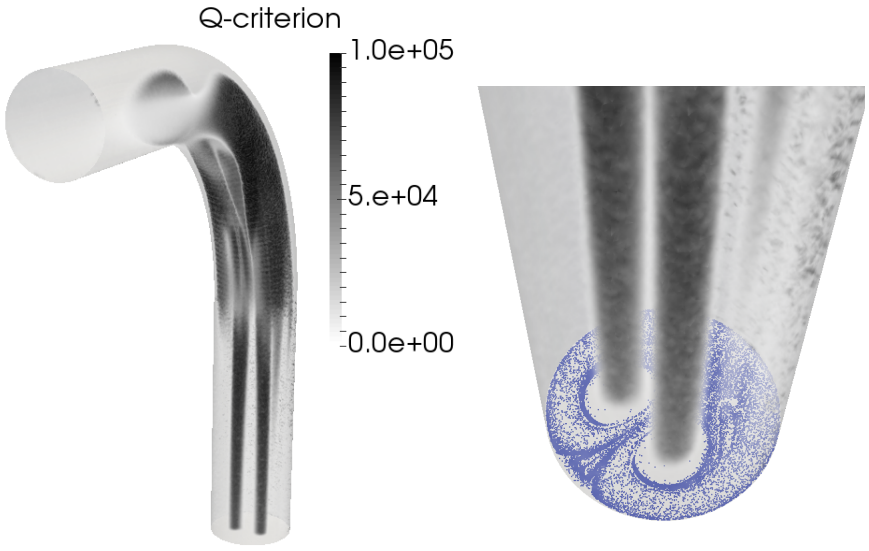

(a) Q-criterion for the velocity field showing the two counter rotating vortices slightly skewed towards the inner walls.

(b) Particle pattern at the outlet neatly matching the counter rotating vortices. $St = 0.17$

Figure 5.5

5.3.3 Results

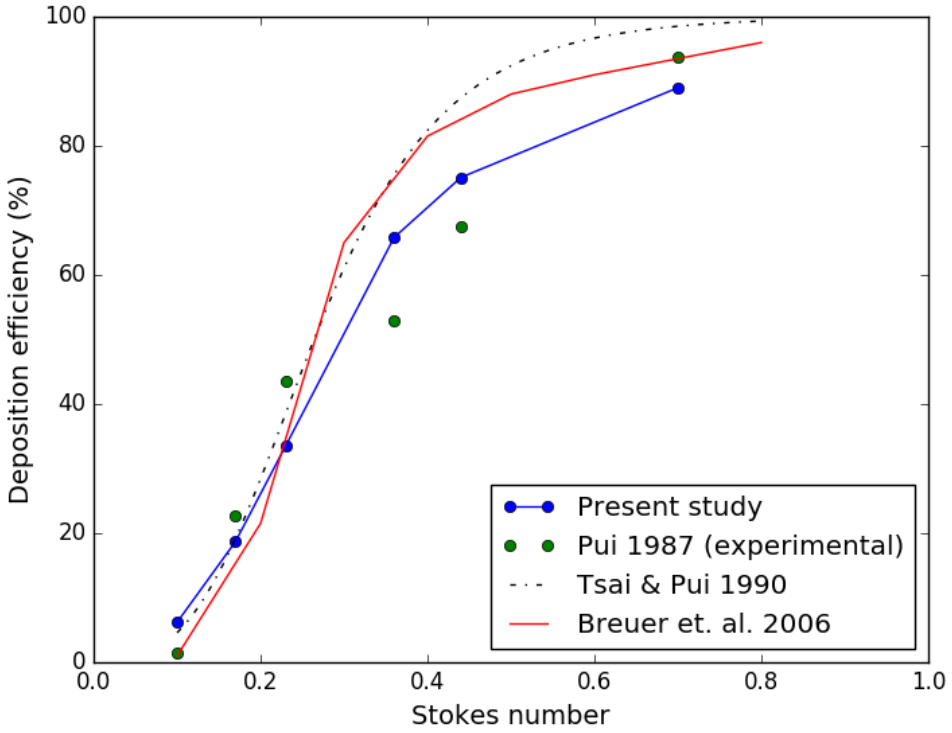

Figure 5.6: Comparison of deposition efficiency between different studies.

	Deposition fraction	
St	Pui. et. al (experimental)	Present simulation
0.10	1.5	6.2
0.17	22.7	18.7
0.23	43.5	33.5
0.36	53.0	65.8
0.44	67.6	75.1
0.70	93.7[1]	89.0

Table 5.7: Deposition fraction for particles depending on the Stokes numbers. Experimental (Pui. et. al.) and numerical results. [1](from experiment with $D = 3.95\ mm$ and $r_0 = 2.7$).

The deposition efficiency as function of Stokes number is presented in Figure 5.6 together with the results obtained in the three other studies. In addition to the already mentioned experiment by *Pui et. al*, two other numerical studies are included. The best overall agreement of results are between *Tsai* and *Breuer*.

At Stokes numbers around 0.4-0.5 all the numerical methods over predict the deposition efficiency compared with the experimental results, but the present study only to a lesser degree. At Stokes number 0.7 the present study shows the lowest deposition efficiency. However, if considering relative error, the discrepancy is less significant than for the smallest Stokes numbers. In Figure 5.8 a particular change in the deposition pattern can be seen for Stokes numbers larger than 0.23. The smallest particles do not have the inertia to escape the centrifugal forces and are only deposited at the inside of the bend with some offset from the middle. For particles with Stokes number 0.36 and larger this behavior is changed and the deposition occurs predominately on the outside bend.

5.3.4 Discussion

The general trend of underprediction of particle deposition in the current study compared with the two other numerical studies, may be seen in correlation to how the deposition criterion has been treated. As explained in Section 5.3.1, in the present study, a particle is considered deposited if its next step velocity x^{n+1} is outside the mesh domain. In the studies by *Breuer et al*, and *Tsai and Pui*, particle deposition was modeled by a control volume method, where a particle is considered deposited if being closer to the wall than to the present cell center. Furthermore, in *Tsai and Pui*, simulations were initially performed with high Stokes number particles. Based on the simulations of the high Stokes number particles, cells at the inlet that did not contain deposited particles were defined as non-impact control volumes. In the subsequent simulations, smaller particles initiated in the non-impact control volumes were assumed not to deposit, and thus removed from the simulation. In both papers, the details and uncertainties regarding the control volume method are not outlined, but the reader is referred to *Tsai et. al.* (1988), which, however, is not available online.

Figure 5.7 show $St = 0.36$ particles that are "trapped" in the viscous sublayer very close to the boundary at $T = 0.15\ s$. Similar behavior could be seen for the other particles as well. Given the control volume approach for determining deposition, some of these particles may have been considered deposited in the other studies, depending on the thickness of the boundary layer cells. *Breuer et al.* reports that the innermost cells has an non dimensional thickness of $y^+ = 0.70$, but it is not specified from which flow condition this is derived. In addition to different approaches for particle deposition modeling, the flow fields were also computed using different temporal and spatial resolutions, which despite the low Reynolds number may have had some impact on the results. *Breuer et. al.* simulated the flow with a *finite volume method* on a block structured curvilinear grid consisting of $2.28 \cdot 10^6$ cells, *Tsai and Pui* used a mesh in toroidal coordinates with 17, 38 and 25 cells in radial, angular, and streamvise direction, respectively.

Finally, the experimental method of *Pui et al.* was reported to have an expected uncertainty of 5%.

Figure 5.7: Particles moving very slowly in the viscous sublayer close to the boundary at $T = 0.15s$

5.3.5 Conclusion

In Section 5.2 the desired second order convergence rate was measured following three different test problems. The validation test case showed good results given the uncertainties discussed in the previous section. It is thus concluded that the equation of particle motion algorithm is correctly implemented in the particle tracking framework of this study.

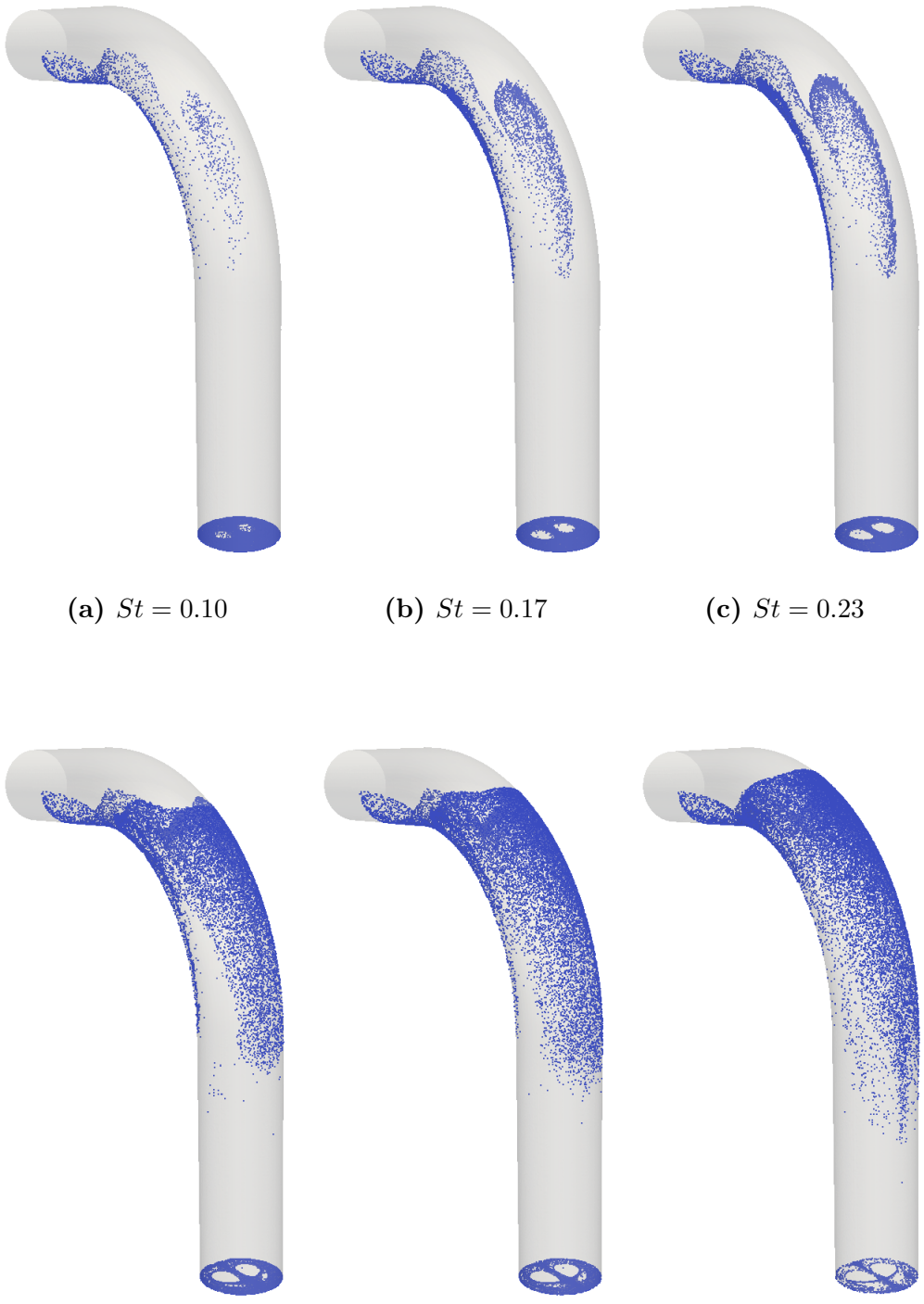

(a) $St = 0.10$ **(b)** $St = 0.17$ **(c)** $St = 0.23$

(d) $St = 0.36$ **(e)** $St = 0.44$ **(f)** $St = 0.70$

Figure 5.8: The deposition pattern for the six experiments. The particles deposited at the outlet are considered escaped.

Chapter 6

A Computational Study of the Air Flow in a Realistic Model of the Human Respiratory System

6.1 Aim: Determining Appropriate Numerical Resolution

In Section 4.1 it was argued that a one way coupling is sufficient for modeling the motion of the considered particles. Thus, the flow field could be computed separately without any interaction from the particles. In this chapter a refinement test was carried out with the aim of finding a combination of temporal and spatial resolution producing a reasonably well resolved flow field at a moderate computational cost. Sensitivity to temporal and spatial resolution was evaluated by the following metrics:

- Mean velocity profiles.
- Root-mean-square velocity perturbation profiles (turbulence rms).
- Kolmogorov scales versus spatial and temporal resolutions.
- Turbulence energy spectrum.

With the settings found appropriate in the refinement study, the simulation was extended and used to model the motion of inhaled particles, which is described in Chapter 7.

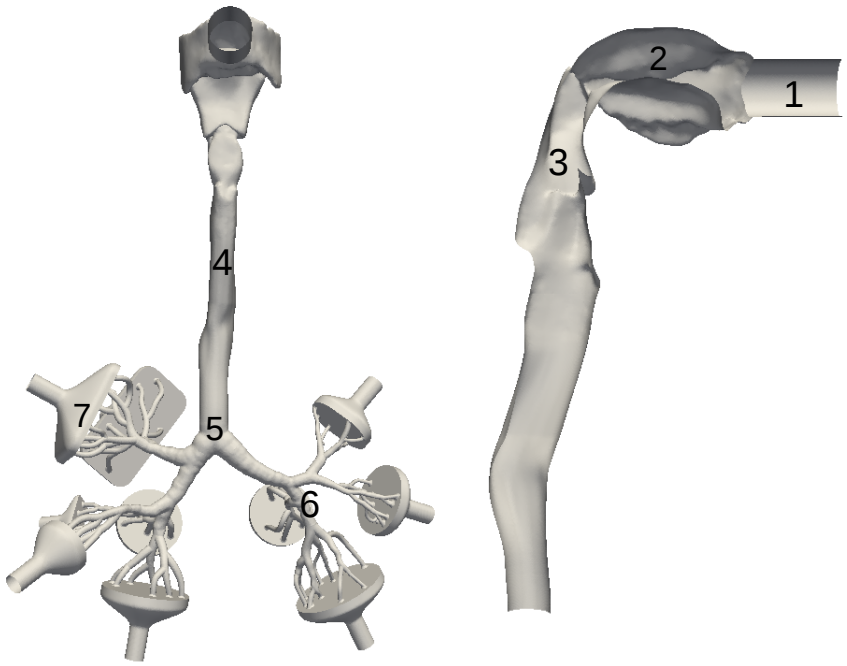

Figure 6.1:) The digital model of the upper human respiratory system used in this thesis, with prominent geometrical and anatomical features pinpointed.
Inlet - 1), Oral cavity - 2), Epiglottis - 3), Trachea - 4), Bifurcation - 5), Bronchi - 6), Outlet container - 7)

6.2 Anatomical Features of the Human Respiratory System and a Plausible Model

Figure 6.1 shows the digitalized surface model used for the computations carried out in this thesis. The model consists of the oral cavity, trachea and the bronchial three, which together constitutes the upper human respiratory system. The mouth is extended with a cylindrical inlet section (1) which replicates a inhalation drug delivery device. The oral cavity (2) is connected to the lungs through the trachea (4) which inside the chest splits into the bronchi (5). Both the trachea and the bronchi are radially asymmetrical, causing turbulent-like flow at even moderate Reynolds Numbers ($Re < 2300$) [33]. The epiglottis (3), located in the upper part of the *trachea* is a sharp edge that can close the airways, preventing food from entering the airways. Apart from its obvious important anatomical function, the epiglottis has a significant impact on the flow field as its sharp, asymmetrical shape enhance velocity instabilities in the trachea.

A particular characteristic of the geometry studied in this thesis, is the merging of the 7th generation bronchi into 10 cone shaped containers (7), which originates from the physical model used *in vitro* experiments.

From a geometrical point of view, the perhaps most prominent feature of the human respiratory system is the progressive branching of the tract. The branching of the bronchi progresses into the bronchioles which, at approximately the 17th generation, ends up in the alveolar sacks where the inhaled gas is exchanged through diffusion. The change of the bronchial radii between bifurcations is governed by Murry's law [45]. Given r_p and r_{d_i} are the radii of parent and daughter bronchi branch number i, respectively, Murray's law is expressed as

$$r_p^3 = \sum_i r_{d_i}^3 \tag{6.1}$$

The diameter of the trachea is approximately 1.5 cm. From 6.1 we can deduce that the 7th generation bronchus has a diameter of around 2 mm while the 10th generation less than 1 mm, which is a complicating factor when creating models of the human respiratory system as it requires very high image resolutions to capture.

There are mainly two approaches for creating a model of the human respiratory system, either by casting of cadaver lungs or digital imaging of live volunteers. However, it is difficult to obtain sufficient image quality of the bronchi beyond the third generation, due to the combination of small length scales and heart beating. The model used in *Brno Lungs* was produced by combining the two mentioned methods: Computer tomography (CT) scans were taken of an excised lung down to the 7th generation bronchi, and then merged with a digitalized cast of an oral cavity (*The A Model*) from Lovelace Respiratory Research Institute, Albuquerque [69]. A detailed description of the development of the model is presented in *Lizal et al.* (2011) [35].

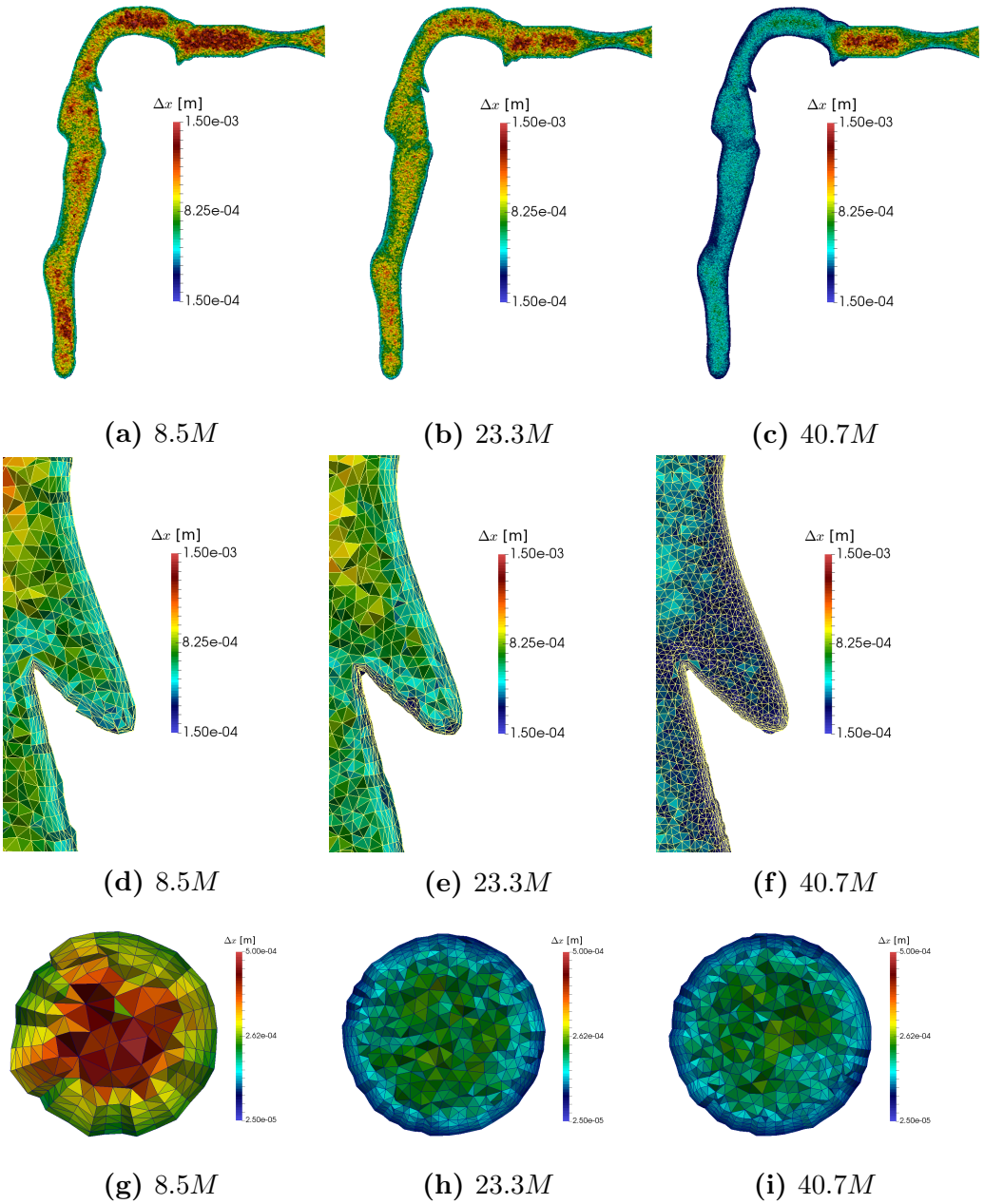

(a) 8.5M **(b)** 23.3M **(c)** 40.7M

(d) 8.5M **(e)** 23.3M **(f)** 40.7M

(g) 8.5M **(h)** 23.3M **(i)** 40.7M

Figure 6.2: Slices of the mesh along the Oral Cavity and upper Trachea, close up at boundary layer around the Epiglottis and cross section at a 7th generation Bronchi. Color plot of characteristic cell edge length Δx

6.3 Mesh Generation

The *Journal of Fluids Engineering Editorial Policy Statement on the Control of Numerical Accuracy* is used as a guideline in the refinement study [55]. Following this guideline, three meshes with increasingly finer cell resolutions were used for studying the effect of spatial resolution. The meshes consists of 8.5, 23.3, and 40.7 million (M) cells, will be referred to as 8.5M, 23.3M, and 40.7M, respectively.

Mesh characteristics including number of cells and nodes, in addition to average node spacings, h, are presented in Table 6.1.

Number of Cells	Number of Nodes	h	h_i/h_{i+1}
$8.5M$	$1.5M$	$6.54 \cdot 10^{-4}$	-
$23.3M$	$4.2M$	$4.68 \cdot 10^{-4}$	1.40
$40.7M$	$7.2M$	$3.88 \cdot 10^{-4}$	1.21

Table 6.1: Mesh characteristics including number of cells, number of nodes and characteristic edge length h. The ratio between characteristic edge length of the coarsest and finest mesh is of factor 1.72, within the range recommended by the guideline [55].

The meshes were created with *ICEM-CFD* (Ansys Inc., Canonsburg, PA, USA) from a STL surface file of the model. The VTK [58] based open source geometry processing tool *Vascular Modeling Tool Kit* (VMTK) [2] was used to scale the geometry prior meshing, as well as extracting smaller parts of the geometry for initial studies. Even though also being a meshing tool, VMTK was not able to create a boundary layer mesh, most likely due to sharp edges in the geometry (e.g Epiglottis), which is why ICEM-CDF was used.

The process of creating meshes from the surface file consisted of first assigning different areas of the geometry to *parts*. This is a feature that allows for easy adjustment of local mesh density, as well as the possibility of pinpointing locations of the mesh for assigning boundary conditions in *FEniCS*. As the variation in diameter between the inlet and the most narrow bronchi is of factor 10, the element size was set to depend on the surface curvature, controlled by a minimum and maximum factor, leading to a smooth transition in cell sizes and securing a good cross sectional resolution in the narrow branches. In order to better capture the steep gradients at the wall, a structured and exponentially growing boundary layer was configured at the walls, consisting of four cells in the normal direction. Finally, meshes was be generated using the unstructured Delauney method. In order to improve the mesh quality, the meshes were smoothed using Lagrangian smoothing.

Following the *Brno Lung* benchmark, a turbulent-like inlet condition was triggered in order to mimic the jet from a spray inhaler, typically used for delivering asthma medicine. Several methods exits for generating turbulent inflow conditions in CFD. Some include recirculating the velocity field in an extended inlet region and adding small disturbances perpendicular to the flow direction. The recirculation approach can be challenging to implement as the flow rate is not constant at all slices perpendicular to an instantaneous velocity field. In addition, artificially induced velocity perturbations may not satisfy the continuum criterion (Eq. 2.2). As no conditions on the characteristics of the turbulent inflow were given in the benchmark, a simpler approach was taken in this thesis. The inlet tube section was extended a length corresponding to five diameters, and an asymmetrical geometry was added, as depicted in Figure 6.3b. The most narrow part of the double conical

shape is half the initial radius, with an offset of 5% in the z-direction causing a turbulence triggering asymmetry.

6.3.1 Notes on the Spatial Discretization

Ideally, the boundary layers would have been set according to *The Law of the Wall*, with the thickness of innermost cells corresponding to the thickness of the *viscous sublayer* [67]. Estimating the viscous sublayer for complex geometries requires an iterative process where the wall shear is calculated to approximate a new mesh thickness and repeated until convergence. This was not performed as it would have required a varying boundary layer thickness and density throughout the geometry, which for practical reasons is very demanding to accomplish with the softwares in question.

6.3.2 Setup and Data Sampling

Based on the experimental measurements flow rates was assigned to each of the ten outlets as presented in Table 6.2. According to the directions of the benchmark the simulation should have been performed with a prescribed parabolic velocity profiles at the outlets and zero pressure at the inlet. However, this setup caused back-flow at in the inlet making the simulation to diverge. Instead, the simulations were performed with the following boundary conditions:

- Parabolic velocity profile at the inlet.
- Paraboloc velocity profiles at 9 outlets (section 13-21)
- Zero pressure condition at the last outlet (section 22)
- No slip condition at the walls.

In this thesis two different flow rates were considered; $Q = 30$ and 60 liters per second. For $Q = 60\ l/min$ the circulation time through the trachea is estimated to be $0.025\ s$, and the total computational time was set to $0.15\ s$. The total wall clock time for the computations varied from 23 to 72 hours on the Abel supercomputer depending on mesh size, number of time steps (30000 or 60000), and CPU's. The number of CPU's used for the calculations were 32, 48, and 64 for the three meshes. For the computations with flow rate $Q = 30\ l/min$ the discrete time step Δt and computational time T was doubled. The setup is shown in Table 6.3.

The full velocity and pressure field was saved every 10th time step producing 140GB, 380GB and 662GB of data for the three meshes respectively. From the saved velocity field the Kolmogorov Scales, t^+, and l^+, were computed and used to estimate to which degree the *energy cascade* was captured in the different simulations. However, as the cells in the inlet tube and outlet containers was not subject

Flow rates per segment l/min		
Segment	$Q = 30\ l/min$	$Q = 60\ l/min$
13	0.7	1.4
14	0.8	1.6
15	2.0	4.0
16	1.0	1.9
17	1.8	3.6
18	2.3	4.7
19	1.9	3.8
20	1.6	3.1
21	1.5	3.1
22	1.5	3.0

Table 6.2: Flow rates per outlet segment. Following *Brno lung* the geometry was divided into 22 segments, where 13-22 points at the outlets.

Flow rate (Q) $[\frac{l}{min}]$	Computational Time (T) [s]	$\Delta t\ [s]$
30	0.30	$1.0 \cdot 10^{-5}$ $5.0 \cdot 10^{-6}$
60	0.15	$5.0 \cdot 10^{-6}$ $2.5 \cdot 10^{-6}$

Table 6.3: Computational time and time step values for the two different flow rates.

to refinement, only data from the inner part of the geometry, depicted in Figure 6.3a, was used in the analysis.

At every time step samples of the velocity field were taken at 250 sampling probes equally spaced along three lines radial to the flow direction. The sampling was performed with *fenicstools* [43]. Both the locations, shown in 6.3b, and the names of the probe lines are following the *Brno Lungs*. From the probe samples, the mean (Eq. 2.23) and turbulence root-mean-square (rms) (eq 2.26) velocity profiles was computed. In addition, the power spectrum was computed from six different probe locations in the oral cavity and down the trachea. Following the theory of Fourier analysis every signal can be decomposed into a spectrum of frequencies which constitutes the corresponding power spectrum. However, by performing a Fourier transform of a stochastic signal the resulting power spectrum may be distorted by "noise" inherent in the signal. In Welsch method the distorting "noise" is filtered out by first splitting the signal into segments. For each segment individual power spectra are found, which are then averaged. The result is a more correct distribution, but the lower frequencies get filtered away if the signal is split into too many segments. In this study power spectra was computed by splitting the signals into 15 segments.

Mesh	Number of cores	Wall clock time per 1000 time steps
8.5M	2×16	≈ 1.1 hours
23.3M	3×16	≈ 1.2 hours
40.7M	4×16	≈ 2.3 hours

Table 6.4: Magnitude of computational time used on the Abel supercomputer for the different meshes. Note the difference in number of cores used in the simulations.

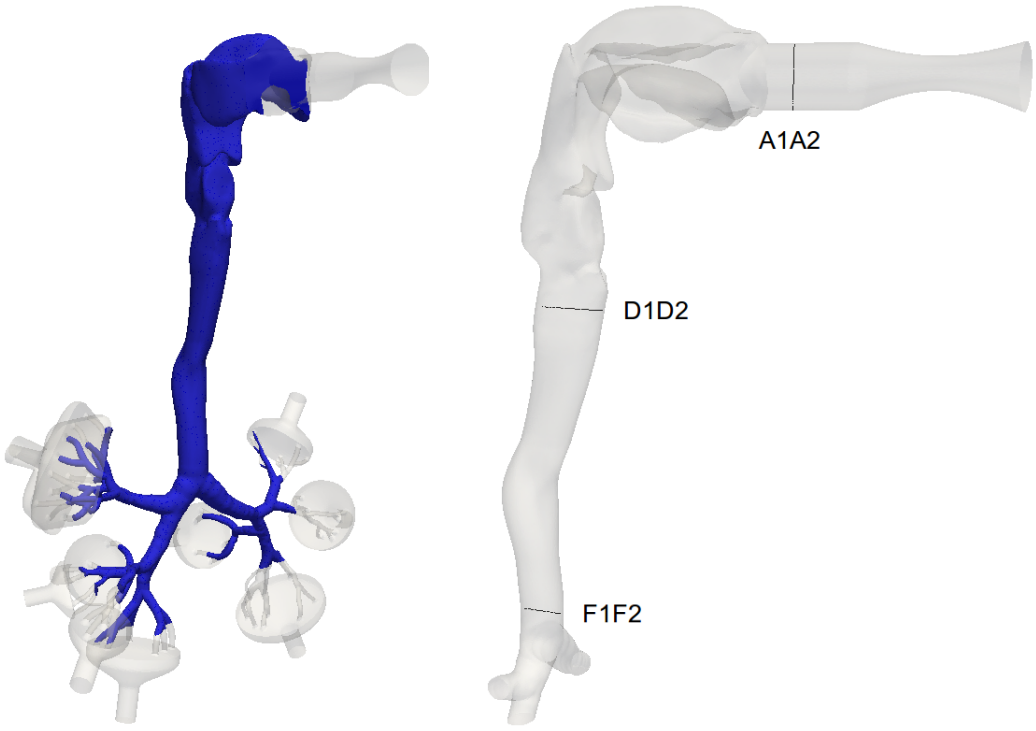

(a) Inner section **(b)** Probe locations

Figure 6.3: Figures showing the inner section representing the bodily part of the geometry, used in the turbulence analysis (left), and the locations of the three cross sectional probe lines (right).

6.4 Convergence Results

6.4.1 Flow Description

Figure 6.4 shows the instantaneous velocity profiles at a plane in center of the inlet tube and oral cavity for both flow rates and all three meshes at $t = 0.20\ s$ and $t = 0.10\ s$ for $Q = 30\ l/min$ and $Q = 60\ l/min$, respectively. The jets appear to break down at approximately the same distance from the asymmetric perturbation in the inlet tube. This is an indication of mesh convergence, as significant variations in jet break downs depending on spatial resolution has been reported in the literature

[4]. However, visual inspections of the flow field's appearance should not be given too much credence when analyzing convergence.

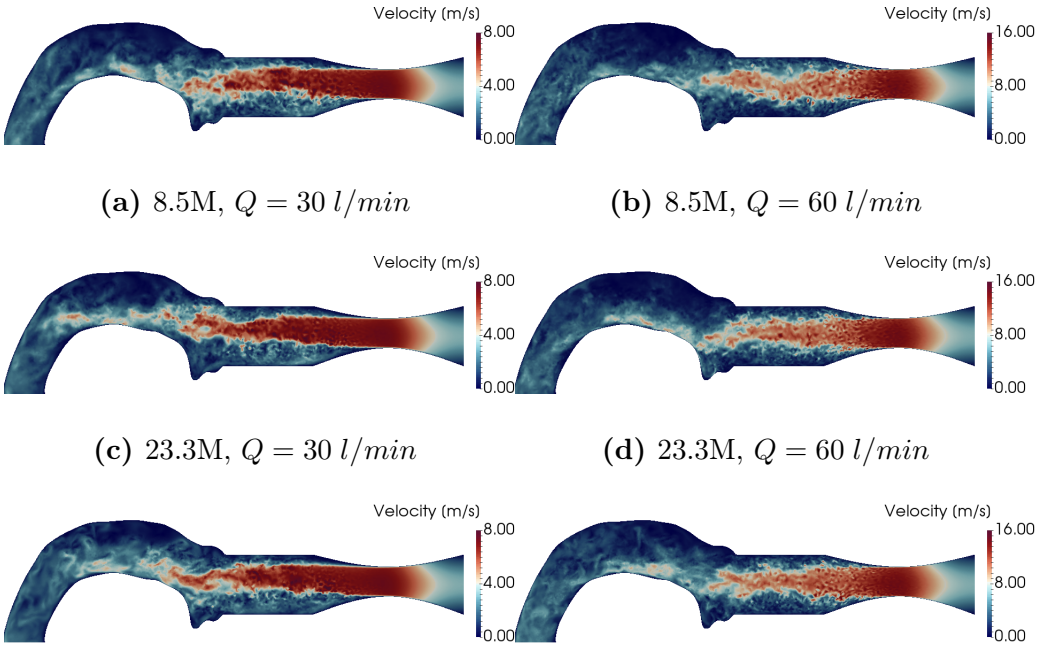

(a) 8.5M, $Q = 30\ l/min$ **(b)** 8.5M, $Q = 60\ l/min$

(c) 23.3M, $Q = 30\ l/min$ **(d)** 23.3M, $Q = 60\ l/min$

(e) 40.7M, $Q = 30\ l/min$ **(f)** 40.7M, $Q = 60\ l/min$

Figure 6.4: Figures showing the instantaneous velocity profiles at a slice through the center of the inlet tube and oral cavity. Note that the color maps are scaled differently between the two flow rates.

In 6.5 vortical structures are depicted by the Q-criterion, in additional to cross sectional slices along the trachea showing instantaneous velocity profiles at the final time steps. It can be observed that vortex structures are amplified downstream asymmetries in the geometry, and damped by dissipation in the smoother middle trachea region.

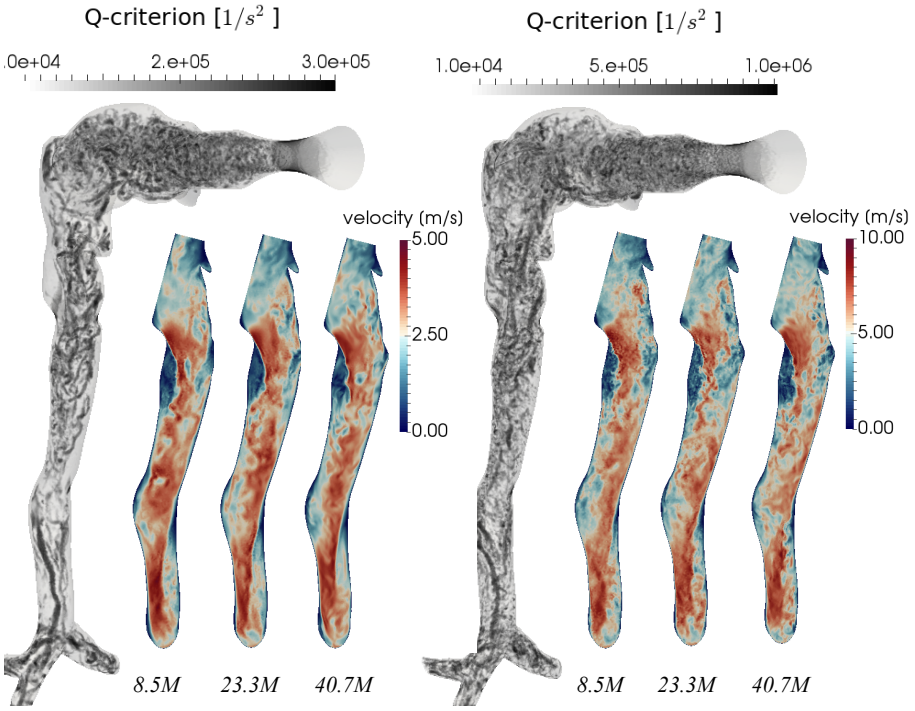

Figure 6.5: Vortical structures represented by the Q-criterion in addition slices of instantaneous velocity profiles through the trachea at $T = 0.15\ s$ and $T = 0.30\ s$ for $Q = 60\ l/min$ and $Q = 60\ l/min$, respectively

6.4.2 Mesh Refinement

The impact of increasing the mesh density was investigated both with respect to mean velocity and turbulence rms profiles. In addition, to which degree the small scale motions were captured by the spatial and temporal discretization was evaluated by considering the Kolmogorov scales in relation the time step Δt and characteristic cell size Δl.

By first investigating the impact of varying the sampling interval on mean velocity and turbulence rms profiles, the following was observed:

- The velocity fields were only "reasonably" developed after 0.2 s / 0.10 s for $Q = 30\ l/min$, $Q = 60\ l/min$, respectively.
- 10000 time steps appeared sufficient to provide a statistically significant from which turbulence statistics could be computed.
- As a result; all statistics were computed from the last 1/3 of the time steps.

Figure 6.6 shows the comparison of the mean and turbulence rms velocity profiles between the three meshes at the three locations for both flow rates. The discrepancies are greater in the more turbulent regions (A1A2 and D1D2), and are

further amplified for the highest flow rate. At location A1A2, the mean velocity peak value is significantly lower for the computations on the 8.5M mesh, while the curves are more equal at the other two locations. Despite some discrepancies, the overall results shows a clear sign of convergence for the mean value statistics, especially for $Q = 30\ l/min$.

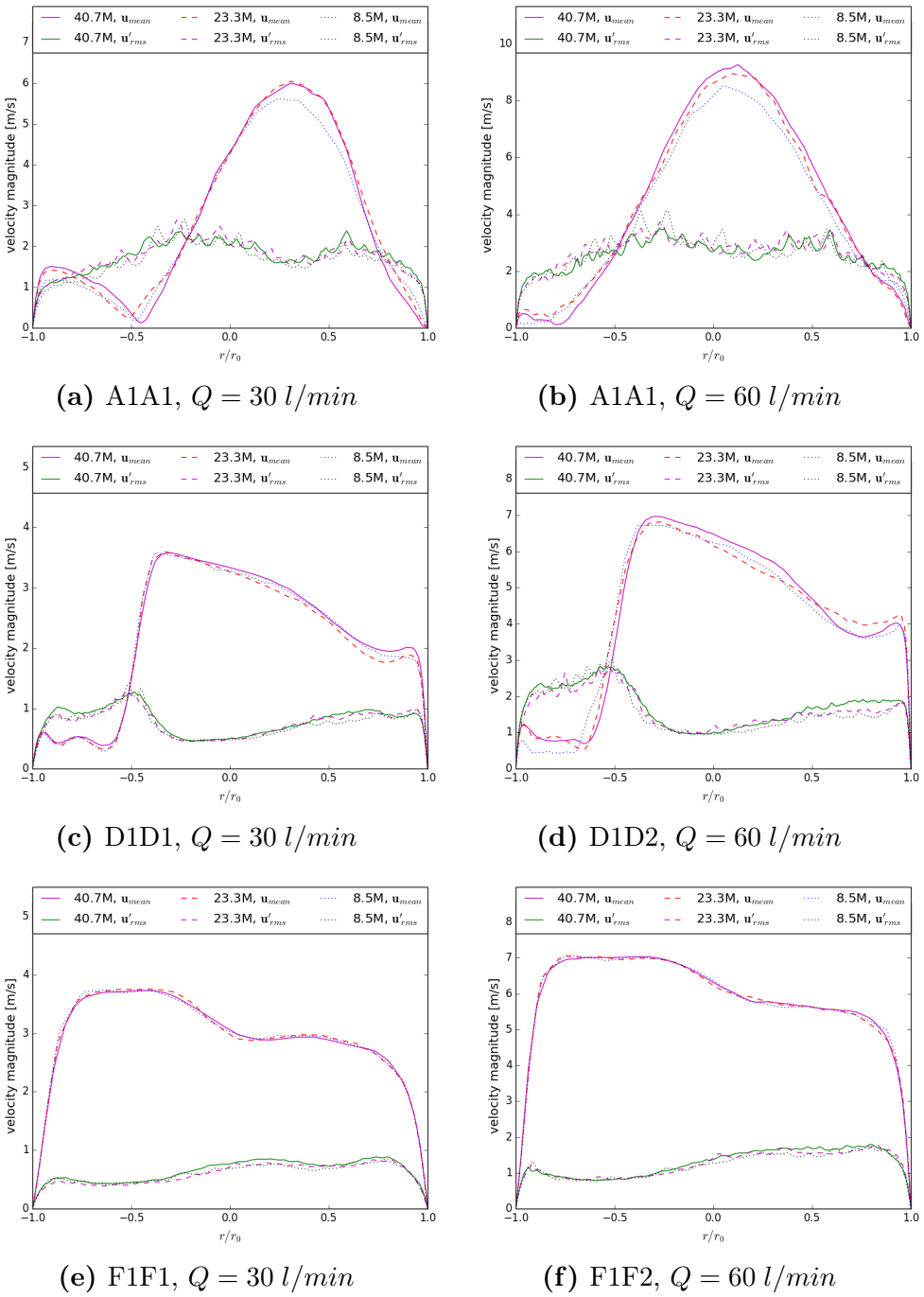

(a) A1A1, $Q = 30\ l/min$

(b) A1A1, $Q = 60\ l/min$

(c) D1D1, $Q = 30\ l/min$

(d) D1D2, $Q = 60\ l/min$

(e) F1F1, $Q = 30\ l/min$

(f) F1F2, $Q = 60\ l/min$

Figure 6.6: Mesh refinement comparison of mean velocity and turbulence rms profiles at three cross sectional lines for both flow rates

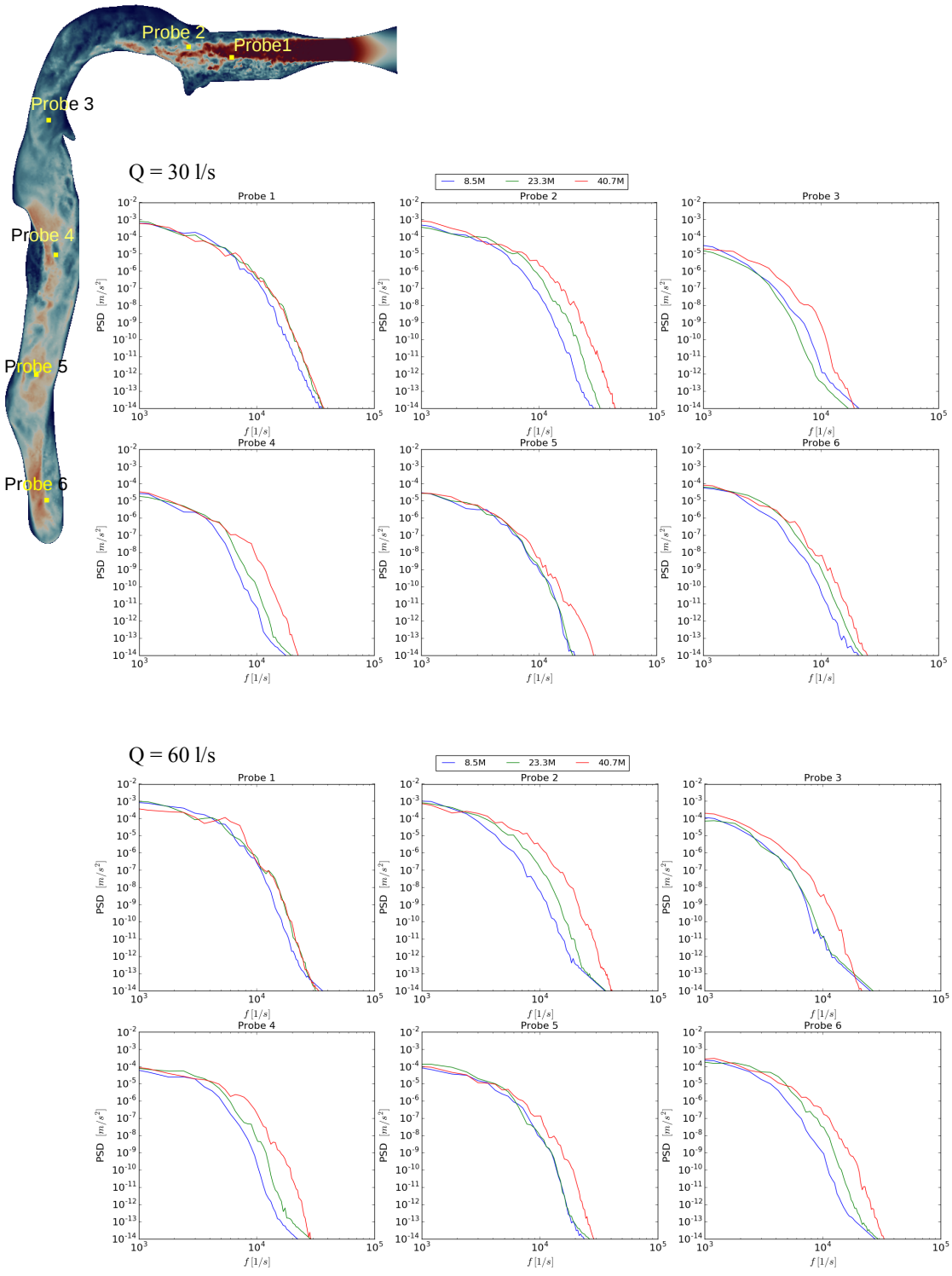

Figure 6.7: Frequency spectrum at six probe locations for both flow rates computed by Welch Method.

In Table 6.5 the minimum and mean turbulence length scales are compared with the node spacings in the different meshes. The Kolmogorov Scales are functions of the rate of dissipation, ϵ and kinematic viscosity, ν and thus sensitive to mesh refinement, which is evident when considering the $\eta_m in$ values. For $Q = 30; l/min$ the smallest Kolmogorov length scale is varying from 11.9 μm to 10.6 μm, and 7.0 μm and 6.0 μm for $Q = 60; l/min$. The change in η between the two flow rates is in agreement with Eq. 2.19 ($\approx$ 59% smaller η for double Re). When observing minimum values of the ratios between Δl and η, it is obvious that even the simulations on the 40.3M mesh is far away from being a DNS. Even the average turbulence length scales are for both flow rates significantly smaller than the node spacing at the corresponding locations. The same trend is seen for t^+. However, the decrease of this quantity shows that the finer meshes are able to resolve more of the smallest length scales, thus also represent more of the dissipation range. Consequently, more energy can be carried by the smallest length scales in the simulations on the finer meshes, which is verified by observing the energy spectrum curves depicted in Figure 6.7. At all six locations, for both flow rates, more energy is distributed in the higher frequencies. At probe 3 for $Q = 30\ l/min$ as well as 2 and 3 for $Q = 60\ l/min$ it can be seen that the 8.5M and 23.3M curves are leveling out at and becoming much smoother the highest frequencies. This is an artificial effect and an indication that the smallest time scales are limited by low mesh resolution, i.e, that the small length scales with corresponding time scales cannot be approximated by the meshes.

	$Q = 30\ l/min \quad \Delta t = 1 \cdot 10^{-5}\ s$			$Q = 60\ l/min \quad \Delta t = 5 \cdot 10^{-6}\ s$		
	$8.5M$	$23.3M$	$40.7M$	$8.5M$	$23.3M$	$40.7M$
Δl_{avg}	$4.22 \cdot 10^{-4}$	$2.27 \cdot 10^{-4}$	$1.85 \cdot 10^{-4}$	$4.22 \cdot 10^{-4}$	$2.27 \cdot 10^{-4}$	$1.85 \cdot 10^{-4}$
η_{min}	$1.19 \cdot 10^{-5}$	$1.13 \cdot 10^{-5}$	$1.06 \cdot 10^{-5}$	$7.03 \cdot 10^{-6}$	$7.00 \cdot 10^{-6}$	$5.98 \cdot 10^{-6}$
η_{mean}	$1.01 \cdot 10^{-4}$	$9.60 \cdot 10^{-5}$	$1.09 \cdot 10^{-4}$	$6.31 \cdot 10^{-5}$	$6.02 \cdot 10^{-5}$	$6.90 \cdot 10^{-5}$
$(\frac{\Delta l}{\eta})_{max}$	22.94	19.31	15.93	35.93	31.33	23.94
$(\frac{\Delta l}{\eta})_{mean}$	5.15	3.34	2.94	8.11	5.26	4.61
l^+_{max}	19.31	16.35	13.41	30.27	26.53	20.17
l^+_{mean}	4.47	2.90	2.57	7.08	4.59	4.06

Table 6.5: Turbulence length scales compared with mesh resolutions for the spatial refinement study. Metrics computed from average of 1000 time steps in the time interval T=$[0.2 - 0.3\ s]$ for $Q = 30\ l/min$ and $T = [0.1 - 0.15\ s]$ for $Q = 60\ l/min$.

Table 6.6 shows the sensitivity of the turbulence time scale to spatial resolution. The smallest Kolmogorov time scales approximated are decreasing for increased mesh resolution. The variations are of factor 1.82 and 1.76 for $Q = 30\ l/min$ and $Q = 60\ l/min$, which indicates that steeper velocity gradients are captured for finer mesh resolution. That the Kolmogorov time scales appear to be more sensitive to mesh resolution can be explained by recalling their definitions 2.18 and observing that τ_η and η scales with ∇u and $(\nabla u)^{1/2}$, respectively.

	$Q = 30\ l/min \quad \Delta t = 1 \cdot 10^{-5}\ s$			$Q = 60\ l/min \quad \Delta t = 5 \cdot 10^{-6}\ s$		
	$8.5M$	$23.3M$	$40.7M$	$8.5M$	$23.3M$	$40.7M$
CFL_{max}	0.59	1.11	1.16	0.53	1.06	1.30
$\tau_{\eta,min}$	$6.54 \cdot 10^{-6}$	$4.79 \cdot 10^{-6}$	$3.56 \cdot 10^{-6}$	$2.84 \cdot 10^{-6}$	$2.06 \cdot 10^{-6}$	$1.61 \cdot 10^{-6}$
$\tau_{\eta,mean}$	$2.24 \cdot 10^{-3}$	$1.39 \cdot 10^{-3}$	$2.25 \cdot 10^{-3}$	$7.41 \cdot 10^{-4}$	$4.83 \cdot 10^{-4}$	$8.05 \cdot 10^{-4}$
t^+_{max}	1.10	1.58	2.04	1.30	1.75	2.27
t^+_{mean}	0.021	0.026	0.020	0.026	0.031	0.025

Table 6.6: Turbulence time scales compared with mesh resolutions for the *spatial refinement study*. Metrics computed from average of 1000 time steps in the time interval T=$[0.2 - 0.3\ s]$ for $Q = 30\ l/min$ and $T = [0.1 - 0.15\ s]$ for $Q = 60\ l/min$.

The overall trend for both flow rates show that the smallest turbulence time scale is approximately a factor 2.5 less than the temporal resolutions considered in spatial refinement simulations, which suggests that a temporal refinement may yield some improvement. However, as the average turbulence time scales are more than a factor 100 greater than Δt, and that it appears some of the smallest time scales are cut of by coarse mesh resolution, only limited effects of decreasing Δt was expected.

6.4.3 Temporal Refinement

	$Q = 30\ l/min \quad$ 24M		$Q = 60\ l/min \quad$ 24M	
	$\Delta t = 1.0 \cdot 10^{-5}\ s$	$\Delta t = 5.0 \cdot 10^{-6}\ s$	$\Delta t = 5.0 \cdot 10^{-6}\ s$	$\Delta t = 2.5 \cdot 10^{-6}\ s$
CFL_{max}	1.11	0.56	1.06	0.53
$\tau_{\eta,min}$	$4.79 \cdot 10^{-6}$	$4.75 \cdot 10^{-6}$	$2.06 \cdot 10^{-6}$	$2.05 \cdot 10^{-6}$
$\tau_{\eta,mean}$	$1.39 \cdot 10^{-3}$	$1.14 \cdot 10^{-3}$	$4.83 \cdot 10^{-4}$	$4.90 \cdot 10^{-6}$
t^+_{max}	1.58	0.76	1.75	0.48
t^+_{mean}	0.026	0.013	0.031	0.016

Table 6.7: Turbulence time scales compared with mesh resolutions for the *temporal refinement study*. Metrics computed from average of 1000 time steps in the time interval T=$[0.2 - 0.3\ s]$ for $Q = 30\ l/min$ and $T = [0.1 - 0.15\ s]$ for $Q = 60\ l/min$.

The impact of temporal resolution was investigated using the 23.3M mesh. Due to limited computational resources and time limits on Abel, it was only practically achievable to reduce Δt once with a factor 2. A coarser temporal resolution was not tested as it was out of question to the limiting, numerical stability of the equation of particle motion algorithm.

, simulations with increased Δt was not performed.

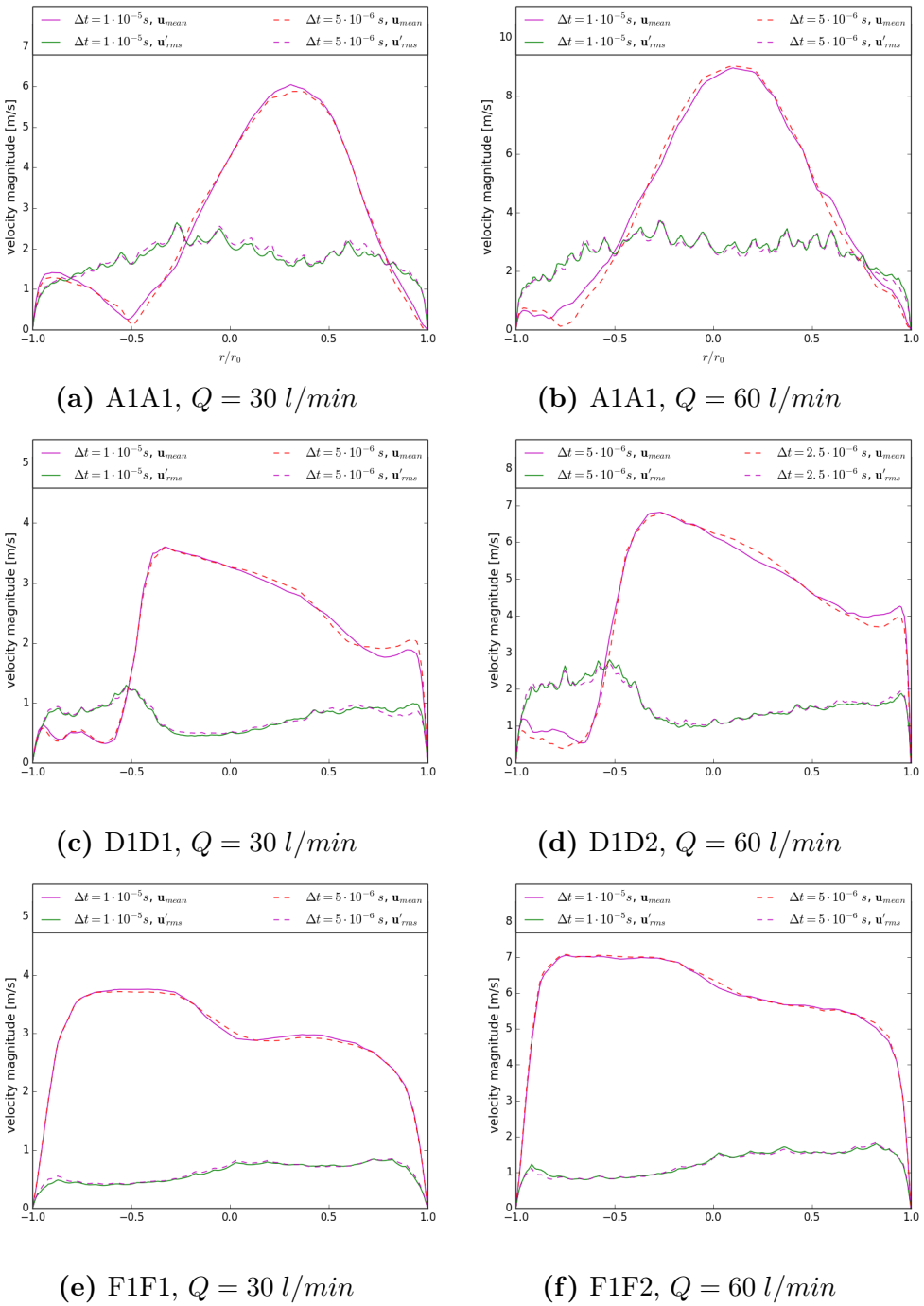

(a) A1A1, $Q = 30\ l/min$ **(b)** A1A1, $Q = 60\ l/min$

(c) D1D1, $Q = 30\ l/min$ **(d)** D1D2, $Q = 60\ l/min$

(e) F1F1, $Q = 30\ l/min$ **(f)** F1F2, $Q = 60\ l/min$

Figure 6.8: Cross sectional mean velocity turbulence rms profiles for 23M, $Q = 60\ l/min$ computed over 10000 time steps for three different starting time steps.

Figure 6.8 shows the mean velocity and turbulence rms curves following computations with the different temporal resolutions. Some differences between the curves are seen, especially in segments with high turbulence rms values. As observed in Figure 6.6 the discrepancies are amplified for $Q = 60\ l/min$. The overall effects

of doubling the temporal resolution with regards to mean value statistics are not radical, especially not for $Q = 30\ l/min$. Whereas increasing the mesh resolution had a significant effect on the turbulence rms velocity curve at $A1A2$, the temporal resolution had a much less impact. Furthermore, when observing Table 6.7 it is evident that the computed Kolmogorov time scales are only marginally affected by the change of Δt. Despite the simulations are close to being "well resolved in time" ($\Delta t < \tau_{eta}$) when the temporal resolution is halved, the impact on the large scale flow appears to be rather limited.

6.4.4 Discussion

As addressed in Subsection 6.4.2, based on samplings throughout the simulations, it could not be concluded that the flow fields had reached a state of being totally developed (e.g not affected by initial effects). Ideally, as explained in Section 2.4.1, flow field statistics should be computed based on a statistically significant interval sampled after the flow field has reached a developed state. However, as only very small variations in the velocity profiles were seen between different sampling intervals (e.g $0.15 - 0.25$ and $0.20 - 0.30\ s$), it assumed that extending the simulations would not have altered the outcome of the below conclusion.

6.5 Conclusion: A Trade-off between Accuracy and Computational Cost

$\rho_p = 914\ kg/m^3 \quad \mu = 1.95\ kg/sm$	
$d_p\ [\mu m]$	$\tau_p\ [s]$
1.0	$2.60 \cdot 10^{-6}$
2.5	$1.63 \cdot 10^{-5}$
4.0	$4.17 \cdot 10^{-5}$
10.0	$2.60 \cdot 10^{-4}$
20.0	$1.04 \cdot 10^{-3}$

Table 6.8: Response times for different diameters and given particle density and viscosity.

When also considering computational resources it is concluded the 23.3M mesh produces a velocity field that is adequately well resolved in time and space for $\Delta t = 1 \cdot 10^{-5} s$ and $Q = 30\ l/min$. For the larger flow rates a lesser degree of convergence was observed. Thus this flow rate was not considered for particle tracking, as it was deemed that the resulting uncertainties in deposition fractions would have been to large.

Furthermore, performing the concluding particle tracking simulations with $\Delta t = 1 \cdot 10^{-5} s$ implies that the smallest particles considered, $d_p = 1\ \mu m$, are outside the stability criterion (cf., 4.20), leading to less accurate results.

Chapter 7

A Simulation of the Motion of Inhaled Particles in the Human Respiratory System

7.1 Introduction

In Chapter 6 it was found that for the flow rate $Q = 30\ l/min$, the 23.3M mesh in combination with a temporal resolution of $\Delta t = 1 \cdot 10^{-5}\ s$ produced a flow field reasonably temporally and spatially resolved, at a moderate computational cost. It was also found that after a simulation over 30000 time steps, corresponding to $0.3\ s$, the flow field had become sufficiently developed in time. Hence, this setup was chosen as a basis for completing the main goal for this thesis - simulating the flow and motion of inhaled particles in the human respiratory system, after the directions in the benchmark test case, *Brno Lungs*

7.2 Benchmark test case: *Brno Lung*

Following *Brno Lungs*, the participating researchers was given access to a digitalized model of the lung cast in a *.vtp* file format, which can be read by several meshing tools. As briefly outlined in Section 6.3.2, flow rates, boundary conditions, and properties of the dispersed phase was given in the benchmark as the following:

- Flow rates: $Q = 15,\ 30,$ and $60\ l/min$.
- Prescribed velocity conditions at the ten outlets.
- Zero pressure condition at the inlet.
- No slip condition ($\mathbf{u}_{wall} = 0$) at the remaining boundary.

- Fluid kinematic viscosity $\mu = 1.7 \cdot 10^{-5}\ m^2/s$ (air at $\approx 25°C$)
- Particle diameters, $d_p = [0.5,\ 1,\ 2,\ 2.5,\ 4,\ 4.3,\ 6,\ 8,\ 10,\ 20]\ \mu m$ and density $\rho_p = 914\ kg/m^3$.
- 10^5 particles of each size released from random locations at the inlet surface over $0.025\ s$, $(Q = 60\ l/min)$

The model was divided into 22 segments as depicted in Figure 7.1. The deposition pattern was determined by counting the number of deposited particles in each segment.

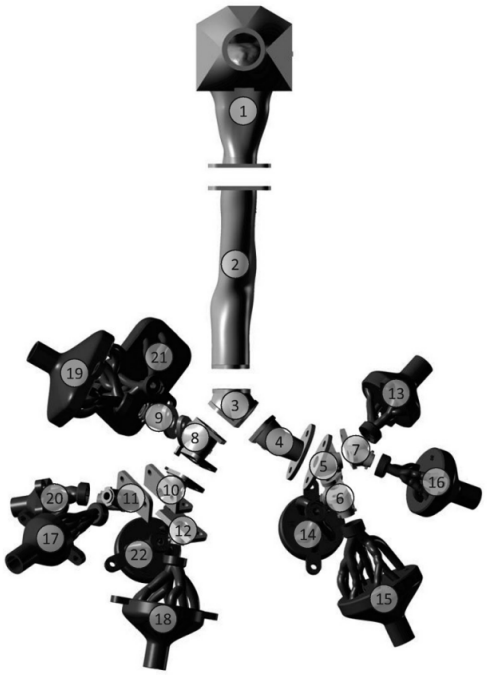

Figure 7.1: The human airways model split into 21 segments following the *Brno Lung* benchmark

7.3 Setup and Modifications of the Benchmark

Some modifications to the benchmark directions were done in this thesis due to problems imposing the assigned boundary conditions and limited computational resources practically available. As explained in Section 6.3.2, the boundary conditions were changed to prescribed parabolic velocity profile at the inlet and nine of the outlets, and zero pressure at the last outlet. In addition, the flow rate $Q = 60\ l/min$ was discarded, and only simulations with $Q = 30\ l/min$ was found adequate for performing the numerical experiment. Furthermore, the total number

of injected particles of each size were reduced to 25000, and only the five following diameters were considered: [1, 2.5, 4, 10, 20] μm.

The following statistics and definitions are computed and discussed in this chapter:

- The *segments* (cf. Figure 7.1) are merged into four *sections*:
  1. Oral cavity: seg. 1.
  2. Trachea: seg. 1-2.
  3. 2nd - 4th generation bronchi: seg. 4-12.
  4. 5th-7th generation bronchi: seg. 13-22.
- Particles beyond the 7th generation bronchi (i.e in the outlet containers) are considered not deposited.
- Deposition *fraction*: the fraction of particles deposited in a given *segment* or *section*, normalized both to the number of released or deposited particles .
- Deposition *efficiency*: the fraction of particles deposited within the geometry (not including outlet containers), normalized both to the number of released or deposited particles .

7.4 Deposition Results

Figure 7.2 and 7.3 show the location of the particles deposited within the model. Larger particles yields a higher deposition efficiency as depicted in Figure 7.5. For the small particles ($d_p \leq 4.0\mu m$) the deposition efficiency is so low that any conclusion based on the local deposition statistic is dubious. It appears that the small particles are less affected by inertia as no significant deposition build-ups are seen are any bifurcation. This is not surprising when recalling the results in Section 5.3 where a shift in the deposition mechanism was observed between small and large particles. Furthermore, as a result of less inertia and thus shorter response times, the small particles appears to be more influenced by convection due to turbulent-like motion (i.e being transported by eddies). By inspecting the particles deposited in the oral cavity, it can be seen that very few of the small particles deposit on the tung, while some have deposited at the inlet walls. It can even be seen that a significant amount of particles of all sizes have deposited behind the inlet release plane, which can be explained by considering Figure 7.4. As the inlet perturbation has an offset in the z-direction, a recirculation zone if created underneath the jet, dragging the particles backwards. Even at the end of the simulation a small number of particles of all size were still trapped in the recirculating back-flow.

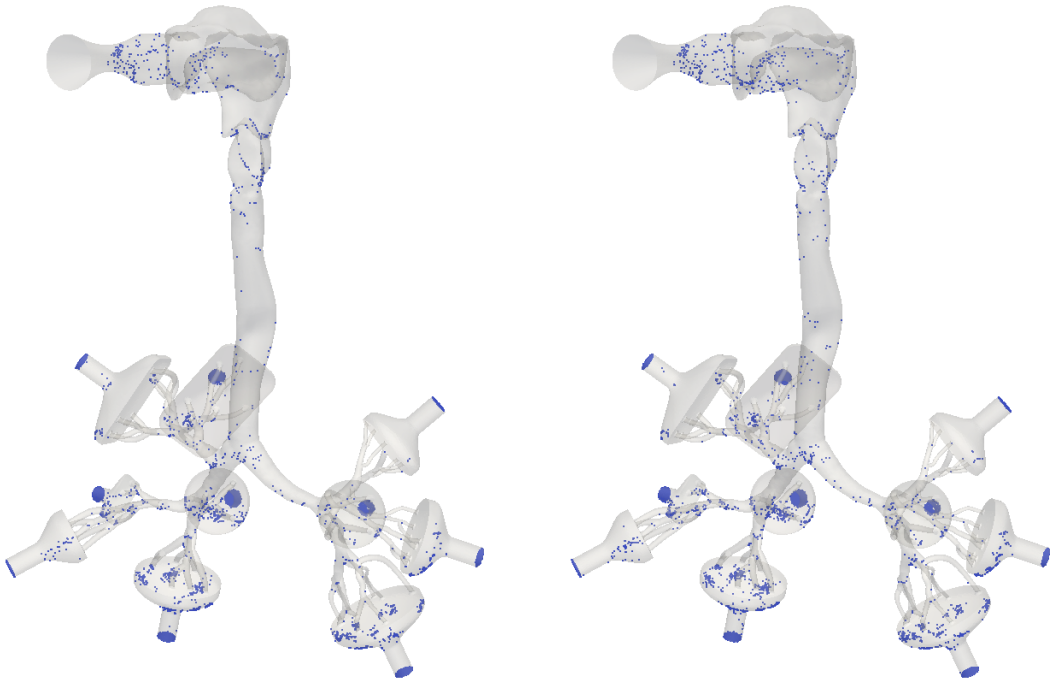

(a) $d_p = 1.0\ \mu m$ **(b)** $d_p = 2.5\ \mu m$

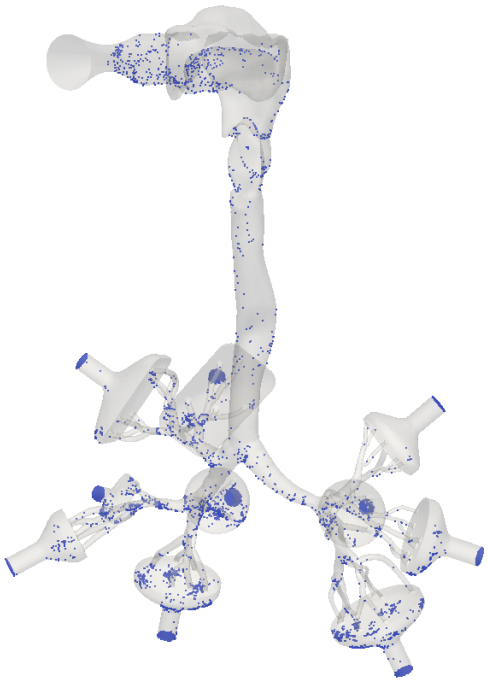

(c) $d_p = 4.0\ \mu m$

Figure 7.2: Deposition pattern for small particles after 0.5 s of inhalation at a constant flow rate $Q = 30\ l/min$.

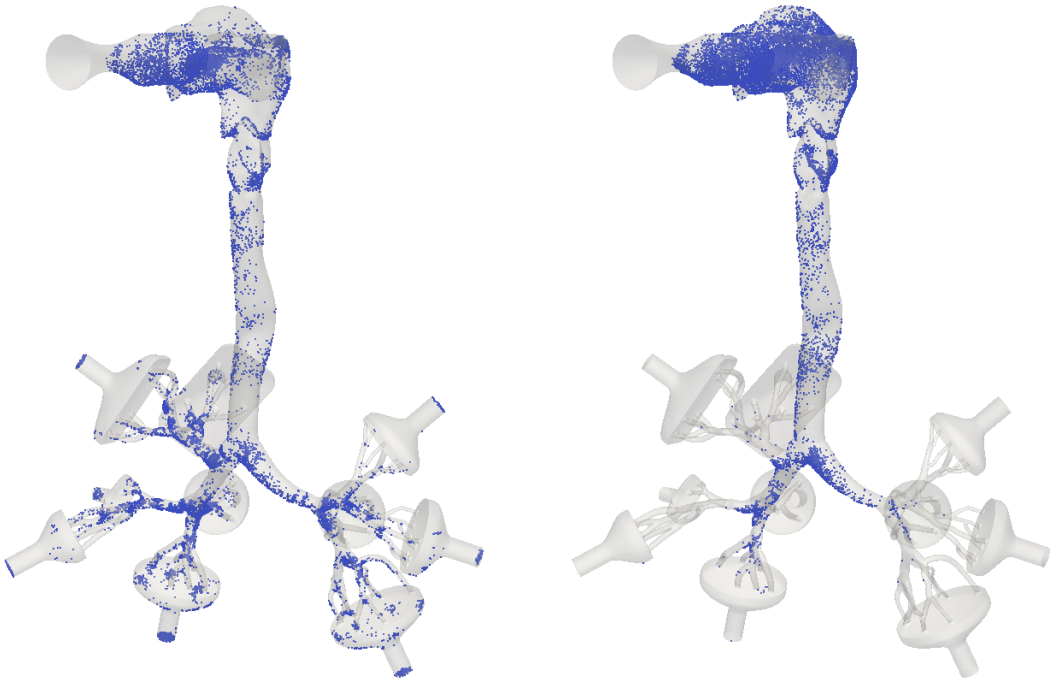

(a) $d_p = 10.0\ \mu m$ **(b)** $d_p = 20.0\ \mu m$

Figure 7.3: Deposition pattern for the small particles after 0.5 s of inhalation at a constant flow rate of $Q = 30\ l/min$

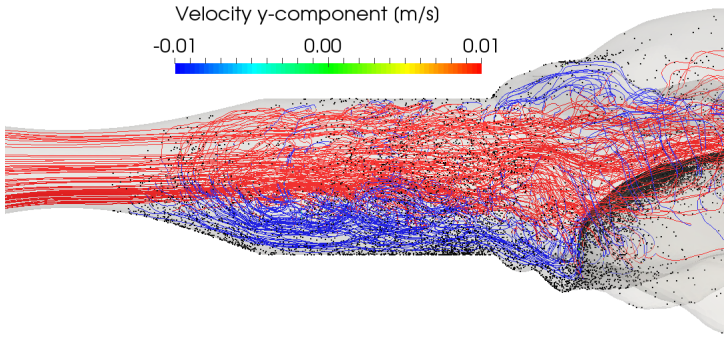

Figure 7.4: Streamlines in the inlet region showing particles being deposited upstream the release plane due to backflow. Color of streamlines indicating magnitude of velocity y-component. The deposited particles (black dots) have a diameter of 20 μm.

When considering Figure 7.3a it can be seen that a significant fraction of the inhaled particles have deposited on the tip of the tung. The same also applies for the largest particles, although not equally apparent in Figure 7.3b due to

dense deposition in the entire oral cavity. Furthermore, virtually none of the small particles have deposited in the bend where the oral cavity connects with the throat, which demonstrates the shift in the primary deposition mechanism from turbulence convection to particle inertia between the small and large particles.

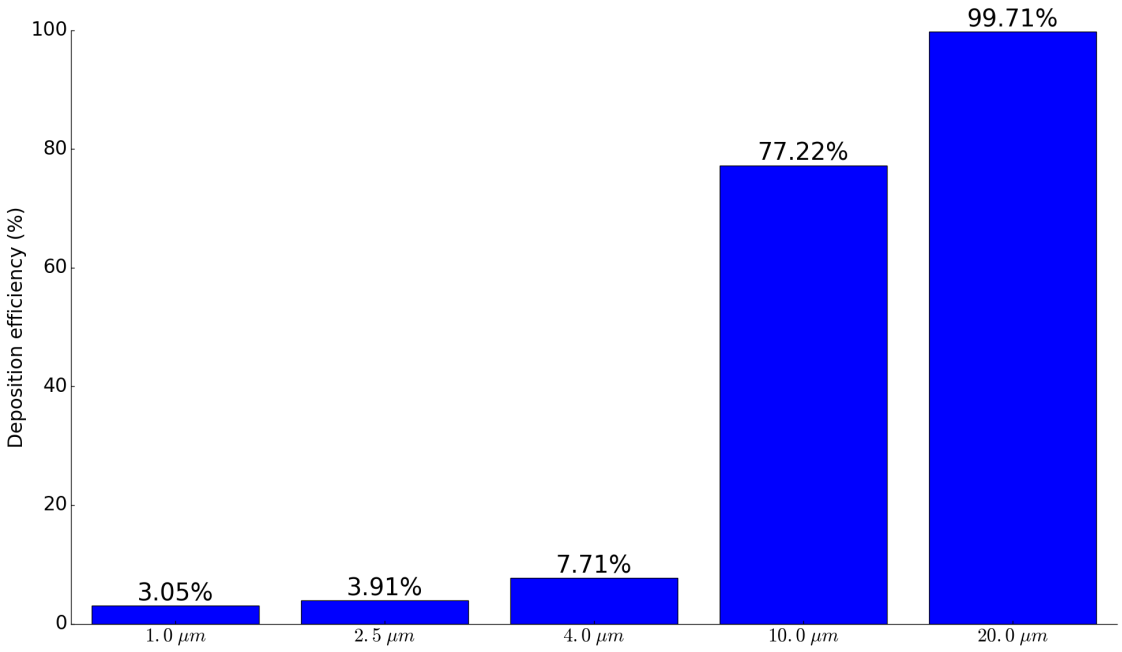

Figure 7.5: Deposition efficiency ($N_{\text{deposited}}/N_{\text{released}}$) per particle diameter.

The Figures 7.6 and 7.7 shows comparisons of the deposition fraction per *section* for the different particles, normalized against the number of released and deposited particles, respectively. Figure 7.6 shows that the large particles $d_p \geq 10.0\mu m$ have a deposition fraction of a magnitude 10 larger than the small particles in the oral cavity. Virtually none of the largest particles have penetrated to the 5th-7th generation bronchi, whereas a significant portion of the second largest particles have deposited in the section. In the two *sections* constituting the bronchi, the $10\mu m$ particles are, by far, dominating the deposition fraction.

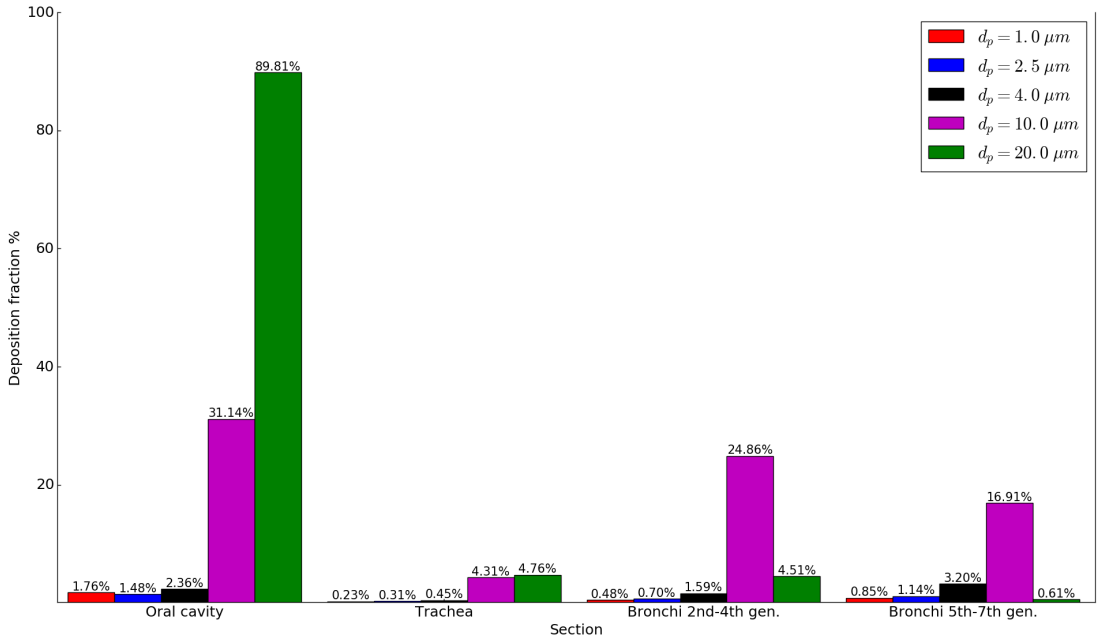

Figure 7.6: Comparison of deposition fraction per segment normalized against total number of particles injected (25000).

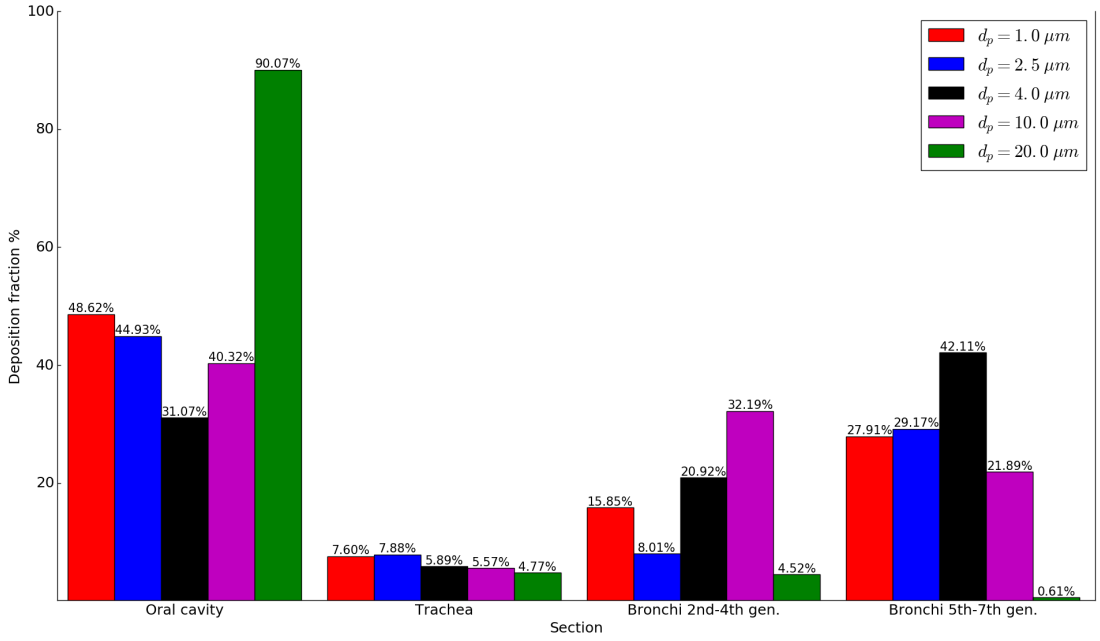

Figure 7.7: Comparison of deposition fraction per segment normalized against total number of particles deposited (ref. Table 7.5)

If considering the distribution of deposited particles (Figure 7.7) it can be observed that for $d_p \leq 4.0\ \mu m$ the fraction of particles depositing in the oral cavity is decreasing for increased diameter, while the opposite applies for $d_p > 4.0\ \mu m$. For all particles, except $d_p = 4.0\ \mu m$, the oral cavity is the *section* with the highest portion of deposited particles. However, as suggested above, the primary mechanism for deposition in this *section* appears to be turbulence-like convection and particle inertia for the small and large particles, respectively. Compared with the other *sections*, the Trachea is the *section* with the overall lowest deposition fraction, again with the exception for the largest particles. The smallest particles prevail the deposition fraction in this section, which strengthens the perception of turbulence-like convection being the driving mechanism for deposition of the small particles.

The Figure 7.9 - 7.13 show the deposition fraction per segment *section* for each of the particles, depicting a more detailed map of the deposition distribution. For the small particles the deposition fraction in each segment, except the first (oral cavity), is so small that the statistical significance is dubious. *Segment* 13 and 14 stands out with containing a very low fraction of the deposited particles. Of the largest particles none deposited neither in these *segments* or segment 17, 20, and 22. The segments with few or none particles deposited have correspondingly low flow rates (ref. Table 6.2).

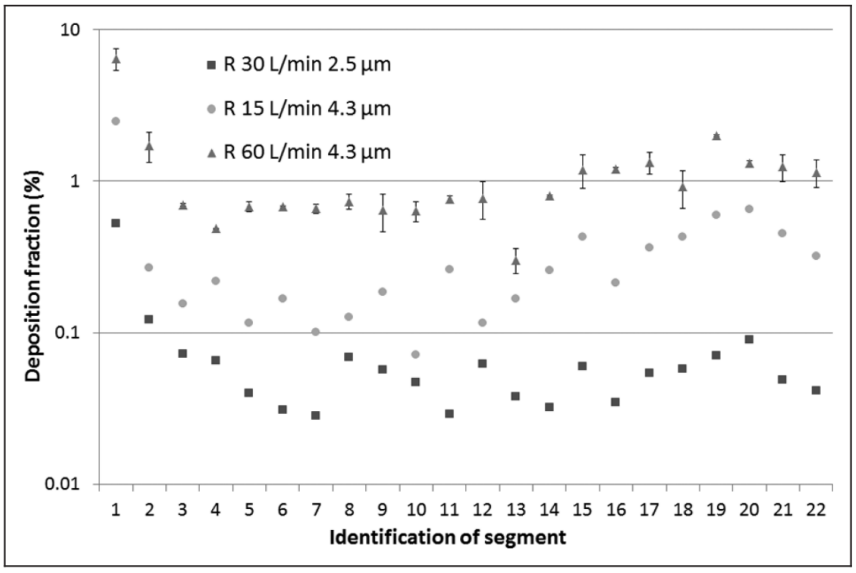

Figure 7.8: Deposition fractions per section obtained in the in vitro Brno experiment. The experiment was conducted with a steady, unperturbed inlet flow.

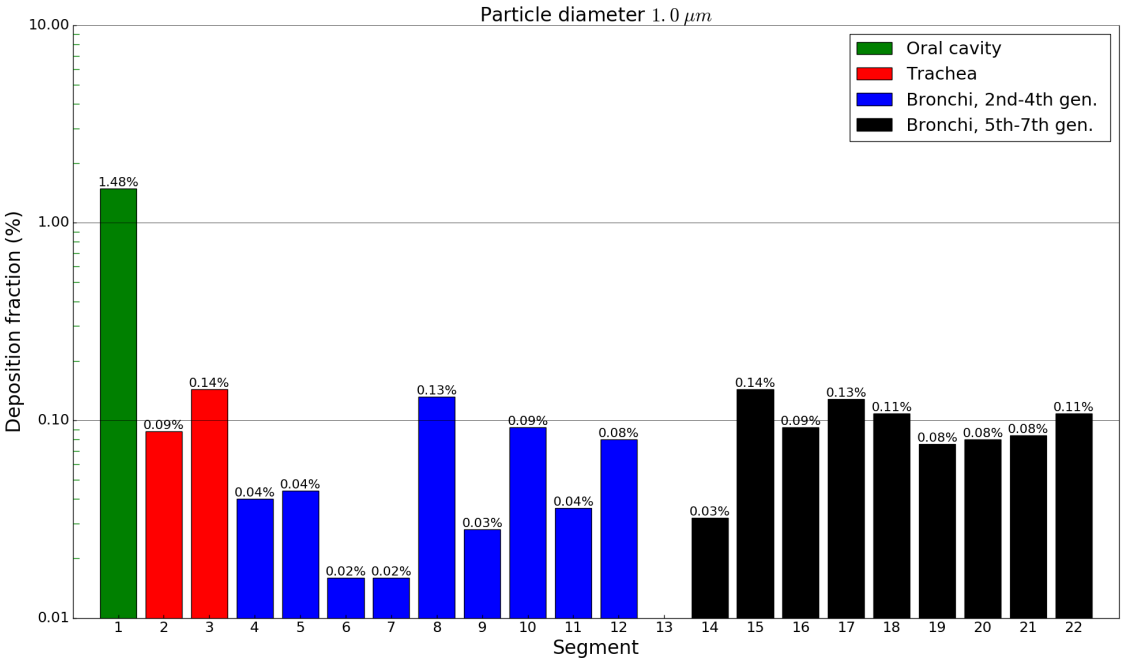

Figure 7.9: Deposition fraction per section for $d_p = 1.0\ \mu m$

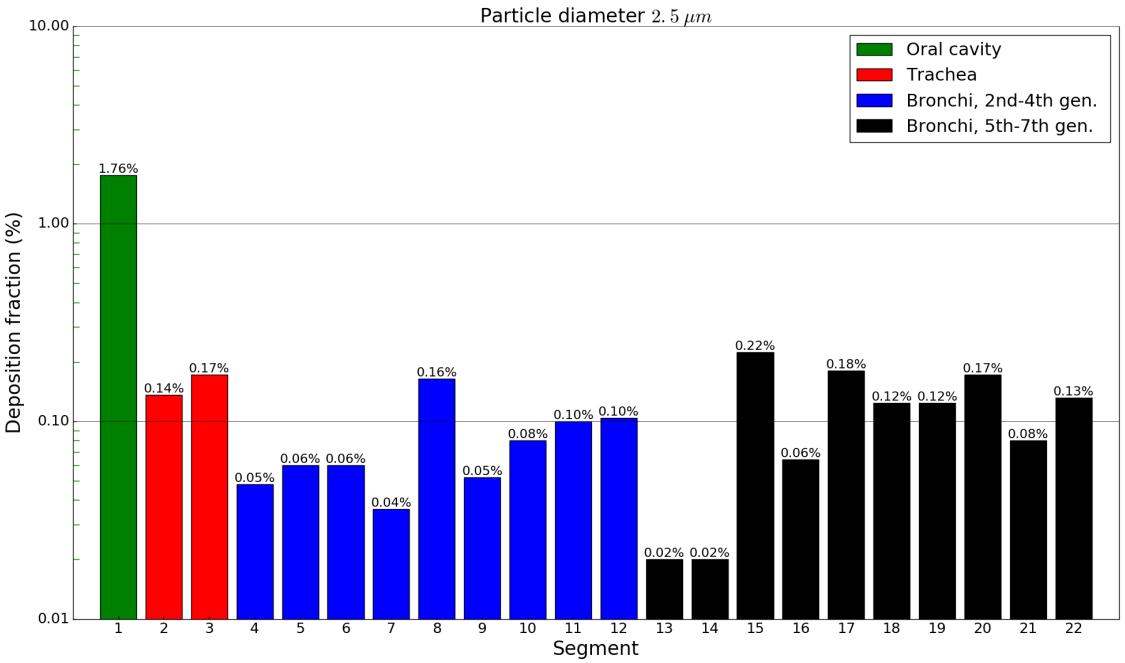

Figure 7.10: Deposition fraction per section for $d_p = 2.5\ \mu m$

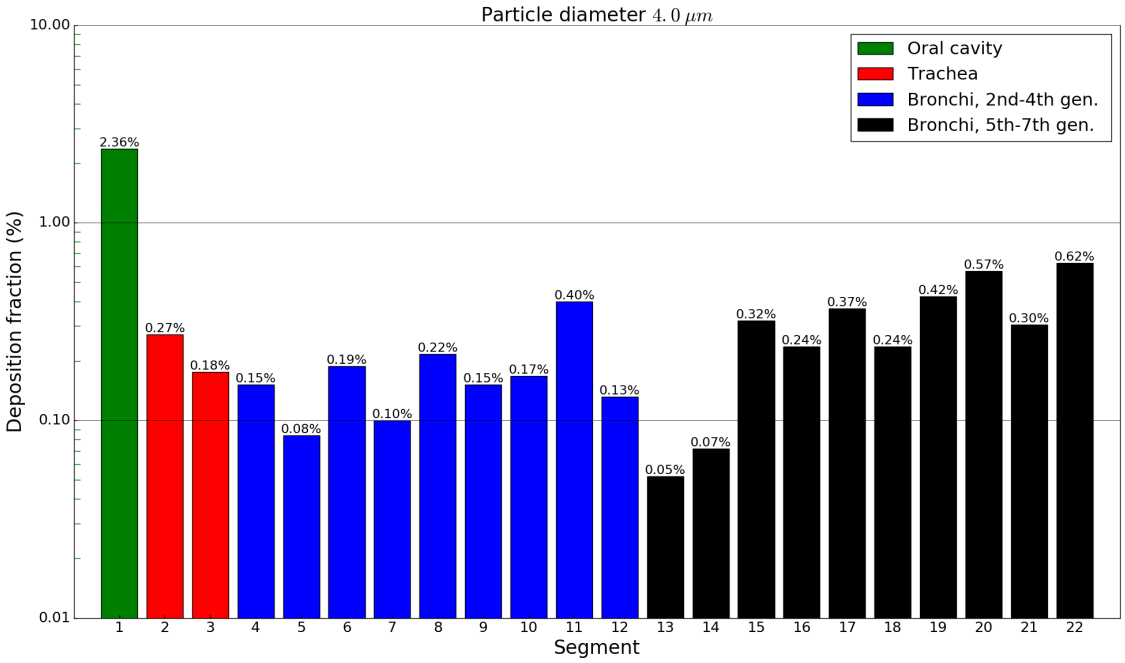

Figure 7.11: Deposition fraction per section for $d_p = 4.0\ \mu m$

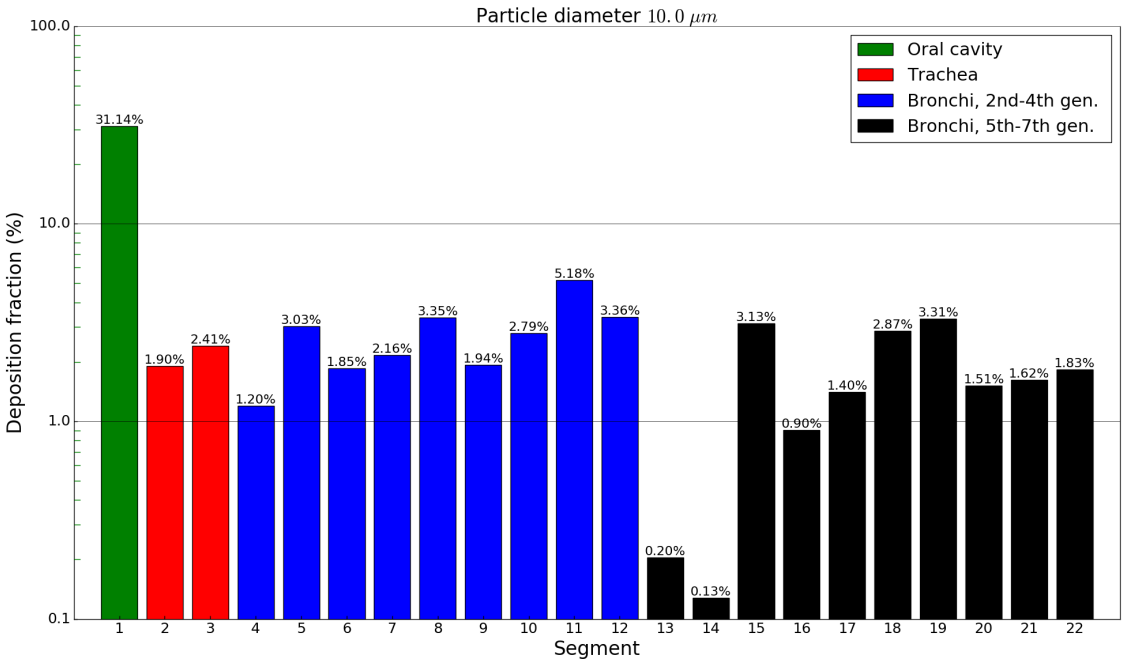

Figure 7.12: Deposition fraction per section for $d_p = 10.0\ \mu m$

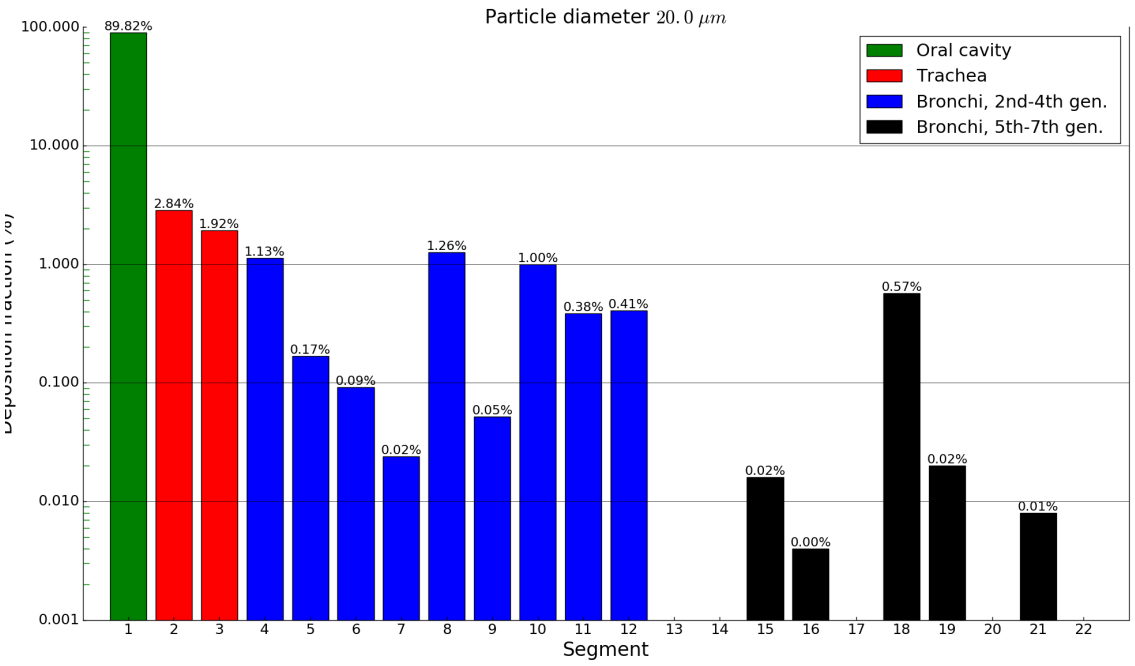

Figure 7.13: Deposition fraction per section for $d_p = 20.0\ \mu m$

In Figure 7.14 the deposition fractions per segment are compared between the different particles. Figure 7.15 shows the same, but with the metrics normalized against the number of particle deposited. By considering the deposition-normalized statistics, some correlation between the deposition patterns are seen. However, as Figure 7.7 is logarithmically scaled, caution must be taken when comparing the curves. For all particles, *segment* 1 is dominating the deposition fraction statistics. The 20 μm particles show the largest shows the most significant deviation from the deposition trend overall, with the curve being discontinuous due to several segments without any deposition (cf., Figure 7.13). Noteworthy are the quite well correlated deposition fractions in segment 2, 15, 17, and 18.

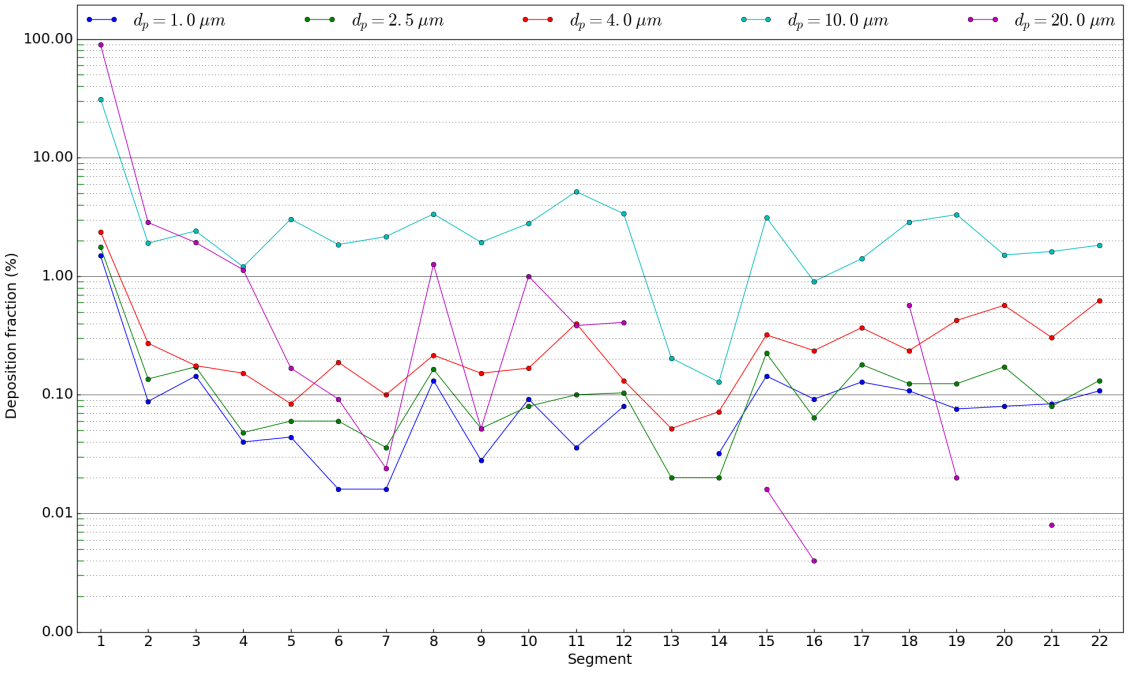

Figure 7.14: Comparison of deposition fraction per segment normalized against the number of particles injected (25000).

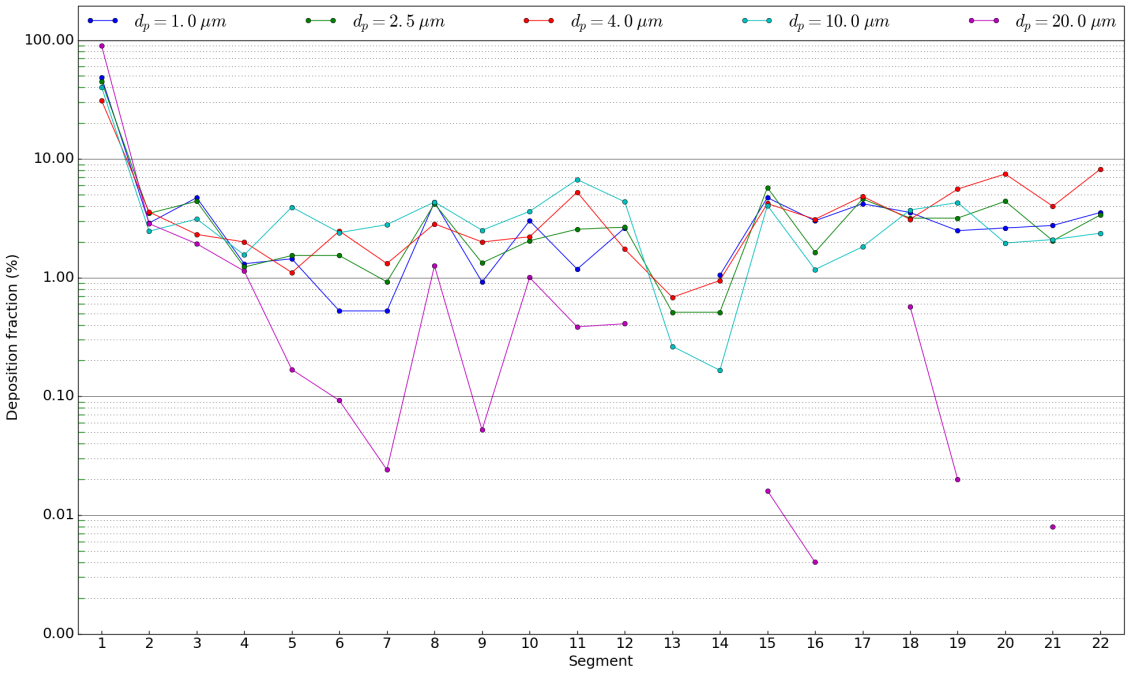

Figure 7.15: Comparison of deposition fraction per segment normalized against the number of particles deposited (ref. Table 7.5)

7.5 Discussion and Relations to the Literature

Results from the in vitro experiment which sets the basis for the *Brno lung* benchmark is depicted in Figure 7.8. Note that squares denotes 2.5 μm particles at $Q = 30\ l/min$. The experiment was performed on the physical version of the model used in this thesis, but without a turbulent inlet profile. Given the deviation in inlet flow condition, the deposition pattern numerically computed in this thesis does not deviate radically for the one experimentally obtained. The overall increase of deposition fraction in many of the *segments* may be accredited the turbulent inlet condition, such as the doubling of deposition in the trachea (seg. 1).

Several other numerical studies of micron particles depositing in the oral cavity are described in the literature. Despite variations in boundary conditions and geometrical model, they still provide a foundation for comparison. *Ma et al.* simulated particles inhaled at the flow rates 15, 30 and 60 l/min in a model extending to the 10th generation bronchi, with turbulent inflow conditions of varying intensity. [39]. The particles had a density of $1000\frac{kg}{m^3}$ and the geometry also included a small portion of the nasopharynx which connects the nasal passage with the respiratory system. Some increase in overall deposition efficiency appears to be due to the inclusion of this anatomical feature. The study reported an deposition efficiency of 12% for 3.0 μm particles inhaled at $Q = 30\ l/min$. Based on a visual inspec-

tion, it appears that the model used by [39] was somewhat less smooth, which may partly explain the increased deposition efficiency, besides the slightly heavier particles.

P.G Koullapis et al. carried out deposition simulations of particles with a density of 1200 μm and the flow rates 15.2, 30 and 60 l/min. [50]. Their study also included a realistic, although not turbulent, inlet profile based on experiment measurements, which they found led to an significant increase of particle deposition compared to a constant inlet profile. The results were in overall good agreement with the ones obtained in this thesis.

As mentioned in the previous section, the deposition efficiencies of the small particles are so limited that a sound statistical selection was not provided (e.g., in some segments only ≈ 10 particles deposited). Even though no uncertainty margin has been derived, it is likely that the number of released particles should have been tenfolded in order to significantly improve the statistical precision. However, as the particle tracking framework accounted for up to 50 % of the computational time during peak (time step 5000), a tenfolding of the number of particles released was not achievable with the resources available for this project.

Between $d_p = 4\ \mu m$ and $d_p = 10\ \mu m$ the deposition efficiency is increased almost by a factor 10. Thus the details in the transition from particles *penetrating* to *depositing* could, unfortunately, not be addressed.

In Chapter 6 it was shown that despite the model being meshed with 23.3 million cells, the flow was still largely underresolved in space, and to some degree also time. Moderate differences in the mean velocity profiles between the 23.3M and 40.7M mesh was also observed. As the mesh was not further refined, it was not possible to conclude that the 40.7M mesh would have provided a converged solution, and the turbulence statistics also suggested otherwise (ref. Table 6.6). Furthermore, it is not possible to conclude to which degree the particle deposition was affected by the flow being somewhat underresolved. Since results from *Brno Lung* has not yet been published, it has not been possible to compare with the results obtained by the other research groups. Given more available time and resources, particle tracking should have been performed on all meshes, which would have given qualitative information on the sensitivity of the particle deposition to the mesh resolution.

In addition, as DNS simulations are still out of practical reach, turbulence models that account for the lack of dissipation in the smallest turbulence scales, may have provided flow fields closer to the "reality". Different turbulence models such as the k-ω [68] and the simpler large eddy simulation (LES) have been employed in literature [50, 18]. A LES extension containing several models is implemented in Oasis and have been reported to perform well under testing [5]. Based on the assessment results in Joachim Bø's Master's thesis, two of the LES extensions were tested in this thesis. The *dynamic Smagorinsky* model [19], where the artificial dissipation term is adjusted every time step, yielded an increase of computational time of factor 3 and thus deemed too impractical. The simpler, standard *Smagorinsky* [59]

model did not cause a noticeable increase in computational time and was further applied during this project. However, as an error was detected in this model few weeks prior to the submission date, the simulations had to be discarded.

As briefly mentioned in Section 1.1, it is a general agreement in the scientific community that simulations of higher resolution and accuracy are necessary before CFD can provide a more detailed prediction of the deposition pattern of particles inhaled in the human respiratory system. Based on the somewhat dispersed results in the 90° bend benchmark described in Section 5.3, it also appears that more care should be taken in the validating particle tracking models. In this thesis a particle tracking algorithm with second order precision was employed, but higher order methods has been implemented in other software, such as the 6 step Runge-Kutta method in *ANSYS Fluent* [17]. However, as the flow fields simulated in this thesis was not fully resolved, it is not given that a higher order integration of the equation of particle motion would have provided a more precise deposition pattern. Hence, by also considering the aspect of time spent testing and development, the simpler, second order method was considered appropriate.

Finally, when performing any type of simulation of a physical processes occurring in the nature, it is important to remember that the result are only a model of the actual process. In the setting of computing the flow field in the human respiratory system, even though it may be possible to produce a fully converged flow field, the results are always confined by the limitation of the geometrical model. The geometry used for the simulations in this thesis is obviously not a complete model of the human respiratory system. Furthermore, the boundaries were modeled as completely rigid, which is partly justified by that the trachea and main bronchi are supported by cartilage and do not move significantly during respiration [34]. However, if extending the models to include deeper generations of the bronchi, or even the alveoli region, interaction between the air and tissue may be of high significance.

Due to the complexity of the problem studied, a discussion regarding the validity of the obtained results could be continued for many pages. The limitations of this work considered the most central can be summarized as:

- The results are confined by the limitations of the model which do not represent the full human respiratory system.
- High uncertainties in the deposition pattern in the bronchi for small particles ($d_p \leq 4.0\mu m$) due to very low deposition efficiency.
- The smallest particles ($d_p = 1.0\ \mu m$) were outside the numerical stability criterion (cf., Section 4.2.2).
- A better resolved flow field may have provided more precise results.
- The effects of different flow rates and particle densities were not considered.

7.6 Conclusion: Medical Applications

The discussion of which types of drugs are suitable for pulmonary delivery (medicine inhalation) is left to the medical professionals. However, through numerical simulations like the one performed in the thesis, it may be possible to create a map showing the likelihood of a particle of a certain property to deposit in a confined region in the human respiratory system for a given mode of respiration. Such a map may be very useful for the medical industry in determining the best action for the delivery of a given drug.

The condition perhaps most commonly associated with inhalation medicine is asthma, but an array of other deceases such as lung infection, diabetes and cystic fibrosis can be treated or relieved by inhaling medicine [49]. Furthermore, particular conditions are most effectively treated through deposition in different parts of the respiratory system. Some remedies are only effective if reaching all the way to the alveoli where gas exchange is taking place, while other needs to settle in the main bronchi.

Given particles with a density of $914 kg/m^3$ and a moderate inhalation flow rate $30\ l/s$, the following can be concluded with regards to medical applications:

- Particles larger than $10.0\ \mu m$ will mainly deposit in the oral cavity and are thus not suitable for pulmonary drug delivery.
- Particles smaller than $4.0\ \mu m$ will penetrate deep into the lung and may thus be effective for the delivery of medicine for absorption in the alveoli.
- Particles with a diameter in the range $4.0 - 10.0\ \mu m$ largely deposit it the bronchi, with smaller particles penetrating deeper.

Chapter 8

Main Findings and Future Work

8.1 Main Findings

Through carefully verifying and validating the various steps taken in this thesis, the following can be concluded:

- The open source Navier-Stokes solver Oasis is definitively suitable for computing the challenging flow conditions in the human respiratory system.
- Verification and validation is an indispensable part of any CFD experiment.
- The flow in the human respiratory system features turbulent-like characteristics even at moderate inhalation rates.
- The deposition pattern of inhaled particles of different diameters has been analyzed and we find that: Small particles ($d_p \leq 4.0\ \mu m$) penetrates deep into the lung, medium sized particles ($4.0\ \mu m < d_p \leq 10.0\ \mu m$) largely deposit in the bronchi, whereas large particles ($d_p > 10.0\ \mu m$) mostly deposit in the oral cavity.
- Small particles ($d_p \leq 4.0\ \mu m$) are more influenced by turbulent-like flow structures than the larger ones, for which the deposition pattern is mostly influenced by inertia.

8.2 Future Work

CFD simulations has proven itself as a valuable tool in describing the deposition pattern of particle inhaled in the human respiratory system. However, the field is still in development and further research coordinated between the CFD- and med-

ical community is necessary before a sufficiently precise map of particle deposition in the human respiratory system can be made.

Based on the results obtain in this thesis and a review of selected literature on the subject, it is recommended that future research focus on the following:

- Validation of CFD simulations. Computational results without thoroughly validated methods may easily be misleading.
- Development of more realistic models (mesh) that includes finer anatomical features.
- Particles with diameters between 4.0 μm and 10.0 μm where a significant change in deposition efficiency is observed. Consequently, further investigations into the deposition mechanisms should be carried out.
- Investigation of the impact of rigid versus compliant walls in order to reveal the possible importance of fluid structure interaction in the human respiratory system.
- The potential of guided drug delivery such as through magnetic drug targeting, for a potentially enhanced treatment efficiency.

Bibliography

[1] AAAAI. Asthma statistics. http://www.aaaai.org/about-aaaai/newsroom/asthma-statistics, 2016.

[2] Luca Antiga, Marina Piccinelli, Lorenzo Botti, Bogdan Ene-Iordache, Andrea Remuzzi, and David A Steinman. An image-based modeling framework for patient-specific computational hemodynamics. *Medical & biological engineering & computing*, 46(11):1097, 2008.

[3] Philipp Berg, Christoph Roloff, Oliver Beuing, Samuel Voss, Shin-Ichiro Sugiyama, Nicolas Aristokleous, Andreas S Anayiotos, Neil Ashton, Alistair Revell, Neil W Bressloff, et al. The computational fluid dynamics rupture challenge 2013—phase ii: variability of hemodynamic simulations in two intracranial aneurysms. *Journal of biomechanical engineering*, 137(12):121008, 2015.

[4] Aslak Wigdahl Bergersen. Investigating the link between patient-specific morphology and hemodynamics: Implications for aneurism initiation? Master's thesis, 2016.

[5] Joakim Bø. Implementation and assessment of subgrid-scale models for large eddy simulations of incompressible turbulent flows. Master's thesis, 2015.

[6] ME Brachet. Direct simulation of three-dimensional turbulence in the taylor—green vortex. *Fluid dynamics research*, 8(1-4):1–8, 1991.

[7] M Breuer, HT Baytekin, and EA Matida. Prediction of aerosol deposition in 90 bends using les and an efficient lagrangian tracking method. *Journal of Aerosol Science*, 37(11):1407–1428, 2006.

[8] Jonathan R Bull and Antony Jameson. Simulation of the compressible taylor green vortex using high-order flux reconstruction schemes. In *7th AIAA Theoretical Fluid Mechanics Conference*, page 3210, 2014.

[9] Alexandre Joel Chorin. Numerical solution of the navier-stokes equations. *Mathematics of computation*, 22(104):745–762, 1968.

[10] Clayton T Crowe, John D Schwarzkopf, Martin Sommerfeld, and Yutaka Tsuji. *Multiphase flows with droplets and particles*. CRC press, 2011.

[11] Lisandro Dalcín, Rodrigo Paz, and Mario Storti. Mpi for python. *Journal of Parallel and Distributed Computing*, 65(9):1108–1115, 2005.

[12] James DeBonis. Solutions of the taylor-green vortex problem using high-resolution explicit finite difference methods. *51st AIAA Aerospace Sciences Meeting including the New Horizons Forum and Aerospace Exposition*, 2013.

[13] Jakub Elcner, Frantisek Lizal, Jan Jedelsky, Miroslav Jicha, and Michaela Chovancova. Numerical investigation of inspiratory airflow in a realistic model of the human tracheobronchial airways and a comparison with experimental results. *Biomechanics and modeling in mechanobiology*, 15(2):447–469, 2016.

[14] S Elghobashi. On predicting particle-laden turbulent flows. *Applied scientific research*, 52(4):309–329, 1994.

[15] Charles L Fefferman. Existence and smoothness of the navier-stokes equation. *The millennium prize problems*, pages 57–67, 2006.

[16] WH Finlay, KW Stapleton, and J Yokota. On the use of computational fluid dynamics for simulating flow and particle deposition in the human respiratory tract. *Journal of Aerosol Medicine*, 9(3):329–341, 1996.

[17] ANSYS Fluent. 15.0 user's manual, ansys documentation n fluent n user's guide & theory guide—release 15.0. *ANSYS Inc., ANSYS Inc.*

[18] T Gemci, Valery Ponyavin, Y Chen, H Chen, and R Collins. Computational model of airflow in upper 17 generations of human respiratory tract. *Journal of Biomechanics*, 41(9):2047–2054, 2008.

[19] Massimo Germano, Ugo Piomelli, Parviz Moin, and William H Cabot. A dynamic subgrid-scale eddy viscosity model. *Physics of Fluids A: Fluid Dynamics*, 3(7):1760–1765, 1991.

[20] Christophe Geuzaine and Jean-François Remacle. Gmsh: A 3-d finite element mesh generator with built-in pre-and post-processing facilities. *International Journal for Numerical Methods in Engineering*, 79(11):1309–1331, 2009.

[21] Jean-Luc Guermond, Peter Minev, and Jie Shen. An overview of projection methods for incompressible flows. *Computer methods in applied mechanics and engineering*, 195(44):6011–6045, 2006.

[22] Ragnar Winther Hans Petter Langtangen, Kent Andre Mardal. Solving nonlinear ode and pde problems. 2016.

[23] Isles K. D. Johnston, J. R. and D. C. F Muir. *Inhaled Particles*, 4:61–72, 1977.

[24] George Karniadakis and Spencer Sherwin. *Spectral/hp element methods for computational fluid dynamics*. Oxford University Press, 2013.

[25] MO Khan, DA Steinman, and K Valen-Sendstad. Non-newtonian versus numerical rheology: Practical impact of shear-thinning on the prediction of sta-

ble and unstable flows in intracranial aneurysms. *International Journal for Numerical Methods in Biomedical Engineering*, 2016.

[26] MO Khan, K Valen-Sendstad, and DA Steinman. Narrowing the expertise gap for predicting intracranial aneurysm hemodynamics: impact of solver numerics versus mesh and time-step resolution. *American Journal of Neuroradiology*, 36(7):1310–1316, 2015.

[27] Muhammad Owais Khan, Christophe Chnafa, Diego Gallo, Filippo Molinari, Umberto Morbiducci, David A Steinman, and Kristian Valen-Sendstad. On the quantification and visualization of transient periodic instabilities in pulsatile flows. *Journal of biomechanics*, 52:179–182, 2017.

[28] Robert M. Kirby and George Em Karniadakis. *Under-resolution and Diagnostics in Spectral Simulations of Complex-Geometry Flows*, pages 1–42. Springer Netherlands, Dordrecht, 2002.

[29] Václav Kolář. Vortex identification: New requirements and limitations. *International journal of heat and fluid flow*, 28(4):638–652, 2007.

[30] P.K. Kundu and I.M. Cohen. *Fluid Mechanics*. Elsevier Science, 2010.

[31] Hans Petter Langtangen. Truncation error analysis. http://hplgit.github.io/num-methods-for-PDEs/doc/pub/trunc/pdf/trunc-4print.pdf, 2015.

[32] Wing-Hin Lee, Ching-Yee Loo, Daniela Traini, and Paul M Young. Inhalation of nanoparticle-based drug for lung cancer treatment: Advantages and challenges. *asian journal of pharmaceutical sciences*, 10(6):481–489, 2015.

[33] Ching-Long Lin, Merryn H Tawhai, Geoffrey McLennan, and Eric A Hoffman. Characteristics of the turbulent laryngeal jet and its effect on airflow in the human intra-thoracic airways. *Respiratory physiology & neurobiology*, 157(2):295–309, 2007.

[34] Frantisek Lizal, Miloslav Belka, Jan Adam, Jan Jedelsky, and Miroslav Jicha. A method for in vitro regional aerosol deposition measurement in a model of the human tracheobronchial tree by the positron emission tomography. *Proceedings of the Institution of Mechanical Engineers, Part H: Journal of Engineering in Medicine*, 229(10):750–757, 2015.

[35] Frantisek Lizal, Jakub Elcner, Philip K Hopke, Jan Jedelsky, and Miroslav Jicha. Development of a realistic human airway model. *Proceedings of the Institution of Mechanical Engineers, Part H: Journal of Engineering in Medicine*, 226(3):197–207, 2012.

[36] Anders Logg, Kent-Andre Mardal, and Garth Wells. *Automated solution of differential equations by the finite element method: The FEniCS book*, volume 84. Springer Science & Business Media, 2012.

[37] OpenCFD Ltd. Openfoam documentation. http://www.openfoam.com/documentation/, 2017.

[38] John L. Lumley and Akiva M. Yaglom. A century of turbulence. *Flow, Turbulence and Combustion*, 66(3):241–286, 2001.

[39] Baoshun Ma and Kenneth R. Lutchen. Cfd simulation of aerosol deposition in an anatomically based human large–medium airway model. *Annals of Biomedical Engineering*, 37(2):271, 2008.

[40] Matthew Masoli, Denise Fabian, Shaun Holt, and Richard Beasley. The global burden of asthma: executive summary of the gina dissemination committee report. *Allergy*, 59(5):469–478, 2004.

[41] J.J. Monaghan and J.B. Kajtar. Leonardo da vinci's turbulent tank in two dimensions. *European Journal of Mechanics - B/Fluids*, 44:1 – 9, 2014.

[42] SAj Morsi and AJ Alexander. An investigation of particle trajectories in two-phase flow systems. *Journal of Fluid mechanics*, 55(02):193–208, 1972.

[43] Mikael Mortensen. Fenicstools, 2017. https://github.com/mikaem/fenicstools.

[44] Mikael Mortensen and Kristian Valen-Sendstad. Oasis: A high-level/high-performance open source navier-stokes solver. *Computer physics communications*, 188:177–188, 2015.

[45] Cecil D Murray. The physiological principle of minimum work ii. oxygen exchange in capillaries. *Proceedings of the National Academy of Sciences*, 12(5):299–304, 1926.

[46] Jonathan P Mynard and Kristian Valen-Sendstad. A unified method for estimating pressure losses at vascular junctions. *International journal for numerical methods in biomedical engineering*, 31(7), 2015.

[47] NASA. 3rd international workshop on higher-order cfd methods. https://www.grc.nasa.gov/hiocfd/, 2015.

[48] World Health Organization. World health statistics 2008, 2008. http://www.who.int/whosis/whostat/2008/en/.

[49] John S Patton and Peter R Byron. Inhaling medicines: delivering drugs to the body through the lungs. *Nature Reviews Drug Discovery*, 6(1):67–74, 2007.

[50] M.P. Bivolarova A.K. Melikov P.G. Koullapis, S.C. Kassinos. Particle deposition in a realistic geometry of the human conducting airways: Effects of inlet velocity profile, inhalation flowrate and electrostatic charge. *Journal of Biomechanics*, 29(11):2201–2212, 20152.

[51] S.B. Pope. *Turbulent Flows*. Cambridge University Press, 2000.

[52] Arthur W. Proetz. Xli air currents in the upper respiratory tract and their clinical importance. *Annals of Otology, Rhinology & Laryngology*, 60(2):439–467, 1951. PMID: 14857634.

[53] David Y. H. Pui, Francisco Romay-Novas, and Benjamin Y. H. Liu. Experimental study of particle deposition in bends of circular cross section. *Aerosol Science and Technology*, 7(3):301–315, 1987.

[54] P.J. Roache. *Verification and Validation in Computational Science and Engineering*. Hermosa, 1998.

[55] White FM Roache PJ, Ghia KN. Editorial policy statement on the control of numerical accuracy. *Journal of Fluids Engineering*, 108(3):2–3, 1986.

[56] M. Schäfer, S. Turek, F. Durst, E. Krause, and R. Rannacher. *Benchmark Computations of Laminar Flow Around a Cylinder*, pages 547–566. Vieweg+Teubner Verlag, Wiesbaden, 1996.

[57] Richard B Schlesinger, Daryl E Bohning, Tai L Chan, and Morton Lippmann. Particle deposition in a hollow cast of the human tracheobronchial tree. *Journal of Aerosol Science*, 8(6):429–445, 1977.

[58] W Schroeder, K Martin, and B Lorensen. Vtk textbook 4th edition. kitware, 2006.

[59] Joseph Smagorinsky. General circulation experiments with the primitive equations: I. the basic experiment. *Monthly weather review*, 91(3):99–164, 1963.

[60] David A Steinman, Yiemeng Hoi, Paul Fahy, Liam Morris, Michael T Walsh, Nicolas Aristokleous, Andreas S Anayiotos, Yannis Papaharilaou, Amirhossein Arzani, Shawn C Shadden, et al. Variability of computational fluid dynamics solutions for pressure and flow in a giant aneurysm: the asme 2012 summer bioengineering conference cfd challenge. *Journal of biomechanical engineering*, 135(2):021016, 2013.

[61] GI Taylor and AE Green. Mechanism of the production of small eddies from large ones. *Proceedings of the Royal Society of London. Series A, Mathematical and Physical Sciences*, 158(895):499–521, 1937.

[62] Chuen-Jinn Tsai and David YH Pui. Numerical study of particle deposition in bends of a circular cross-section-laminar flow regime. *Aerosol Science and Technology*, 12(4):813–831, 1990.

[63] Kristian Valen-Sendstad, Kent-André Mardal, and David A Steinman. High-resolution cfd detects high-frequency velocity fluctuations in bifurcation, but not sidewall, aneurysms. *Journal of biomechanics*, 46(2):402–407, 2013.

[64] Kristian Valen-Sendstad, Marina Piccinelli, and David A Steinman. High-resolution computational fluid dynamics detects flow instabilities in the carotid siphon: Implications for aneurysm initiation and rupture? *Journal of biomechanics*, 47(12):3210–3216, 2014.

[65] Kristian Valen-Sendstad and DA Steinman. Mind the gap: impact of computational fluid dynamics solution strategy on prediction of intracranial

aneurysm hemodynamics and rupture status indicators. *American Journal of Neuroradiology*, 35(3):536–543, 2014.

[66] Ewald R. Weibel. *Geometric and Dimensional Airway Models of Conductive, Transitory and Respiratory Zones of the Human Lung*, pages 136–142. Springer Berlin Heidelberg, Berlin, Heidelberg, 1963.

[67] F.M. White. *Viscous Fluid Flow*. McGraw-Hill series in mechanical engineering. McGraw-Hill, 2006.

[68] David C Wilcox et al. *Turbulence modeling for CFD*, volume 2. DCW industries La Canada, CA, 1998.

[69] Yue Zhou and Yung-Sung Cheng. Particle deposition in a cast of human tracheobronchial airways. *Aerosol Science and Technology*, 39(6):492–500, 2005.